Study and optimization of 2D matrix arrays for 3D ultrasound imaging

Bakary Diarra

Université Claude Bernard Lyon 1 — Università degli Studi di Firenze — Université de Lyon

N° d'ordre : 165 - 2013 Année 2013

THESE DE L'UNIVERSITE DE LYON

délivrée par

L'UNIVERSITE CLAUDE BERNARD LYON 1

et préparée en cotutelle avec

L'UNIVERSITÀ DEGLI STUDI DI FIRENZE

ECOLE DOCTORALE : MÉCANIQUE, ÉNERGÉTIQUE, GÉNIE CIVIL, ACOUSTIQUE

DOTTORATO DI RICERCA : TECNOLOGIE ELETTRONICHE PER L'INGEGNERIA DELL'INFORMAZIONE

DIPLOME DE DOCTORAT
(arrêté du 7 août 2006 / arrêté du 6 janvier 2005)

soutenue publiquement le 11 octobre 2013

par

Bakary DIARRA
Ingénieur INSA Lyon 2010

Study and optimization of 2D matrix arrays for 3D ultrasound imaging

Jury

Christian CACHARD	Professeur des Universités, Lyon 1	Co-directeur de thèse
Hervé LIEBGOTT	Maitre de Conférences, Lyon 1	Co-directeur de thèse
Jérôme MARS	Professeur des Universités, Grenoble	Rapporteur
Nicolò Attilio SPECIALE	Ricercatore Confermato, Bologna	Examinateur
Jean Philippe THIRAN	Professeur Associé, Lausanne	Examinateur
Piero TORTOLI	Professore Ordinario, Firenze	Co-directeur de thèse
Andrea TRUCCO	Professore Associato, Genova	Rapporteur
Marc ROBINI	Maitre de Conférences, INSA Lyon	Invité

Abstract

3D Ultrasound imaging is a fast-growing medical imaging modality. In addition to its numerous advantages (low cost, non-ionizing beam, portability) it allows to represent the anatomical structures in their natural form that is always three-dimensional. The relatively slow mechanical scanning probes tend to be replaced by two-dimensional matrix arrays that are an extension in both lateral and elevation directions of the conventional 1D probe. This 2D positioning of the elements allows the ultrasonic beam steering in the whole space. Usually, the piezoelectric elements of a 2D array probe are aligned on a regular grid and spaced out of a distance (the pitch) subject to the space sampling law (inter-element distance must be shorter than a mid-wavelength) to limit the impact of grating lobes. This physical constraint leads to a multitude of small elements. The equivalent in 2D of a 1D probe of 128 elements contains 128x128 = 16,384 elements. Connecting such a high number of elements is a real technical challenge as the number of channels in current ultrasound scanners rarely exceeds 256. The proposed solutions to control this type of probe implement multiplexing or elements number reduction techniques, generally using random selection approaches (« sparse array »). These methods suffer from low signal to noise ratio due to the energy loss linked to the small number of active elements. In order to limit the loss of performance, optimization remains the best solution.

The first contribution of this thesis is an extension of the « sparse array » technique combined with an optimization method based on the simulated annealing algorithm. The proposed optimization reduces the required active element number according to the expected characteristics of the ultrasound beam and permits limiting the energy loss compared to the initial dense array probe.

The second contribution is a completely new approach adopting a non-grid positioning of the elements to remove the grating lobes and to overstep the spatial sampling constraint. This new strategy allows the use of larger elements leading to a small number of necessary elements for the same probe surface. The active surface of the array is maximized, which results in a greater output energy and thus a higher sensitivity. It also allows a greater scan sector as the grating lobes are very small relative to the main lobe. The random choice of the position of the elements and their apodization (or weighting coefficient) is optimized by the simulated annealing.

The proposed methods are systematically compared to the dense array by performing simulations under realistic conditions. These simulations show a real potential of the developed techniques for 3D imaging.

A 2D probe of 8x24 = 192 elements was manufactured by Vermon (Vermon SA, Tours, France) to test the proposed methods in an experimental setting. The comparison between simulation and experimental results validate the proposed methods and prove their feasibility.

Résumé

L'imagerie échographique en trois dimensions (3D) est une modalité d'imagerie médicale en plein développement. En plus de ses nombreux avantages (faible cout, absence de rayonnement ionisant, portabilité) elle permet de représenter les structures anatomiques dans leur forme réelle qui est toujours 3D. Les sondes à balayage mécaniques, relativement lentes, tendent à être remplacées par des sondes bidimensionnelles ou matricielles qui sont un prolongement dans les deux directions, latérale et azimutale, de la sonde classique 1D. Cet agencement 2D permet un dépointage du faisceau ultrasonore et donc un balayage 3D de l'espace. Habituellement, les éléments piézoélectriques d'une sonde 2D sont alignés sur une grille et régulièrement espacés d'une distance (en anglais le « pitch ») soumise à la loi de l'échantillonnage spatial (distance inter-élément inférieure à la demi-longueur d'onde) pour limiter l'impact des lobes de réseau. Cette contrainte physique conduit à une multitude d'éléments de petite taille. L'équivalent en 2D d'une sonde 1D de 128 éléments contient 128x128=16 384 éléments. La connexion d'un nombre d'éléments aussi élevé constitue un véritable défi technique puisque le nombre de canaux dans un échographe actuel n'excède que rarement les 256. Les solutions proposées pour contrôler ce type de sonde mettent en œuvre du multiplexage ou des techniques de réduction du nombre d'éléments, généralement basées sur une sélection aléatoire de ces éléments (« sparse array »). Ces méthodes souffrent du faible rapport signal à bruit du à la perte d'énergie qui leur est inhérente. Pour limiter ces pertes de performances, l'optimisation reste la solution la plus adaptée.

La première contribution de cette thèse est une extension du « sparse array » combinée avec une méthode d'optimisation basée sur l'algorithme de recuit simulé. Cette optimisation permet de réduire le nombre nécessaire d'éléments à connecter en fonction des caractéristiques attendues du faisceau ultrasonore et de limiter la perte d'énergie comparée à la sonde complète de base.

La deuxième contribution est une approche complètement nouvelle consistant à adopter un positionnement hors grille des éléments de la sonde matricielle permettant de supprimer les lobes de réseau et de s'affranchir de la condition d'échantillonnage spatial. Cette nouvelle stratégie permet d'utiliser des éléments de taille plus grande conduisant ainsi à un nombre d'éléments nécessaires beaucoup plus faible pour une même surface de sonde. La surface active de la sonde est maximisée, ce qui se traduit par une énergie plus importante et donc une meilleure sensibilité. Elle permet également de balayer un angle de vue plus important, les lobes de réseau étant très faibles par rapport au lobe principal. Le choix aléatoire de la position des éléments et de leur apodization (ou pondération) reste optimisé par le recuit simulé.

Les méthodes proposées sont systématiquement comparées avec la sonde complète dans le cadre de simulations numériques dans des conditions réalistes. Ces simulations démontrent un réel potentiel pour l'imagerie 3D des techniques développées.

Une sonde 2D de 8x24=192 éléments a été construite par Vermon (Vermon SA, Tours France) pour tester les méthodes de sélection des éléments développées dans un cadre expérimental. La comparaison entre les simulations et les résultats expérimentaux permettent de valider les méthodes proposées et de prouver leur faisabilité.

Sommario

L'ecografia 3D è una modalità di imaging medicale in rapida crescita. Oltre ai vantaggi in termini di prezzo basso, fascio non ionizzante, portabilità, essa permette di rappresentare le strutture anatomiche nella loro forma naturale, che è sempre tridimensionale. Le sonde a scansione meccanica, relativamente lente, tendono ad essere sostituite da quelle bidimensionali che sono una estensione in entrambe le direzioni laterale ed azimutale della sonda convenzionale 1D. Questo posizionamento 2D degli elementi permette l'orientamento del fascio ultrasonico in tutto lo spazio. Solitamente, gli elementi piezoelettrici di una sonda matriciale 2D sono allineati su una griglia regolare e separati da una distanza (detta “pitch”) sottoposta alla legge del campionamento spaziale (la distanza inter-elemento deve essere meno della metà della lunghezza d'onda) per limitare l'impatto dei lobi di rete. Questo vincolo fisico porta ad una moltitudine di piccoli elementi. L'equivalente di una sonda 1D di 128 elementi contiene 128x128 = 16.384 elementi in 2D. Il collegamento di un così grande numero di elementi è una vera sfida tecnica, considerando che il numero di canali negli ecografi attuali supera raramente 256. Le soluzioni proposte per controllare questo tipo di sonda implementano le tecniche di multiplazione o la riduzione del numero di elementi, utilizzando un metodo di selezione casuale (« sparse array »). Questi metodi soffrono di un basso rapporto segnale-rumore dovuto alla perdita di energia. Per limitare la perdita di prestazioni, l’ottimizzazione rimane la soluzione migliore.

Il primo contributo di questa tesi è un’estensione del metodo dello « sparse array » combinato con un metodo di ottimizzazione basato sull'algoritmo del simulated annealing. Questa ottimizzazione riduce il numero degli elementi attivi richiesto secondo le caratteristiche attese del fascio di ultrasuoni e permette di limitare la perdita di energia.

Il secondo contributo è un approccio completamente nuovo, che propone di adottare un posizionamento fuori-griglia degli elementi per rimuovere i lobi secondari e per scavalcare il vincolo del campionamento spaziale. Questa nuova strategia permette l'uso di elementi più grandi, riducendo così il numero di elementi necessari per la stessa superficie della sonda. La superficie attiva della sonda è massimizzata, questo si traduce in una maggiore energia e quindi una maggiore sensibilità. Questo permette inoltre la scansione di un più grande settore, in quanto i lobi secondari sono molto piccoli rispetto al lobo principale. La scelta casuale della posizione degli elementi e la loro apodizzazione viene ottimizzata dal simulated annealing. I metodi proposti sono stati sistematicamente confrontati con la sonda completa eseguendo simulazioni in condizioni realistiche. Le simulazioni mostrano un reale potenziale delle tecniche sviluppate per l'imaging 3D.

Una sonda 2D di 8x24 = 192 elementi è stata fabbricata da Vermon (Vermon SA, Tours France) per testare i metodi proposti in un ambiente sperimentale. Il confronto tra le simulazioni e i risultati sperimentali ha permesso di convalidare i metodi proposti e dimostrare la loro fattibilità.

List of symbols

Generalities on ultrasound imaging

λ	Wavelength (m)
ρ	Density (kg/m^3)
τ	Pressure transmission coefficient
τ_n	Time delay of nth element
ω	Pulsation frequency (rad/s)
c	Sound speed or velocity (m/s^2)
f	Central frequency of the probe (MHz)
k	Wave number (m^{-1})
R	Energy (power) reflection coefficient
r	Pressure reflection coefficient
T	Energy (power) transmission coefficient
Z	Acoustical impedance (MRay or kg/s^2/m^2)

From 1D to 2D arrays

Theoretical expression

δ	Dirac function
θ	Angle in lateral direction
φ	Angle in elevation direction
τ_{ij}	Time delay of the element (i, j)
D	Dimension (1D, 2D, 3D)
d	Inter-element distance (m)
w	Piezoelectric element size (m)
L	Array dimensions (width and height)
Hs	Transfer function of the 2D array (frequency domain)
h	Transfer function of the 2D array (time domain)
s	Piezoelectric element surface (m^2)
P	Pressure function
M	number of element in lateral direction
N	number of element in elevation direction

w_{ij} Apodization of the element (i, j)

Simulated annealing

Γ Markov chain

γ Weighting coefficient matrix (between 0 and 1 after normalization)

Λ Optimization space

μ Strength of sparsity in the cost function

η Temporary weighting coefficient during optimization

σ_A Indexes of active elements

τ Temperature decrease coefficient

A Active element number in the sparse array

f Cost function

$\mathcal{M}$ Total number of elements MxN

$\mathcal{N}$ Total number of iterations

p Pressure function

P_M Maximum value of the pressure

p_s Authorized sidelobes level

q Probability

SA Simulated annealing

T Temperature function

U Space excluding the main lobe area

$4{:}\,1$ Rectangular array (64x16)

Contents

Introduction

The ultrasound imaging plays an important role today in the domain of medical diagnosis and therapy domains. Real-time volumetric imaging is an interesting and attractive ultrasound imaging technique as it provides more realistic representations of the tissues. Such imaging is useful for real time interventional tools tracking and visualization, for moving organs imaging like the heart and permits to image deep organs in the human body. Several advances have been made in this domain [Light et al. (1997), Yen and Smith (2002)] but many obstacles are to be overcome among which the connection difficulty and the energy loss caused by the reduction methods. Indeed, these arrays ideally contain several thousand of elements whereas the number of channels in recent scanners exceeds seldom 256.

This thesis focuses on the research of solutions to make 2D arrays usable routinely. Making that possible means finding realistic tradeoffs between the active elements number and the probe energy. Strategies combining optimization algorithms and innovative elements positioning are needed. The element number reduction keeping a good beam pattern compared to the full array is not easy as element number and energy are linked. The solutions proposed may considerably impact both ultrasound imaging and therapy as HIFU operations.

This thesis is divided in four chapters:

- The first chapter presents the general aspect of the ultrasound waves as well as a brief introduction to the piezoelectric property and its use in tissue imaging. The basis of the echography and its usefulness in today medicine are introduced.
- The second chapter is about the state of art in the domain of the 2D arrays imaging. The chapter begins with a presentation of the ultrasound arrays evolution from the classical 1D array to the full 2D array. The mathematical background of the 2D arrays, the element number reduction (corner element suppression, sparse array techniques) and the optimization algorithm (the simulated annealing), the progresses and the challenges in this domain are mentioned. The beam profile of the dense array and the sparse array techniques are compared to evaluate their advantages and drawbacks.
- In the third chapter, we present our contributions in terms of optimization and element positioning strategies. The methods proposed are the non-grid (sparse) array, the variable size non-grid array and an improved version of the simulated annealing algorithm. Each technique proposed is compared to its corresponding dense arrays for validation. The comparison criteria are the active element number, the beam energy (sensitivity), the spatial resolution and the grating lobes level. A simulation of the PSF is presented in each case in different scanning angle to appreciate the imaging capability of each method.
- The fourth chapter is dedicated to the experimental validation of the proposed optimization technique. The first part of the measurement was conducted using a small 8x8 array in the MSDLab, in the University of Florence. The second part of the measurements was performed in CREATIS using a new prototype array of 24x16=192 elements developed according to the simulations realized throughout this study. As our ultrasound open research platform (Ula-OP [Tortoli et al. (2009), Boni et al. (2012)]) has only 64 channels, the validation is made on 8x8 sub-arrays to provide realistic comparison between dense and sparse arrays. The

measurements concern only the standard sparse arrays as any prototype based on the non-grid array is available yet.

This thesis ends with the conclusion and the perspectives about the future developments of the methods proposed.

Chapter 1

Generalities on ultrasound imaging

This chapter explains the main principles of ultrasound and its application to medical imaging. A brief presentation of the piezoelectric effects, the origin of the ultrasound and its use in echography are explained. Finally, some simulation tools and the current ultrasound imaging limitations are mentioned.

1.1. Introduction

Imaging is indispensable in modern medical practice because it represents the eye of the physician both in diagnosis and therapies. For example, ultrasound becomes more and more used in surgical tools tracking and follow-up during biopsy and also in minimally invasive surgery [Basset and Cachard (2007)].

Ultrasound imaging is one of the most widely used imaging modalities nowadays; more than a quarter of diagnosis imaging in the world are performed using ultrasound and the proportion is continuously growing. This success of ultrasound imaging comes from many factors among which its innocuousness and the cheapness of the scanners. An ultrasound scanner is mainly composed of the probe, which transmits and receives the echoes, and the control system linked to a visualization screen. The probe consists in several piezoelectric elements arranged in line (linear array), in curve (convex array) or in several rows and columns (2D matrix array). The thickness of the piezoelectric elements imposes the central frequency of the probe and their arrangement the scanning type. When the probe is excited, the piezoelectric elements vibrate (indirect piezoelectric property) and produce sound waves. These waves are used to analyze the support media. Generally a 1D array probe consists of 128 to 256 piezoelectric elements which are supplied electronically in steps of 64 (most of the time) at a time to form a firing line. The interpolation of all lines on the whole probe provides a plane image of the medium investigated. The medium physical constituents (scatterers) have a considerable impact on the resulting image, their concentration and dimensions determine the image texture. However, there are image enhancers like contrast agents that act as extrinsic scatterers injected into the medium for a temporary and locally improvement of the image quality. Ultrasound imaging has several advantages: it has a good resolution, it is non-hazardous to the patient, it is the safest imaging modality and an affordable technology compared to other imaging modalities. Its disadvantages are the difficulty of interpretation (unless highly experienced persons) and its impossibility of imaging organs containing air (like lungs) and solids (like bones).

1.2. Piezoelectricity and ultrasound

The piezoelectricity is the property of some materials to produce electrical signals when they are submitted to a mechanical force (strain), this is called the direct piezoelectric effect (Figure 1.1a). The opposite effect does exist too; it consists in transmitting a mechanical force (or pressure) when these materials are excited by an electrical signal (Figure 1.1b). This

intrinsic property to some materials comes from the dissymmetry in their internal composition. When a piezoelectric material is excited by an electrical current, its spectrum analysis presents resonance frequencies which depend on its dimensions. The materials cover all frequencies domain from low to high frequencies. The most used material in the domain of ultrasound imaging is the PZT (Lead Zirconium Titanate) because of its easiness to be cut into different shapes to create different wave modes; it can also be used for low voltages and high temperatures. New generation ultrasound transducers made of CMUTs (Capacitive Micromachined Ultrasonic Transducers)[Wygant et al. (2008)] are getting more and more investigated but their use remains in research domain for now. As the human hearing spectrum ranges approximately from 12 Hz to 20 kHz, the ultrasound spectrum which ranges from the MHz to several tens of MHz is not audible. These ultrasound waves have the property to propagate in the media in which they are produced and permit to assess some characteristics of these latter. Ultrasound has a lot of application domains among which underwater acoustics in military domains and fishing (sonars), telecommunications as filters (surface Acoustic Wave), cleaning, and medical imaging (echography) and therapy (HIFU). In medical ultrasound imaging (echography), both direct and indirect piezoelectric effects are used by the ultrasound probe in reception (Figure 1.1a) and in transmission (Figure 1.1b), respectively.

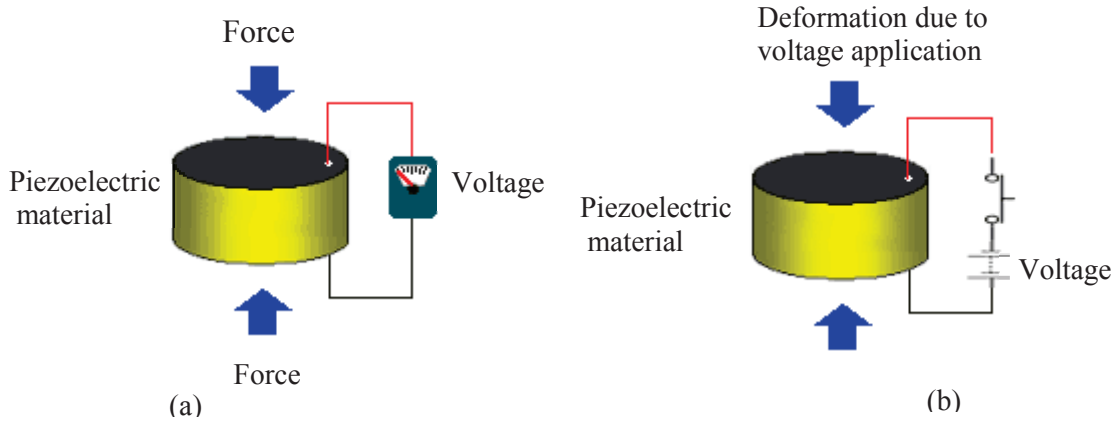

Figure 1.1: illustration of the piezoelectric effects (a) the direct effect and (b) the indirect effect. (Images from the website http://www.robotplatform.com). In ultrasound imaging the piezoelectric elements are supplied by an electrical signal (indirect effect) and the vibration generated permits to transmit the ultrasound wave. In reception the echoes sent back by the medium constitute a strain which action produces electrical signal (direct effect) transporting the information about the medium.

1.3. Echography

Echography is the use of the propagation properties of the ultrasound waves to describe media (Figure 1.2). The use of ultrasound in medicine began in the 50's and has been routinely employed since the early 70's. These techniques derived from those employed in the radar systems, submarine sonars and the non-destructive control of the materials. The advantage of ultrasound in the human body exploration, compared to the other imaging modalities (X-ray, IRM, etc…) is on one hand its non-ionizing behavior, painlessness and its easiness to implement and in the other hand the cheapness and the portability of the systems.

The main components of an ultrasound scanner are the piezoelectric elements which permit the transmission and the reception of the ultrasound waves. An ultrasound wave is characterized by its wavelength (λ) which depends on the resonance frequency (f) of the piezoelectric crystal and its propagation celerity (c)

$$\lambda = c/f. \tag{1.1}$$

The celerity value depends on the medium and in the biological media its value is assumed to be close to that of water which is about $c = 1540$ m/s. The frequency ranges from 1 MHz to 20 MHz for most of the applications. The principle of ultrasound imaging is based on the interaction with the propagation medium. When the ultrasound propagates in the medium it is reflected at different interfaces of this latter. The intensity and the reception time of the reflected waves permit to evaluate the interface "intensity" and its position in the medium.

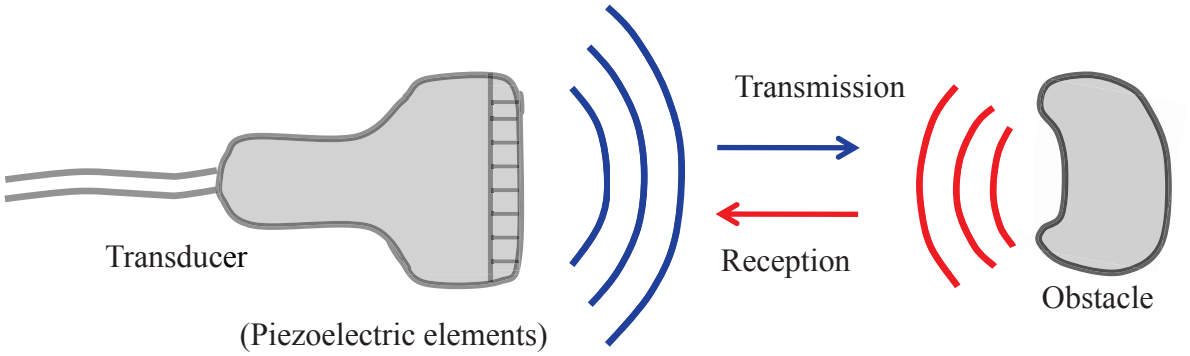

Figure 1.2 : principle of ultrasound imaging. The transmitted waves (blue) are reflected back by the obstacle (target) to the probe (red). The transmission and the echoes are regularly separated by the pulse repetition frequency to avoid stationary waves formation.

Figure 1.2 illustrates the operating mode of a 1D probe (transducer) transmitting the ultrasound and receiving the echo coming from the medium represented by the obstacle. In practice the propagation medium contains a huge number of reflectors (also known as scatterers) which size compared to the wavelength determines the type of reflection

- Specular reflection if the incident signal is reflected with the same angle in the opposite direction. This type of reflection occurs when the size of the scatterers contained in the medium is larger than the wavelength (as in large polite surfaces). It is responsible for the brightness of the interfaces (boundaries) between different parts of the medium.
- Diffuse reflection if the incident signal is reflected in all directions. This type of reflection occurs when the size of the scatterers within the medium is smaller than the wavelength as in rough surfaces. This kind of reflection is commonly known under the name of scattering in ultrasound imaging and it determines the echo texture of the medium.

A medium is characterized by its acoustical impedance Z (expressed in Rayleigh or $kg/s^2/m^2$) being the product of the celerity (c in m/s^2) of the sound and its density (ρ in kg/m^3)

$$Z = \rho c\ . \tag{1.2}$$

This parameter plays an important role in the imaging because it determines the transmission and reflection coefficients of the ultrasound wave during its propagation. Let's consider the schematic of Figure 1.3

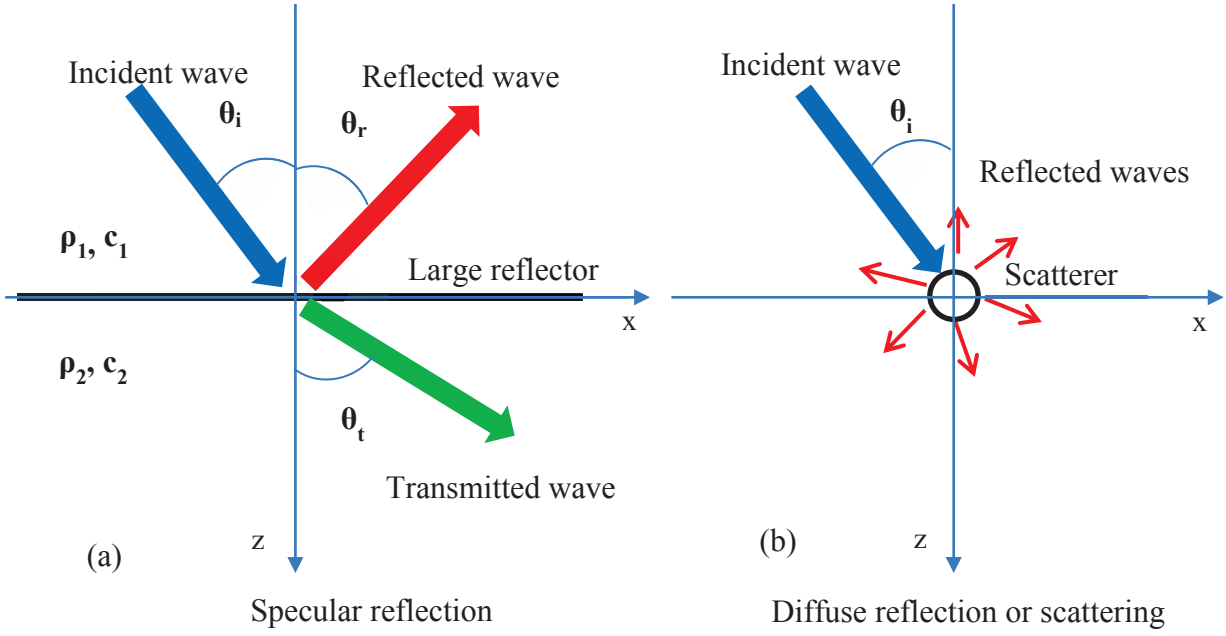

Figure 1.3 : illustration of the two types of reflection in ultrasound imaging (a) specular and (b) diffuse reflection. The specular reflection occurs when the size of the reflector encountered by the ultrasound wave is larger than the wavelength like interfaces of different media. The diffuse reflection determines the texture of the ultrasound image and originates from reflectors (scatterers) smaller than the wavelength.

Considering the specular case (Figure 1.3a), the reflection and the transmission coefficients can be mathematically established. The propagation of ultrasound (under the plane wave, homogeneous medium and 1D propagation assumptions) follows the general acoustical equation

$$\frac{\partial^2 p}{\partial z^2} - \frac{1}{c^2}\frac{\partial^2 p}{\partial t^2} = 0 \tag{1.3}$$

with p the pressure function (in Pa), c the wave celerity (m/s^2) and z the propagation direction. The solution of that equation can be expressed as

$$p(z,t) = ae^{-j(kz-\omega t)} + be^{j(kz-\omega t)} \tag{1.4}$$

where a is the amplitude of the propagating wave in z direction and b the amplitude of the returning wave (in –z direction), k is the wave vector and ω the wave pulsation, f is the frequency and λ the wavelength

$$k = \frac{\omega}{c} = \frac{2\pi}{\lambda}; \omega = \frac{2\pi}{f}. \tag{1.5}$$

In the configuration of specular reflection in Figure 1.3a, the two media have different acoustical properties ($c_1 \neq c_2$ and $\rho_1 \neq \rho_2$) and they are separated by a large reflector in the plane z=0. In the plane z<0, the pressure can be expressed as

$$p_1(z) = e^{-jk_1 z} + re^{jk_1 z} \tag{1.6}$$

where r is the reflection coefficient being the ratio between a/b from (1.4). The pressure in the plane z>0 is

$$p_2(z) = \tau e^{-jk_2 z} \tag{1.7}$$

where τ is the transmission coefficient in the $z>0$ plane . The conditions of continuity of the pressure at the interface $z=0$ give

$$p_1(z)|_{z=0} = p_2(z)|_{z=0} \Rightarrow 1 + r = \tau \tag{1.8}$$

and the continuity of the particle velocity at the interface gives

$$\frac{1}{\rho_1}\frac{\partial p_1(z)}{\partial z}\bigg|_{z=0} = \frac{1}{\rho_2}\frac{\partial p_2(z)}{\partial z}\bigg|_{z=0} \Rightarrow 1 - r = \frac{Z_1\cos(\theta_t)}{Z_2\cos(\theta_i)}\tau\,. \tag{1.9}$$

These two continuity conditions permit to determine the transmission and the reflection coefficients at the interface $z=0$

$$r = \frac{Z_2\cos(\theta_i) - Z_1\cos(\theta_t)}{Z_2\cos(\theta_i) + Z_1\cos(\theta_t)}\;;\;\; \tau = \frac{2Z_2\cos(\theta_i)}{Z_2\cos(\theta_i) + Z_1\cos(\theta_t)} \tag{1.10}$$

where Z_1 and Z_2 are the acoustical impedances of the two planes as defined in (1.2). If the incidence and the transmission angles are equal to zero, then the equation (1.10) becomes

$$r = \frac{Z_2 - Z_1}{Z_2 + Z_1};\;\; \tau = \frac{2Z_2}{Z_2 + Z_1}\,. \tag{1.11}$$

The reflection coefficient corresponding to the power is the squared value of that of the pressure in (1.10) and (1.11). In the simple case of (1.11), the reflection coefficient becomes $R = r^2$ and in transmission $T = 1 - R$

$$R = \left(\frac{Z_2 - Z_1}{Z_2 + Z_1}\right)^2\;;\;\; T = \frac{4Z_1Z_2}{(Z_2 + Z_1)^2}\,. \tag{1.12}$$

The equation (1.12) shows the importance of the acoustical properties of the different parts of a medium to be explored by ultrasound. In particular, if the difference between the impedance is too important ($Z_1 \gg Z_2$ or $Z_1 \ll Z_2$), the reflection coefficient $R \approx 1$ and $T \approx 0$, no energy is transmitted, so it's impossible to describe the second medium. This situation occurs when the transducer transmits in the air. This can be dangerous for the probe because elements can be destroyed by overheating. In the case of $Z_2 \approx Z_1$, the reflection $R \approx 0$, no energy is turned back to the transducer.

All these equations are valid in the case of a linear propagation which supposes that all the acoustical properties of the media remain constant when they are subjected to the ultrasound waves otherwise the equations become more complex in non-linear propagation consideration.

1.4. Beamforming and image formation

The delay-and-sum beamforming technique presented in Figure 1.4 is the most used in today imaging scanners. It consists in introducing delays (τ_n) on the probe individual elements excitation in such a manner that their responses reach at the same time the target area called the focal point. The pressure summation gives a high intensity signal which provides a better image resolution and an important penetration depth in the medium

explored. In this beamforming technique, linear scanning is made by applying the delay on a set of elements for each image line whereas in phased scanning the delay is applied to the whole probe. In this technique, the beam is performed in the same time for all frequencies [Chitre and Potter (1998)]. To obtain a more uniform beam, specific apodization coefficients can be applied to the array elements. The common apodization functions used are the windowing function such Hanning, Hamming, Blackman, etc… but any other customized apodization function can be applied. The default apodization is the rectangular window in which all elements have the same coefficient value.

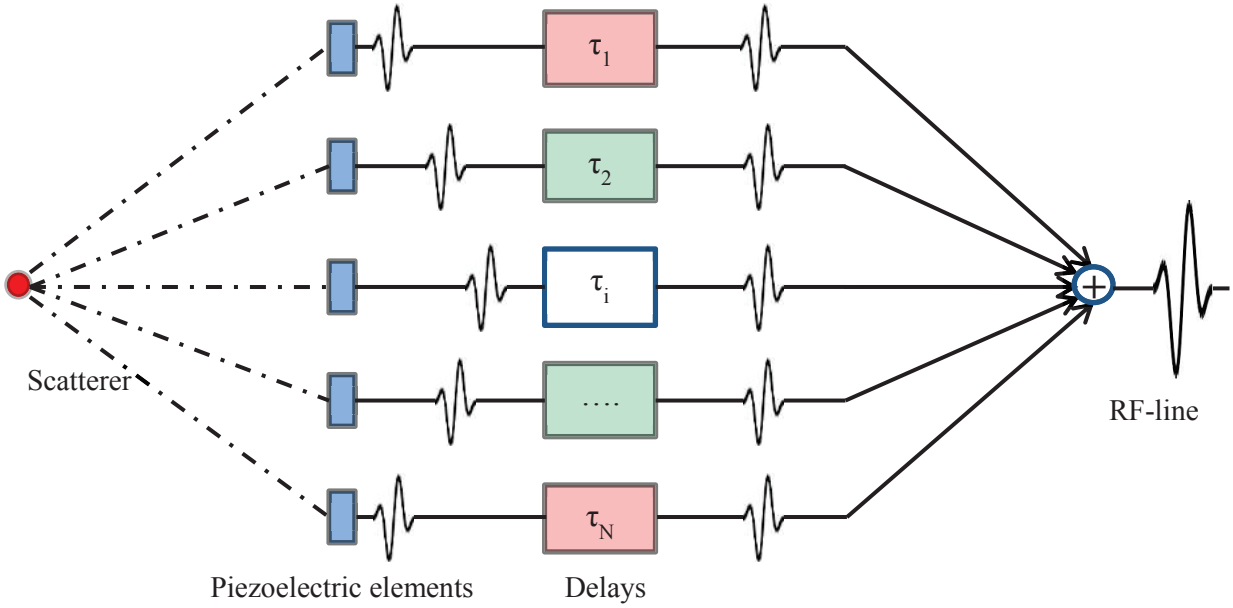

Figure 1.4 : time domain beamforming technique mostly used in the current ultrasound imaging scanners. The delays are proportional to the distance between the elements and the focalization point, they permit to steer the beam in any direction on a plane for 1D array and in the whole space in case of 2D matrix arrays. They also define the shape of the images.

Each single piezoelectric element transmits an ultrasound beam. This beam presents a weak energy and a large directivity whereas high energy and thin beams are needed for good resolution images. To increase the beam energy and make thinner its directivity, several elements transmit together with delayed signals in such way to obtain a summed beam at a focalization point (Figure 1.4). The same technique is used in reception. The image lines received by the ultrasound probe are high frequency signal known as RF-lines. These lines contain all the information about the medium and permit to determine the depth and the amplitude of the different interfaces in the medium. An image is composed of several such RF-lines. The image in RF-mode is not easy to interpret as the RF signals oscillate. To reduce the dynamic range of the received signals (the ratio between high and low amplitude signals) for efficient display, logarithmic compression is applied to the envelope of the RF-image obtained by Hilbert Transform. The amplitudes are converted to grayscale spots giving the B-mode images, B meaning the brightness. This latter is the most used imaging mode in medical ultrasound. As ultrasound is attenuated when going deep, an amplifier (TGC: Time Gain Compensation) is used to compensate the signal attenuation as a function of the depth. The signal processing and display are realized in the scanner which permits the storage of the acquired data.

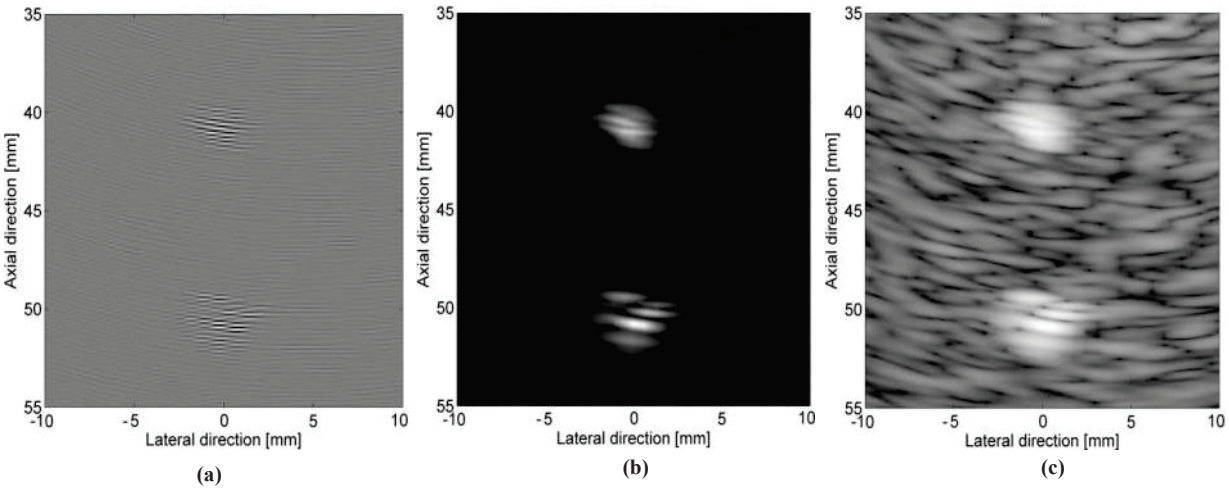

Figure 1.5: images of a cyst phantom simulated by FIELD II (a) RF-image, (b) envelope image and (c) log-compressed image called B-mode. The RF image is the most complete one containing all the information about the medium but its interpretation is difficult. The envelope image in linear scale does not permit correct view of the low amplitude zones and hence the use the log-compressed image.

The image in Figure 1.5a represents an RF image, it contains all the information about the medium but is not suitable for visualization. The signal envelope (Figure 1.5b) obtained by the Hilbert Transform allows a better distinction of the different interfaces of the medium but the background (low amplitude signals) is not clearly visible. The log-compressed signal deriving from the envelope shows all the texture of the medium and is easy to interpret. Because of that suitability, the B-mode image (Figure 1.5c) is the most used routinely in the medical domain. There are three basic transducer designs in ultrasound imaging depending on the scanning type (image shapes or field of view)): the linear, the phased array and the curved transducers [Brant (2001), Yen and Smith (2002)].

The linear transducer (Figure 1.6a) produces rectangular images which width is determined by the physical size of the transducer, the associated scanning type is the linear scanning. This type of transducers gives a good overall image quality and is adapted mainly to the exploration of shallow organs. The phased array (or sector) transducer (Figure 1.6b) is small and performs sectorial scanning producing pie-shaped image slices which are narrow in near field and provides a wide view in the far-field. This type of scanning is optimal for large organs imaging between the ribs as the transducer is small. The curved transducer (Figure 1.6c) is a hybrid type between the linear and the sector transducers. It permits a wide view in both near and far-field [Brant (2001), Yen and Smith (2002)].

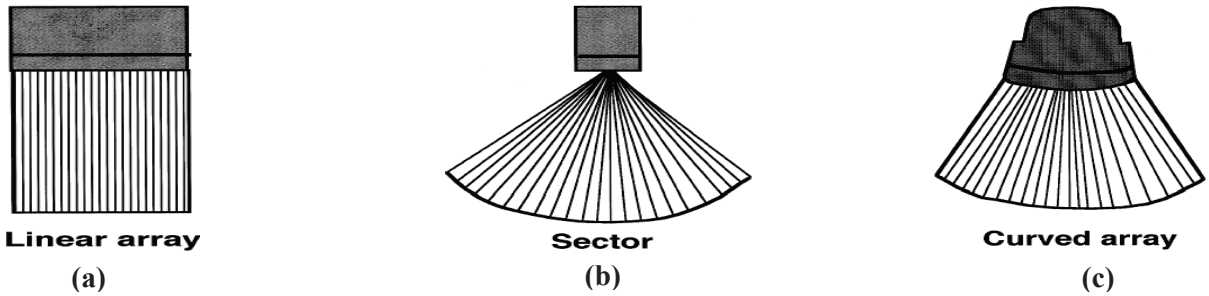

Figure 1.6: different scan types in classical 1D ultrasound imaging. (a) linear scan adapted to shallow organs, (b) Sectorial scanning preferred for large and deep organs and (c) the curved scanning conjugating the advantages of the two first scanning types [Brant (2001)].

1.5. Simulations tools

The literature describes many simulation tools for ultrasound imaging each having its strong and weak points. Many of these tools use the spatial impulse response concepts developed by [Tupholme (1969)] and [P. R. Stepanishen (1971), Peter R. Stepanishen (1971)]. The most known and the most reliable of these tools is Field II [Jensen and Svendsen (1992), Jensen (1996)], but it is limited to linear ultrasound simulation. This software was the first one in ultrasound imaging domain which proposed models comparable to the real case taking into account all the parameters of the piezoelectric elements (size, apodization) and the propagation medium. In our work, we focus on the 2D matrix arrays implemented in field II. Other simulation tools are proposed in the literature with comparable results [Varray et al. (2010), Matrone et al. (2011)].

The PSF (Point Spread Function) is the image obtained from a point source (scatterer). This function characterizes the probe imaging capabilities giving its spatial resolution (in lateral and elevation direction), the axial resolution being determined by the probe transmitting frequency. As classically in signal processing, the image of the given medium is the convolution between the probe PSF and the impulse response of this medium, under the conditions of linearity and homogeneity. Let's considerer for the PSF the function F(x, y, z) and for the medium T(x, y, z), the RF image noted I (x, y, z) can be approximated as in [Meunier and Bertrand (1995)] by

$$I(x,y,z) = F(x,y,z) \otimes T(x,y,z) \tag{1.13}$$

where $\otimes$ is the convolution product function and (x, y, z) the spatial coordinates. In case of the 2D B-mode images this equation remains valid but with only two coordinates [Bamber and Dickinson (1980), Seggie et al. (1983)].

1.6. Limitations of echography

Ultrasound imaging helps the physicians in the diagnosis and therapy but there are some parts of the human body that cannot be imaged by ultrasound. The organs containing gas like the lungs cannot be explored by ultrasound. This is due to the great acoustical impedance difference that makes all the transmitted waves reflected back. The same effect is noticed for bones; only their outer layers can be seen as explained in the equation (1.12). Ultrasound is subject to an important attenuation which makes difficult the imaging of deep organs. This attenuation is much influenced by the probe frequency; high frequencies give better image resolution but they cannot go deep. The classical 1D array cannot represent volume structures but just thin slices which give very few information about the explored media.

1.7. Conclusion

Generalities on ultrasound imaging are detailed in this chapter. The echography is an imaging modality which is completely harmless for the patients and makes easy the diagnosis for the physicians. The ultrasound scanners are portable and affordable conversely to the equipment of many other imaging modalities (CT, MRI, DetScan). The domain is constantly developing and some limitations of the classical 1D imaging are being solved using the 2D arrays.

In the next chapter, the state of art in 3D imaging is reported. The evolution in the ultrasound arrays from 1D to the full 2D arrays to provide better images and representations of the structures is discussed. The different element reduction techniques applied to the 2D matrix arrays, the mathematical background of these arrays and some prototypes of 2D arrays currently available for research purposes or commercially available are presented. The chapter ends with optimization algorithms.

Chapter 2

State of the art

In this chapter, the principle of 3D ultrasound imaging, reconstruction techniques and the different evolutions of the ultrasound imaging probe from its early beginning to nowadays are presented. The advantages and drawbacks of each step of this evolution are detailed. An important part of this chapter is dedicated to the 2D arrays imaging capabilities, the mathematical background, the obstacles and the possible solutions to their design to permit a routinely use in everyday diagnosis. Special attention is reserved to the sparse array techniques and the simulated annealing algorithm used for the array optimization.

2.1. Introduction

Ultrasound imaging domain knows an increasing development and the probes get more and more sophisticated to provide realistic representation of the media. The evolution of the ultrasound probes in time follows the advances in electronics which make possible the control of more and more active elements. In this context 3D imaging using 2D matrix array probes is one of the most attractive and exciting challenges.

2.2. Basic principles of 3D echography

2.2.1. Beamforming techniques

Beamforming is the general term used to refer to the different techniques used to combine the individual elements of an ultrasound array to produce an image. The beamforming can be realized with focalized beam or without any focalization. A beamformer aims at performing [Thomenius (1996)]

- The control of elements delays and weighting coefficients during transmission
- The control of delays and necessary signal processing during the reception
- The summation of different delayed echoes in reception and other possible operations due to the particularity of the application intended.

The principal objectives in general are to obtain the narrowest and the most intense beam with lowest possible sidelobes level and to be able to explore the media in depth without important attenuations. There can be other, more original, objectives of the beamforming, like e.g. the formation of specific images featuring transverse oscillations to better estimate transverse motion or stain [Liebgott (2010), Liebgott et al. (2006)]. The beamforming can be done analogically or numerically [Thomenius (1996)] in the temporal or in the frequency domain [Chitre and Potter (1998)]. There are several beamforming techniques used in today's classical ultrasound imaging devices and the most known is the "delay and sum" technique.

2.2.1.a Time domain beamforming (Delay and sum)

The delay and sum beamforming method (Figure 1.4) is already presented in the Section 1.4. It represents the standard beamforming technique in ultrasound imaging.

2.2.1.b Frequency domain beamforming

The frequency domain beamforming is an attractive alternative to time domain beamforming. It has been used a lot in 2D imaging [Mucci et al. (1984), Maranda (1989)] to exploit the fastness of Fourier transform. There are two main groups in frequency beamforming: the direct methods and the approached methods [Maranda (1989)]. All these techniques have been adapted to the 3D imaging in recent studies [Zhang et al. (2002), Dhanantwari et al. (2004), Murino and Trucco (1994)].

2.2.1.c Parallel processing

The parallel processing technique is a promising technique for real time 3D volumetric imaging. This technique is used by several researchers such as those from Duke University in the USA, one of the most advanced teams in the conception of 2D arrays for 3D imaging. They developed their own parallel beamforming algorithm known as Explososcan [Shattuck et al. (1984), Smith, Pavy et al. (1991)] which permits to perform real time volumetric acquisitions. With a 256 channels beamformer at transmission and reception, they have been able to produce until 30 volumes per second [Light et al. (2008)] by creating 16 image lines at each single transmission [Ramm and Smith (1990)]. In industry, a dense array probe of 3000 elements made by Philips (Sonos 7500) used at a frame rate of 20 volumes/second uses also the parallel processing. The 3000 elements are integrated on an ASIC in the head of the probe and the received signals are collected together to be funneled by 128 channels towards the processing system [Savord and Solomon (2003)]. To realize this probe, they use two methods: configurable array and sub-array beamforming.

2.2.1.d Configurable array

In the configurable array, any single element can be dynamically connected to its neighbors by activating four programmable switches which surround it (Figure 2.1). Depending on the interest area to explore and a suitable switch choice, an equivalent 1D probe can be obtained in any direction (lateral, diagonal, elevation) as shown in Figure 2.1**.** Volumetric acquisition is relatively easy in this configuration as array elements can be activated in any direction and the acquired signals are multiplexed in the probe head to avoid the use of supplementary channels compared to a 1D probe. The technique drawback is the noise produced by the opening and shutting operations of the switches which deteriorate the image signal-to-noise ratio.

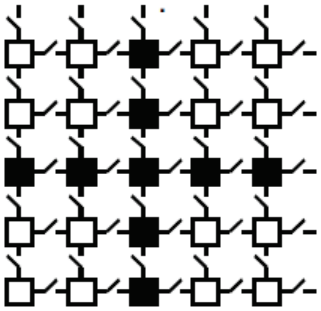

Figure 2.1 : reconfigurable array. Gray elements are connected [Savord and Solomon (2003)]. By acting different switches, different 1D arrays can be formed in each direction and leading to a row-column-like configuration.

2.2.1.e Sub-array beamforming

The sub-array beamforming method functions as the classical 1D beamforming but in two steps. Each sub-array (3000/128 elements) produces a 1D ultrasound beam which are then funneled through the 128 channels in parallel (Figure 2.2). This parallelization avoids the use of supplementary channels and reduces the system complexity in reception. With this configuration, the probe can reach a great frame rate, 20 volumes/second for the Sonos 7500.

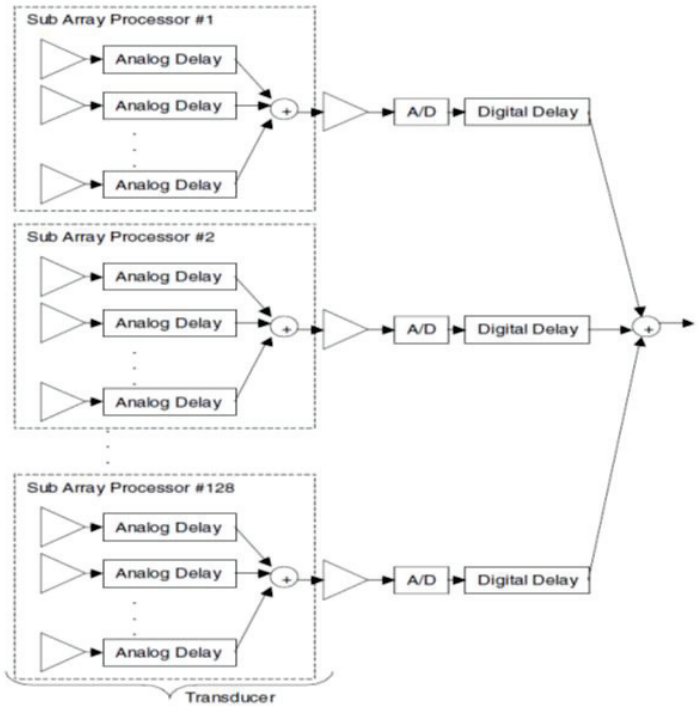

Figure 2.2 : beamforming using sub-arrays. The 3000 channels in the probe head are brought together into just 128 channels at the probe handle by multiplexing them [Savord and Solomon (2003)].

2.2.2. Array and beam parameters

For arrays composed of more than one row of elements (from 1.25 D to full 2D), the lateral direction is the largest dimension (most of the time following the x axis) and the elevation direction is the smallest direction and is along the y axis. For squared arrays, the two directions are identical. The propagation direction is along the z axis, θ is the lateral angle

between the steering direction and the z axis. This angle is in the plane x-z whereas φ in the x-y plane is the elevation angle (Figure 2.3a).

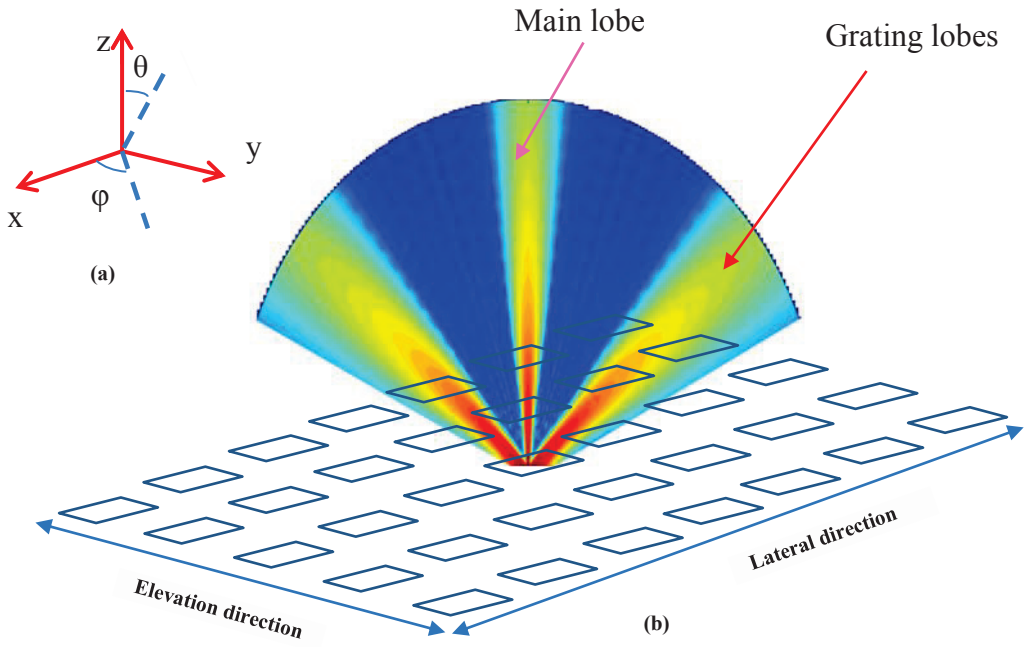

Figure 2.3: (a) 3D reference system and (b) the main parts of the 2D arrays beam. The beam is composed of main lobe (useful part) and the grating lobes (unwanted parts). The propagation direction is z, the lateral direction is along x and the elevation direction along y.

The beam pattern of these arrays is composed of two main parts: the main lobe and the grating lobes (Figure 2.3b). The main lobe is the useful part of the acoustic beam whereas the grating lobes are unwanted lobes outside de imaging direction. The latter are linked to the spatial periodicity and the size of the elements in relation to the wavelength. They constitute the main unwanted parts of the beam. A third part, the sidelobes depends on the weighting (or apodization) coefficients and the spatial distribution of the connected elements.

2.2.3. 3D volume reconstruction

The reconstruction is the technique used to interpolate classical 2D slices to 3D-like structures. Both 3D mechanical and matrix arrays allow volumetric acquisition but with different fastness. The first 3D imaging was performed by the user's manual displacement of the 1D probe and is known as freehand 3D ultrasound imaging [Gee et al. (2002), Housden et al. (2008)]. Sophisticated reconstruction algorithms are proposed in the literature to correct the imprecision in the slice acquisition but this technique remains difficult to use routinely. Later motorized probes were introduced to automatize the 2D planes acquisition and to maintain a constant scanning step between different slices composing the volume. These mechanical probes construct volumes by acquiring several 2D images using a stepper or a continuous current motor (seldom) which speed is about 1 rad/s (or 60 degrees/s) for most of them [Pospisil et al. (2010)] and this limits the volume rate. In general 3D mechanical probes produce between 1 to 4 volumes/second (volume of 25 to 50 images, 50 to 100 lines /image) depending on the number of planes (explored sector) and the depth of penetration. Many 3D volume reconstruction techniques using the mechanical probes have been made and the main techniques are the pyramidal and the rotational techniques. A complete summary of the

exiting acquisition protocols in 3D imaging is listed in [Gee et al. (2003)]. The difference between these methods comes from the coordinates system used and more importantly the application domain [Gee et al. (2003)].

The coordinates of the different planes in pyramidal volume imaging can be expressed by using the 3D rotation matrix R_x (2.1). In this case the x axis is fixed and the rotation is made around y and z axis. This kind of scanning gives parallel planes in the elevation direction and permits to reconstruct pyramidal volumes [Belohlavek et al. (1993), Smith n.d.] (Figure 2.4a). It is similar to the method used in 3D mechanical volume imaging. The angle θ is in the lateral direction (x axis) and φ in the elevation (y axis). The scanning is performed in the sector range from $-\alpha/2$ to $\alpha/2$ (α being θ or φ).

$$R_x = \begin{pmatrix} 1 & 0 & 0 \\ 0 & \cos(\varphi) & -\sin(\varphi) \\ 0 & \sin(\varphi) & \cos(\varphi) \end{pmatrix} \tag{2.1}$$

In the 2D imaging, the coordinates of a plane are given

$$\begin{cases} x = d_{focus} * \sin(\theta) \\ y = 0 \\ z = d_{focus} * \cos(\theta) \end{cases} \tag{2.2}$$

These two equations give the final expression in the 3D pyramidal imaging

$$\begin{cases} x = d_{focus} * \sin(\theta) \\ y = d_{focus} * \cos(\theta) * \sin(\varphi) \\ z = d_{focus} * \cos(\theta) * \cos(\varphi) \end{cases} \tag{2.3}$$

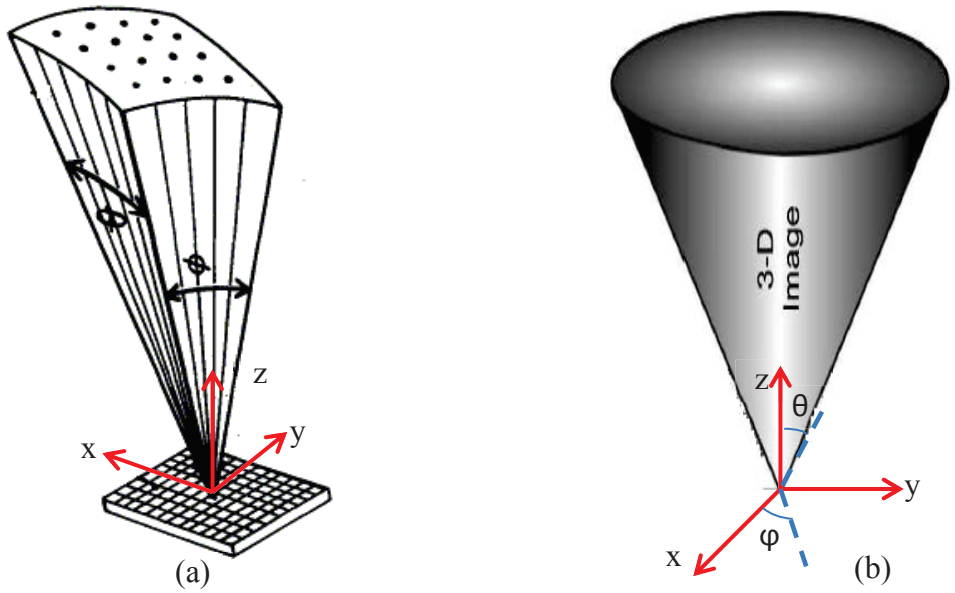

Figure 2.4: (a) the pyramidal [Belohlavek et al. (1993)] and (b) the rotational [Tekes et al. (2011)] 3D scanning strategies. The pyramidal scanning is inspired from the mechanical 3D imaging whereas the conical scanning uses the spherical coordinates to generate rotating planes.

The rotational configuration is adapted to surgical tools tracking as biopsy needles [Bax et al. (2008)] and deep intern organs imaging such as the liver and the prostate. The different steps of a rotational volume reconstruction are detailed in [Nikolov et al. (2003), Krenning et

al. (2003)]. The spherical coordinates are used and the resulting image is a cone-like volume [Tekes et al. (2011)] (Figure 2.4b). The lateral angle θ between the x and z axis allows the plane scanning while the elevation angle φ between x and y permits to change the plane position in the cone. The angle θ varies from 0 to 180 degrees and the scanning is performed between $-\theta/2$ to $\theta/2$ to provide symmetrical planes. In the elevation, θ ranges from 0 to 360 degrees but in practice 180 degrees are enough because of the properties of symmetry.

$$\begin{cases} x = d_{focus} * \sin(\theta) * \cos(\varphi) \\ y = d_{focus} * \sin(\theta) * \sin(\varphi) \\ z = d_{focus} * \cos(\theta) \end{cases} \quad (2.4)$$

The rotational scanning permits to simultaneously visualize perpendicular planes to characterize the lateral and the elevation imaging features of the 2D arrays.

In 2D arrays, high frame rates (some tens volumes/second) can be reached thanks to the electronic steering. In some imaging modalities such as optical coherence tomography for cardiac imaging [Happel et al. (2011), Larina et al. (2012)], 4D (3D+t) imaging is already possible in real time. A 4D imaging mode is present on some commercial scanners for obstetrics applications dedicated to the following of the fetus development status. For the moment, obtaining accurate information about these systems is difficult because the frame (or volume) rate depends a lot on the experimental parameters as the exploration depth, the central frequency and the volume size.

2.2.4. Application domains

3D ultrasound imaging has many applications, it can replace the classical 2D imaging in almost all the using domains of the latter. The main applications domains are prostate, liver and cardiac imaging using both 3D mechanical probes [Bax et al. (2008), Kneif et al. (2009)], and 2D arrays [Light et al. (1997)]. The 2D arrays permit to increase the volume rate and to accede to more information mainly about the c-scan planes (perpendicular planes to the beam direction). For example in biopsy guidance, the visualization of the c-scan planes is extremely important since such planes usually contain the needle tip and the tumor contours.

Examples of such applications are presented in literature [Ding and Fenster (2003), Linguraru (2006), Okazawa et al. (2006), Wu Qiu et al. (2008), Aboofazeli et al. (2009), Uherčík et al. (2010)]. Other examples include cardiac and obstetric imaging performed at Duke university with different 2D arrays [Light et al. (1997)].

2.3. Intermediate arrays

Intermediate arrays are arrays containing not only one line of transducers as the 1D but not enough to be considered really as 2D arrays. The objective of these arrays is to produce volumetric imaging without any displacement to correct the imprecision of 1D and 3D mechanical arrays. Such arrays provide a solution to the elevation resolution problem thanks to their capability to focus ultrasonic beams in the two directions (lateral and elevation). There are three main notations for the intermediate arrays described hereunder: 1.25D, 1.5D and 1.75 D array.

2.3.1. 1.25D array

The main difference between 1.25D and the classical 1D array is the number of elements in the elevation direction; the 1.25D has at least three rows of elements in the elevation direction (Figure 2.5). The outer row elements are symmetrically connected together and connected to the unique channel of the probe. A multiplexor placed in the probe head permits the transit of all data (from outer and inner rows) to the channel. In practice, the outer row elements size is chosen in such a manner that after their connection together, they give the same size as the inner (central) element. This permits to have the same impedance and the same acoustical sensibility for outer and inner rows [Wildes et al. (1997)].

The increase in the row number allows the 1.25D array to have a better elevation resolution than 1D array without any additional extra-channel count. Its drawback is its incapacity to displace the focal area in elevation; the focal point remains static like in 1D imaging. The simulations results realized by [Wildes et al. (1997)] put in evidence the image resolution improvement compared to 1D probes in both the near and the far field even though the system complexity increases a little due to multiplexor cables.

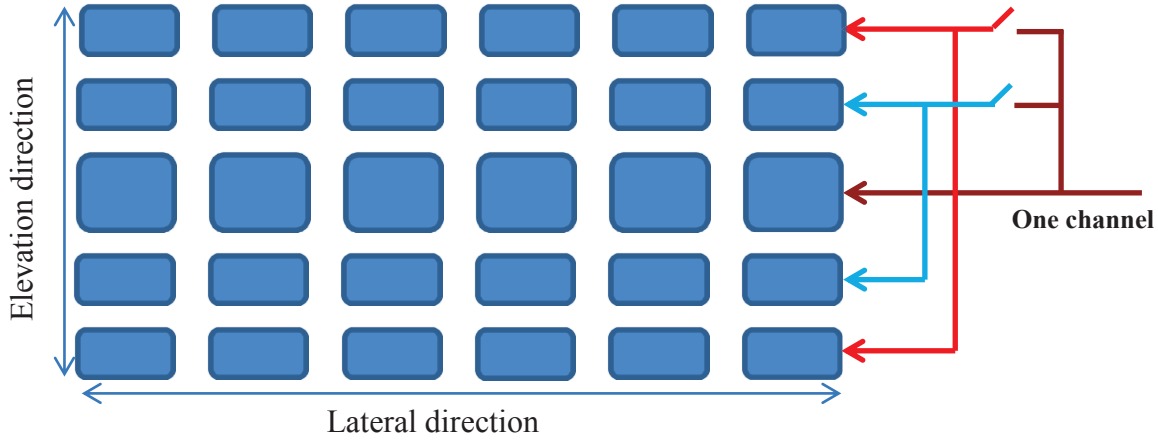

Figure 2.5 : 1.25D array of 5 rows with outer row elements connected together by twos symmetrically to the central (inner) row. Inner row is twice larger than the outer ones to maintain the same acoustical impedance and sensitivity for outers and inner elements.

2.3.2. 1.5D array

The 1.5D array can contain the same element number as the 1.25D (from 3 to 7 rows in general [Barthe and Slayton (1996), Lacaze et al. (1998)]) but the major difference comes from the element connection technique. Conversely to 1.25D where all rows use the same channel, in the 1.5D array outer rows are also connected by two symmetrically to the central row but each pair of rows has its own channel as shown in Figure 2.6. This configuration of outer rows allows dynamic focalization by applying a suitable delay times on them during transmission and reception as presented in many studies [Angelsen et al. (1995), Tournois et al. (1995), Lacaze et al. (1998), Curiel et al. (2002)].

The focal area remains always symmetrical in relation to the center of the probe and can move between two extreme elevation positions but no steering is possible in elevation [Wildes et al. (1997)]. For this reason, the rows in 1.5D array (also 1.25D) are always odd-numbered and the more rows there are the more the image resolution is improved at mid-far and far field [Daft et al. (1994), Wildes et al. (1997). Comparative studies permit to confirm

the efficiency of the 1.5D array compared to the classical 1D probe as described in [Daft et al. (1994), Shung (2002)]. Among all the intermediate probes, the 1.5D was the most investigated because of its capability of dynamic focalization in elevation and its easiness to be controlled by current beamformers. It constitutes a great step in volumetric imaging developed later with 1.75D and full 2D arrays.

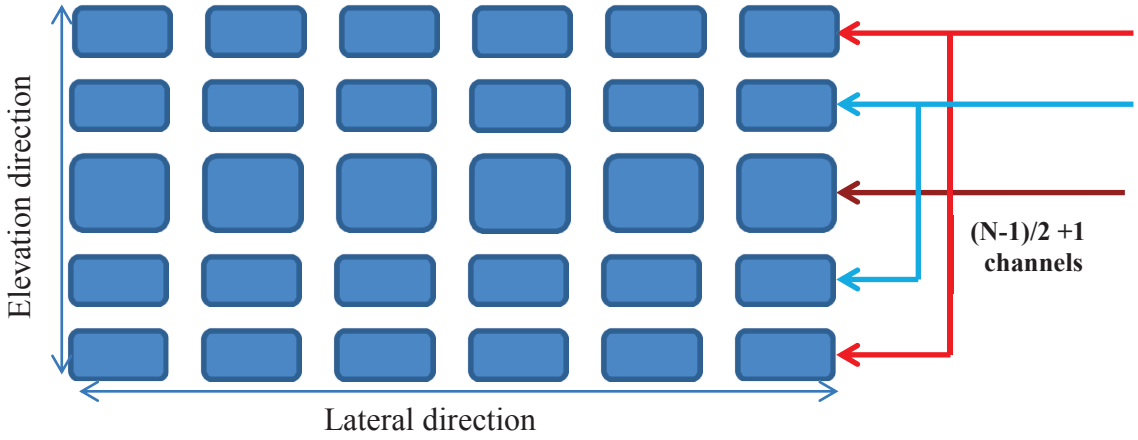

Figure 2.6 : 1.5D array of 5 rows with outer rows connected together symmetrically in relation to the central (inner) row. Each pair of rows has one channel. This array performs limited beam steering in the elevation direction around its center.

2.3.3. 1.75D array

The 1.75D array is an evolution of the 1.5D array and contains at least the same elements number as the latter. The main difference with the 1.25D and 1.5D arrays is that each element can be controlled separately. In fact in 1.75D array each element has its own channel, so there are as many elements as channels. It allows a beam steering in the whole space [Puyun Guo et al. (2001)]. An example of such an array is detailed in [Fernandez et al. (2003)] with simulation and experimental results showing its contrast and resolution improvement compared to the 1.5D array. The array is constituted of 8 rows of 128 elements manufactured by Tetrad Co., Englewood, CO and the experiments are carried out with a Siemens scanner ELEGRA of 1024 channels imaging a tissue mimicking phantom. They demonstrated the capability of the 1.75D array to steer ultrasound beams in a certain limited steering angle in elevation (about 5°). Another 1.75D array composed of 10 rows of 128 elements (approximately 1280 elements) manufactured by Tetrad Inc was studied by [Puyun Guo et al. (2001)]. They focused their study on the volumetric acquisitions capability of this probe and the angle opening consequence on the ultrasound beam form. According to all these results, for an opening angle of approximately 20 degrees (+/-10°) in elevation, the ultrasound beam is acceptable.

The only difference between the 1.75D and the 2D arrays is the number of elements. Indeed, a 2D array is ideally squared with as many elements in both lateral and elevation directions. 2D arrays constitute the current state of the ultrasound probes evolution.

A recap of the different kinds of ultrasound probes was established in [Wildes et al. (1997), Fernandez et al. (2003)] which summarizes the main characteristics of each one and the range of the elements number.

Type of probe studied	1D	1.25D	1.5D	1.75D	2D
Focalization	Lateral	Lateral	Lateral / elevation	Lateral / elevation	Lateral / elevation
Excitation	Totality	Totality	Totality	Totality	Sparse
Freedom of rows		No	Yes (by pair)	Yes	Yes
Rows number / columns number	1xN	(2-7)xN	(2-7)xN	(2-8+)xN	NxN
Electronic focalization in elevation	No	No	Yes (symmetric)	Yes	Yes
Electronic steering in elevation	No	No	No	Yes (limited)	Yes
Mechanical focalization	Yes	Yes	Yes	Yes	No

Table 2.1: recapitulative of different types of ultrasound probes and their particularity going from the linear 1D array to the full 2D arrays. In each step of evolution the image quality and the technological complexity remain the main constraints.

2.4. 2D array

The full 2D arrays are the most advanced arrays in ultrasound imaging. These arrays correspond to an extension of the classical 1D array to both lateral en elevation directions. The elements of a 2D array probe are aligned on a regular grid and spaced out of a distance (the pitch) fewer than a mid-wavelength to avoid grating lobes apparition. This inter-element distance limitation is the spatial sampling condition. This constraint leads to a multitude of small elements. The equivalent of a 1D probe of 128 elements contains 128x128 = 16,384 elements in 2D. Connecting such a high number of elements is a technical challenge as the number of channels in most of the current ultrasound scanners does not exceed 256. Even if the scanners enable the connection of these elements, its realization will necessitate too large electrical connecting cables resulting in a heavy and non-suitable probe for everyday routine operation. As a consequence, the main issue that must be tackled lays in the elements reduction techniques.

2.4.1. Dense array

The dense array is the 2D array completely filled where no reduction method is applied. The dense array is also known as the fully sampled array. It constitutes the reference array in all element number reduction studies.

2.4.1.a Standard used element positioning

The most used grid for the 2D arrays is the rectangular (or square) one (Figure 2.7a). This latter is easy to model as it is a direct extension of the classical 1D probe. Many other

grids are proposed in the literature among which the circular one (Figure 2.7b). The circular elements disposition gives a better beam pattern in terms of grating lobes compared to the square grid but it widens the main lobe [Mendelsohn and Wiener-Avnear (2002)]. Spiral configuration in Figure 2.7c was also tried in few studies with the conclusion of a slight beam pattern improvement compared to the aforementioned configurations [Tweedie et al. (2009)]. In this work we opt for the rectangular grid as reference configuration.

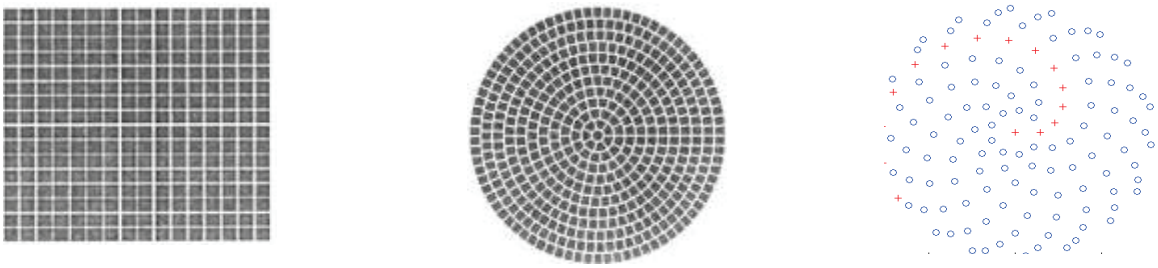

Figure 2.7 : different elements configuration of 2D arrays [Mendelsohn and Wiener-Avnear (2002), Tweedie et al. (2009)]. (a) rectangular(or square) ,(b) circular and (c) spiral elements disposition configuration.

2.4.1.b Theoretical expression of the 2D array beam

In the literature, many theoretical expressions of the beam are presented depending on the grid type. Let's consider the simple case of a 2D array used in a sectorial scan presented by Figure 2.8. The distance d represents the inter-element distance (pitch), w the element's size and θ and φ the lateral and elevation angles.

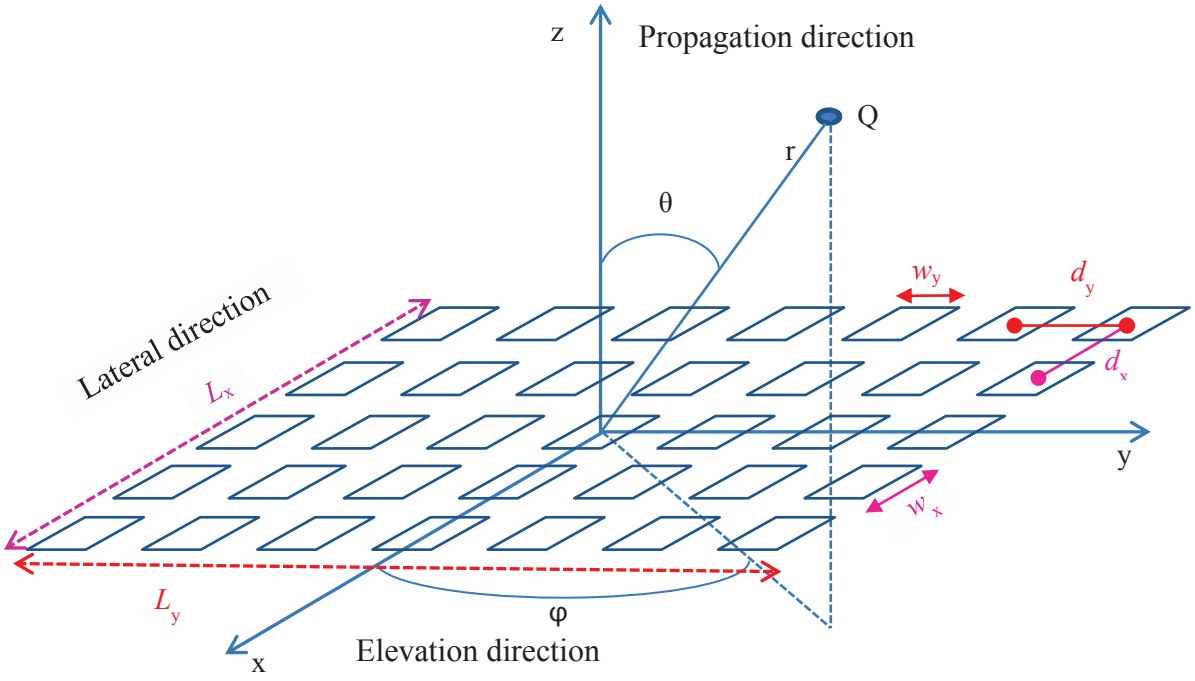

Figure 2.8 : 2D linear array and its coordinate system

The formula expressing the impulse response of a 2D array composed of rectangular elements presenting a spatial periodicity of d (pitch), with dimensions L_x, L_y in lateral and

elevation directions respectively was presented in [Brandwood (2012)] by the following equation

$$H_s(r,\theta,\varphi,\lambda) = \frac{L_x L_y d_x d_y}{2\pi r}\sum_{m=1}^{M} sinc\left(\frac{L_x}{\lambda}(u - m\lambda/d_x - u_s)\right)\sum_{n=1}^{N} sinc\left(\frac{L_y}{\lambda}(v - n\lambda/d_y - v_s)\right), \quad (2.5)$$

in which u and v are the beam direction vectors and u_s and v_s are their values in case of a steering angle θ_s in the lateral direction and φ_s in the elevation direction, M and N are the number of elements in the corresponding directions and λ is the wavelength.

$$u_s = \sin(\theta_s)\cos(\varphi_s) \quad (2.6)$$

$$v_s = \sin(\theta_s)\sin(\varphi_s) \quad (2.7)$$

$$L_x = (M-1)d_x + w_x \quad (2.8)$$

$$L_y = (N-1)d_y + w_y \quad (2.9)$$

The position of the grating lobes in the 2D array correspond to the zeros of the $sinc$ function located at the following positions as expressed in [Turnbull and Foster (1991), Gori et al. (2000), A. Austeng and Holm (2002)]

$$u_g = u_s \pm n\lambda/d \quad (2.10)$$

$$v_g = v_s \pm m\lambda/d \quad (2.11)$$

with θ_g and ϕ_g the grating lobes positions in lateral and elevation direction.

The equations (2.10) and (2.11) confirm that for a given wavelength λ, the bigger is d the closer to the main lobe are the grating lobes and inversely. As there is no efficient manner proposed currently to reduce the grating lobes, the challenge in terms of beam profile is in finding a good tradeoff between the main and grating lobes. In some configurations, the grating lobes can be higher than the main lobe if the angles respect the condition of $|\theta_g| < |\theta_s|$ (or $|\varphi_g| < |\varphi_s|$)which leads to completely wrong imaging [Gori et al. (2000)]. Theoretically the condition to avoid the grating lobes is the spatial sampling condition clearly explained in [Holm (2000), Holm et al. (2001)] and reprised in [Weber et al. (1994), Lockwood and Foster (1996), A. Austeng and Holm (2002)]

$$d < \lambda/2\,. \quad (2.12)$$

If $d = \lambda/2$, with the assumptions of $\theta_s = 0$ and $\varphi_s = 0$, equation (2.11) becomes $\sin(\theta)\sin(\varphi) = 2$ is not defined, so any grating lobe exists at this pitch value. But for values of d between $\lambda/2$ and λ equations do not give precise information about the grating lobes positions even if they exist. Turnbull et al [Turnbull and Foster (1991)] showed that the

grating lobes occur in the array response even if the element spacing is less than $\lambda/2$. This is due to grating lobe contributions coming from the higher frequencies of the pulse. Today, the compromise in a 2D array design resides in the choice of the element size which must be slightly larger than $\lambda/2$ to obtain a better main lobe but not too much to limit the grating lobes effect. Solutions to overstep the equation (2.12) will open lot of possibilities in the 2D arrays imaging capabilities.

The pressure generated by a 2D array when excited by a pulse $e_T(t)$ ($E_T(f)$ is Fourier transform of $e_T(t)$) depends on the elements factor and the element positions in accordance with the field point [Turnbull and Foster (1991), Brandwood (2012)]

$$P(r,\theta,\varphi,f) = E_T(f) w_x w_y sinc\left(\frac{w_x u}{\lambda}\right) sinc\left(\frac{w_y v}{\lambda}\right) \times \text{Obliquity Factor}. \tag{2.13}$$

Equation (2.13) highlights the importance of the element size on the amplitude of the transmitted and received signal. The element factor behaves as a modulation signal in the whole probe beam pattern [Brandwood (2012)].

These same remarks can be made using the integral formulation of the acoustical field of 2D arrays. In the integral formulation, the theoretical demonstration of the relation between the element size and the probe energy is shown by equation (2.14). Assuming the array to an infinite planar baffle of surface S composed of several infinitesimal surfaces *ds*, the radiated pressure at a distance $|\overrightarrow{r_0}|$ from the array can be expressed using the Rayleigh integral

$$P(\overrightarrow{r_0},t) = \rho \int_S \frac{1}{2\pi|\overrightarrow{r_0}|} \frac{\partial v_n(\overrightarrow{r_0},\ t-|\vec{r}|/c)}{\partial t} ds \tag{2.14}$$

where ρ is the density of the medium,v_n the normal acoustical velocity to the array surface, *c* the sound celerity and $|\vec{r}|$ is the distance from the aperture to the observation point. This pressure function (2.15) is a convolution between the array PSF (2.16) and the derivative of the normal velocity v_n [Matrone et al. (2010)]

$$P(\overrightarrow{r_0},t) = \rho \frac{\partial v_n(t)}{\partial t} \otimes h(\overrightarrow{r_0},t) \tag{2.15}$$

where the analytical expression of h is known as

$$h(\overrightarrow{r_0},t) = \int_S \frac{\delta(t-|\vec{r}|/c)}{2\pi|\vec{r}|} ds \tag{2.16}$$

where δ is the spatial Dirac function.

To compute the PSF of a 2D array composed of *M*x*N* elements, the integral is discretized and the final expression of the equation (2.16) becomes

$$h(\overrightarrow{r_0},t) = \sum_{i=1}^{M}\sum_{j=1}^{N} w_{ij} \frac{\delta(t-|\overrightarrow{r_0}-\overrightarrow{r_{ij}}|/c-\tau_{ij})}{2\pi|\overrightarrow{r_0}-\overrightarrow{r_{ij}}|} \Delta s_{ij} \tag{2.17}$$

where w_{ij} are apodization coefficient, τ_{ij} the delays shown in Figure 1.4 and Δs_{ij} the element surface. These equations put in evidence the theoretical basis about the importance of the array active surface on its beam.

The possibility of decoupling between the 2D array beam characteristics in the lateral and elevation direction was demonstrated by [Smith et al. (1991)]. The lateral and elevation spatial resolutions are defined using the Rayleigh criterion and equal

$$\Delta\theta = sin^{-1}(\lambda/L_{\mathrm{x}}) \tag{2.18}$$

$$\Delta\varphi = sin^{-1}(\lambda/L_{\mathrm{y}}) \tag{2.19}$$

and in the case in which the same array is used in both transmission and reception, the - 6 dB beam width can be approximated by

$$\Delta\theta = sin^{-1}(0.9\lambda/L_{\mathrm{x}}) \tag{2.20}$$

$$\Delta\varphi = sin^{-1}\left(\frac{0.9\lambda}{L_y}\right). \tag{2.21}$$

The equations (2.18) to (2.21) prove that to obtain a good spatial resolution (thin main lobe) for a given working frequency the probe must be as large as possible.

2.4.1.c Rectangular array design

The reference array used to illustrate the beam profile of the 2D arrays is a rectangular array. Its central frequency is chosen to be suitable to biopsy or cardiac imaging. Classically, in liver biopsy, the common frequency range is between 4 and 9 MHz (3 MHz to 7 MHz for hepatic ablation operations) [Lee et al. (2004), Okazawa et al. (2006)]. In thoracic biopsy, most of the times the frequency varies from 3.5 MHz to 5 MHz [Liao et al. (2000), Sartori et al. (2007)], and seldom to 7.5 MHz [Herth and Becker (2003)]. Prototypes of 2D arrays studied for biopsy applications at a central frequency of 3.3 MHz exist [Girard et al. (2003)].

Depending on these references and as suggested by one of our collaborators from the Lyon hospital, the central frequency of the reference array is fixed to 3.5 MHz. This frequency allows a good penetration depth and it permits the visualization of classical surgical micro-tools. The initial probe is a 64x16 matrix array. The inter-element distance is 0.6 wavelengths (0.6 λ) to limit the grating lobes apparition. The dimensions of the array are

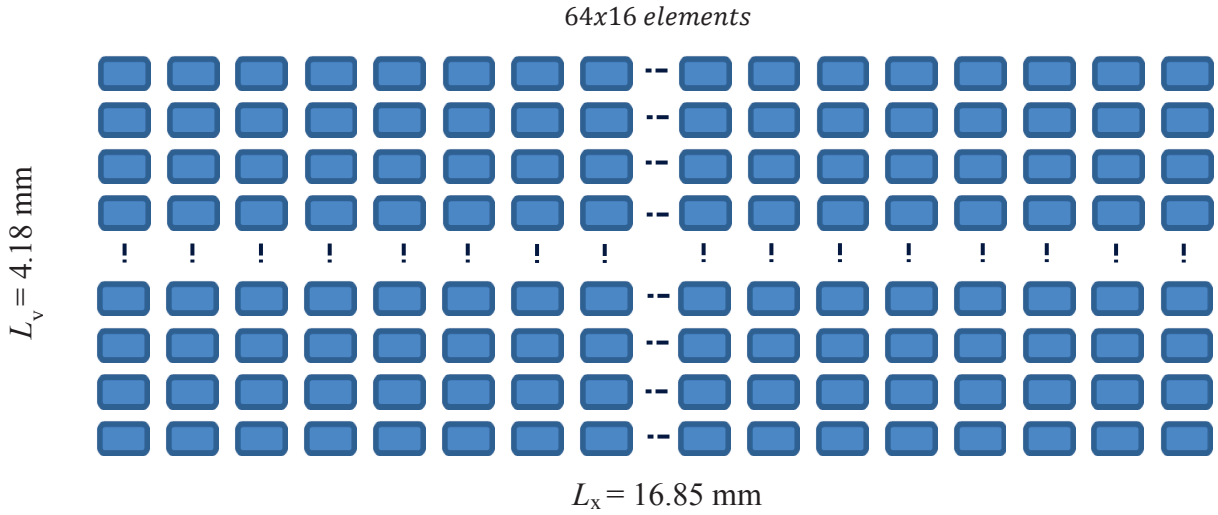

Figure 2.9 : the 2D array in x-y plane with squared elements. This 2D array is aimed for biopsy imaging and for this reason its height is chosen to be smaller than the intercostal distance 5 mm, it constitutes the reference array for the theoretical studies proposed in this work unless otherwise stated. The largest dimension (along x) is the lateral direction whereas the other (along y) is the elevation direction.

38.3λ (16.85 mm) in the lateral direction and 9.5 λ (4.18 mm) in the elevation direction.

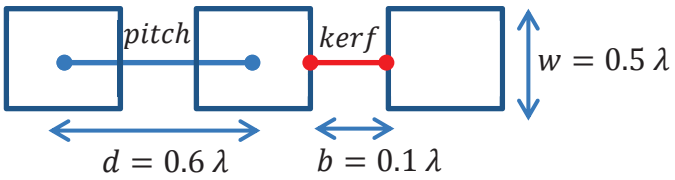

Figure 2.10 : the probe element size and their spacing

$pitch$ The center to center distance or the inter-element distance

$kerf$ The interval between consecutive elements

w The dimension of the elements

Parameters	Values
Central frequency	3.5 MHz
Element number	64x16=1024
Element dimensions (width and height)	0.22x0.22 mm²
Pitch (d)	0.264 mm

Table 2.2: the main parameters of the 2D array probe used as reference in the simulations

The size of the array in the elevation direction is imposed by the inter-costal distance which measures roughly 5 mm to take into account the possible wave reflections on the ribs. Moreover the pitch must be close to the mid-wavelength (0.22 mm) which permits

approximately a number of 22 ($\approx 5/d$) rows in elevation direction. For practical (electronic) consideration, multiple numbers of 8 are suitable for beamformers channel number adaption, so 16 rows are maintained in elevation. The full array contains 1024 elements, which is too much for the current beamformers. Element number reduction techniques are used to make possible the control of this array. The complete features of the 2D array (Figure 2.9) are listed in Table 2.2.

2.4.1.a PSF phantoms

The PSF phantoms are used to compare arrays imaging capabilities. The first phantom in Figure 2.11a is composed of five isolated scatterers (this number can be smaller or greater) placed on the probe's axis (no-steering). The position of the scatterers goes from 40 mm to 60 mm depth with a step of 5 mm. The second phantom (Figure 2.11b) presents the same characteristics but with the scatterers rotated of an angle of 45 degrees off-axis (steering) in both lateral and elevation directions. The last phantom (Figure 2.11c) contains one single scatterer placed at 50 mm on the probe axis and is used to compare the beam profile of the arrays. The latter phantom permits to evaluate the energy loss, the main lobe width and the grating lobes level of different arrays. The scanning sector ranges from – 90° to 90° in both lateral and elevation directions for all PSF simulations.

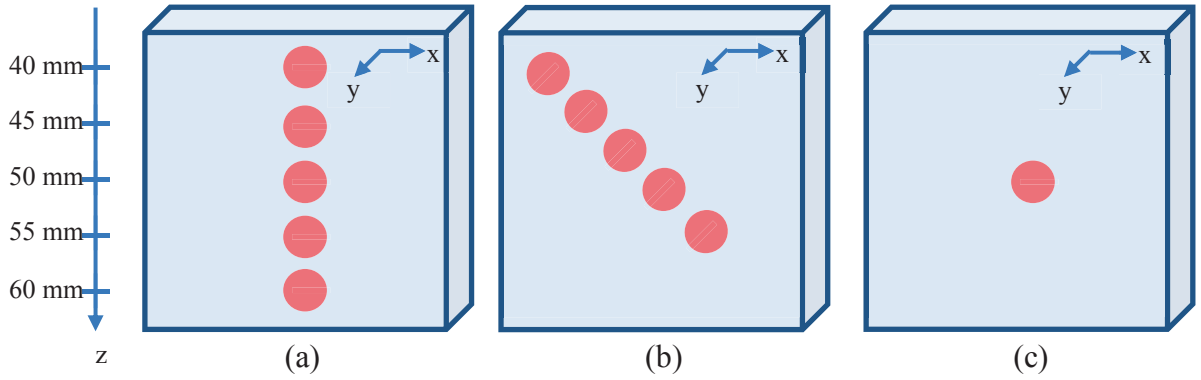

Figure 2.11: (a) and (b) represent the five-scatterer phantoms used in the PSF simulations (a) no-steering, (b) steering at (45°, 45°) in both lateral (along x) and elevation (along y) directions and (c) represents the single scatterer phantom used to perform the beam profiles comparison . All the phantoms have the same dimensions.

2.4.1.b Beam characteristics of the dense array

The beam characteristics evaluation of the proposed 2D array containing 1024 elements is performed using the phantom of (Figure 2.11c). The pressure profile in the lateral and elevation directions when the scatterer is on the probe axis (no steering) is shown in Figure 2.12. These beam profiles are obtained by plotting the non-zero values along in the lateral and the elevation direction.

The main challenges in the use of 2D arrays resides in the element number reduction, the grating lobes suppression, the increase of the array resolution making the main lobe thinner and the increase of the element size to maximize the array sensitivity improving its signal to noise ratio. The beam profiles shown in this study correspond to the worst case of the array beam in terms of grating lobes [Austeng and Holm (2002)]. The beams of Figure 2.12 are all symmetric and for this reason, when no steering is considered, the corresponding beam profiles will always be displayed on a half sector (from 0 to 90 degrees).

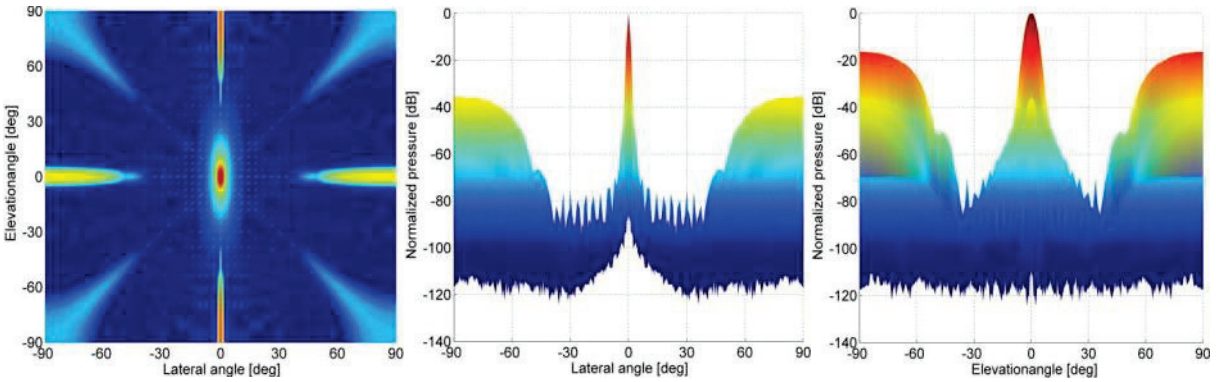

(a) (b) (c)

Figure 2.12 Simulations with FIELD II of the 64x16 arrays, (a) the perpendicular plane to the array beam at 50 mm depth (C-scan), the beam profiles in (b) lateral and (c) elevation directions. The grating lobes are located on the x-y axis center and on the diagonals as the scatterer is on the array axis at (0, 50 mm, 0). The beam profiles in lateral and elevation directions show the angles at which the grating lobes appear (+/- 40 degrees). Between the main and the grating lobes are the sidelobes.

2.4.2. Element number reduction techniques

The element number reduction techniques form two main groups: the first group successively uses subset of elements to run the whole array (synthetic aperture and row-column addressing) and the second group completely deactivates some elements (edge element deactivation and sparse arrays). The latter group (the one studied in this work) presents better perspectives for real-time 3D imaging than the first one as it provides 2D arrays completely controllable by current scanners. These reduction techniques are not necessary for small arrays used for feasibility studies highlighting the 2D array efficiency compared to the 1D probe [Weber et al. (1994), Weber et al. (1999), Austeng and Holm (2000), Eames and Hossack (2008), Fuller et al. (2008)].

2.4.2.a Row-column addressing

The row-column addressing aims at overcoming the connection problem of the 2D arrays by reducing the active elements number and to increase the frame rate. The theoretical rules of this technique was proposed by Lockwood et al [Morton and Lockwood (2003)] who proved a significant reduction capability. For a squared 2D array containing NxN elements, the application of the row-column addressing reduces the element number by a factor of N/4.

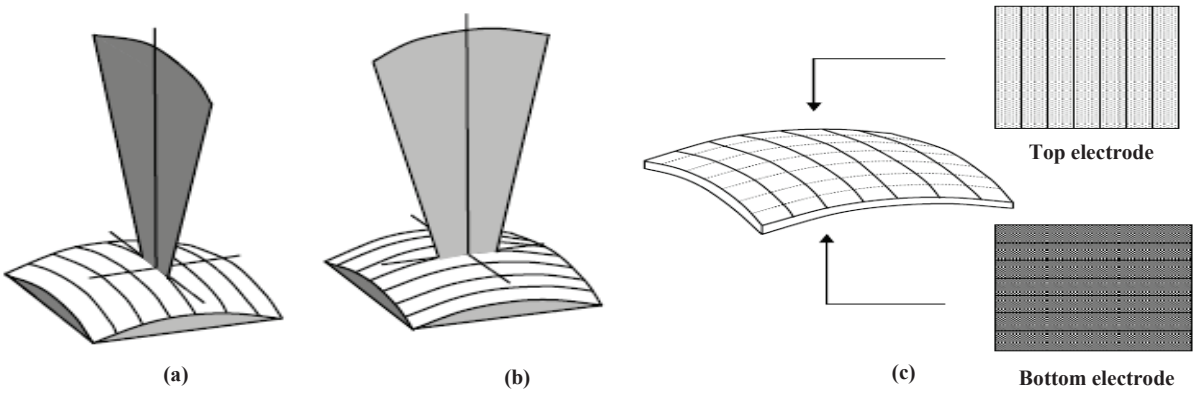

Figure 2.13: Principe of row-column addressing and fan shaped beam in (a) transmission, (b) reception and (c) the elements connection strategy [Morton and Lockwood (2003)]. In this technique only one row is used in transmission and the reception is made with several columns in such a manner to form several RF-lines with just one transmission. Studies showed the real-time 3D imaging capabilities of this technique but the image quality are too poor.

In this technique, the transmission elements are placed in elevation direction (Figure 2.13a) and those in reception are placed in lateral direction (azimuth) (Figure 2.13b). This perpendicular elements connection allows producing a lot of RF-lines simultaneously in reception with just one transmission. The probe must have a curvilinear form to facilitate the beam defocusing in elevation direction for a better reception. The elevation directivity is determined by the curvature of the probe and the scanning sector but a non-suitable modification of these two parameters can also deteriorate the lateral focalization. A trade-off must be found to optimize the beams in the two directions[Morton and Lockwood (2003)]. The 2D arrays manufactured at Duke University [Yen and Smith (2002)] uses this principle reaching a high volume acquisition rate. It produces 16 lines in elevation direction for each single transmission in lateral direction; this means for one row of elements activated in lateral direction, 16 columns are activated in elevation.

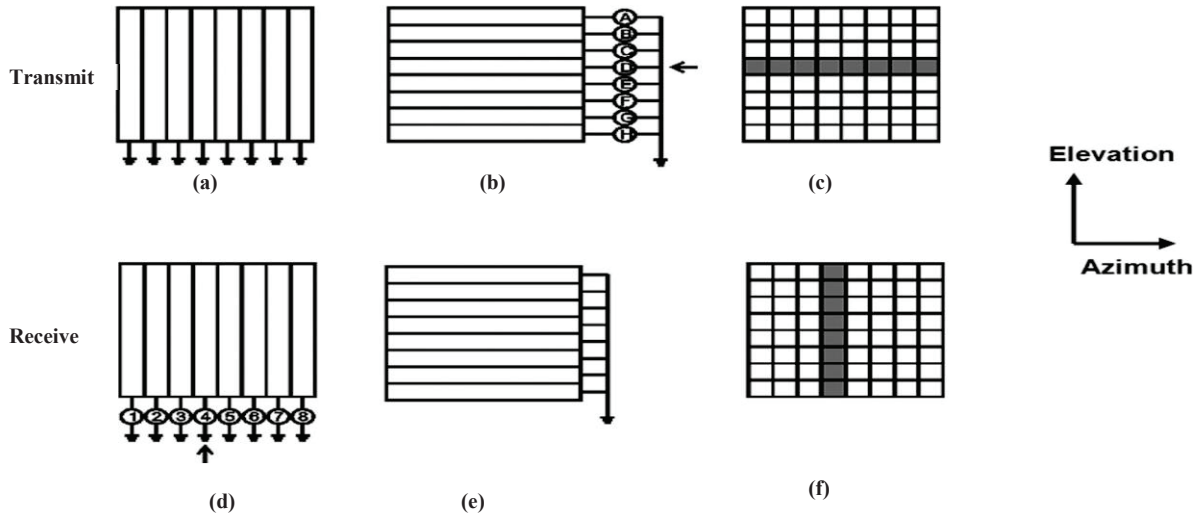

Figure 2.14 :detail of row-column addressing technique proposed by [Chi Hyung Seo and Yen (2009)] . In transmission (a) bottom electrode, (b) top electrode and (c) activated elements. In reception (d), (e) and (f) are respectively the bottom, top electrodes and the activated elements.

The technological realization of the row-column addressing applied to the 2D arrays to put in evidence the channel number reduction is described by [Chi Hyung Seo and Yen (2009)]. The printed circuit shows the two kinds of electrodes: in transmission, the columns

(Figure 2.14a) are grounded whereas the rows (Figure 2.14b) permit the connection of the channels. In reception the rows are grounded and the columns connected to the channels (Figure 2.14d-e).

The simulation results obtained are compared to experimental images acquired by an Ultrasonix RP scanner. These studies confirm the feasibility of real time volumetric data acquisition if the row-column addressing is combined to parallel processing as detailed in [Daher and Yen (2006)].

2.4.2.b Synthetic aperture

The synthetic aperture technique was applied first in telecommunications for sonar antennas and in geological applications before being retrieved in the ultrasound imaging domain [Nikolov and Jensen (2003)]. This technique consists in transmitting with a sub-array of non-focalized elements and receiving the echo with another sub-array. Nikolov and Jensen used a 32x32 2D array subdivided into 16x8 sub-arrays controlled by a 128-channels beamformer and ran all the sub-arrays successively by multiplexing. The validation of the technique was made in simulations using FIELD II [Nikolov and Jensen (2003)]. Similar studies realized on a 40x40 2D array are presented in [Jensen et al. (1999), Wygant (2006)]. The interest of synthetic aperture imaging is its capability to control 2D arrays with a small channel number by multiplexing; its drawbacks are the image signal-to-noise degradation due to non-focalized transmission, the huge amount of the stored information and its incapability to realize fast volume rates as the technique is very time consuming.

[Daher and Yen (2006)] proposed an advanced version of this technique presenting three configurations:

- Transmission by individual elements and reception by the entire row containing this element as in a 1D array imaging. The summation of separate low resolution images gives a high resolution image
- Transmission by an entire sub-array and reception with one row
- Transmission by randomly selected columns and the reception by randomly selected rows.

They noticed that the third configuration is the most promising compared to the two previous ones for 3D real time imaging. The same configuration was applied to 3D under-water imaging and the results are comparable to those of the dense array. They conclude that the time necessary for synthetic aperture 3D imaging is between one to three times more important than with the dense array [Johnson et al. (2002)].

2.4.2.c Edge elements deactivation

Most of the time, in ultrasound imaging, an apodization coefficient is applied to each element to lower energy dispersions and increase the image dynamic range [Matrone et al. (2010)]. These coefficients are chosen to favor central elements up to the outer ones. In case of large array the coefficients applied to the outer elements are so small that they don't contribute much to the resulting beam and for this reason they can be deactivated. Going from rectangular to its circular enclosed part presents a smoother beam [Turnbull and Foster (1991)]. This edge elements deactivation allows a reduction of the active element between 20% to 30% [Turnbull and Foster (1991), A. Austeng and Holm (2002), Diarra et al. (2011)]. The element number reduction from Figure 2.15a to b is 20%. 828 active elements are still too many to be controlled individually by current beamformers. The circular enclosed

configuration is a first step but it is not sufficient to permit an easy use of 2D arrays. To considerably reduce the elements number, the most promising technique is the sparse array described in the next section 2.4.2.d . The beam plot in Figure 2.15c-d, performed on the phantom of Figure 2.11c, confirms that the circular enclosed array has approximately the same beam profile as the dense array with fewer elements. The deactivation of the corner elements impacts weakly the array performances.

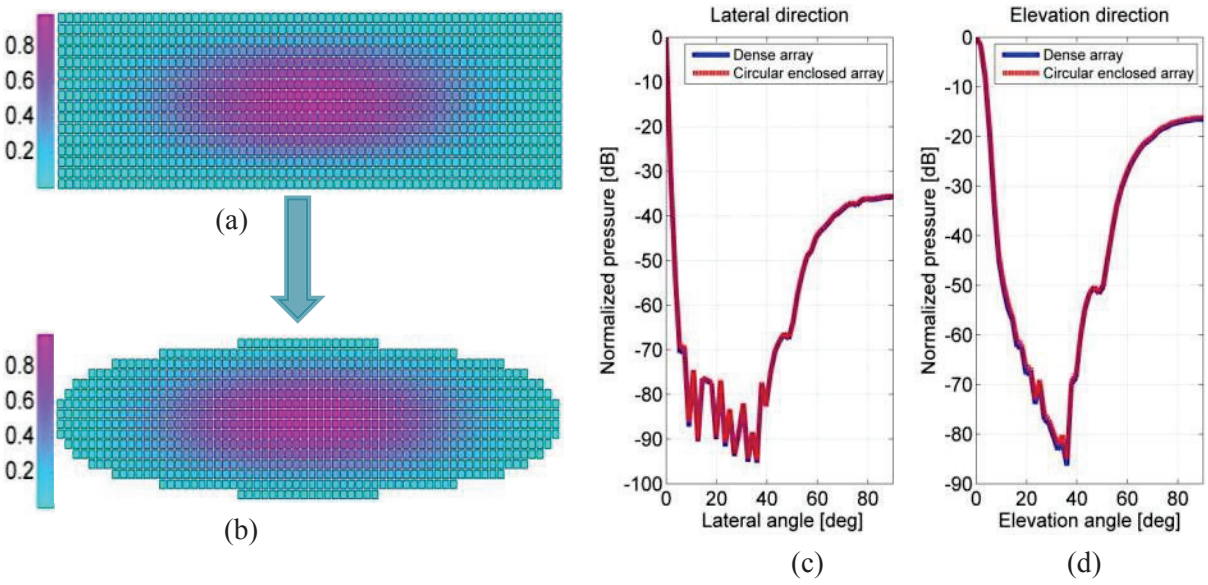

Figure 2.15 : (a) 2D dense array and (b) its corresponding circular enclosed array simulation with FIELD II. The colorbar represents the apodization coefficients varying from 0 to 1. Beam plots are compared in (c) lateral and (d) elevation directions with a focus point at 50 mm. The edge element deactivation does not significantly modify the array beam features but an decrease in the probe energy can be noticed in some cases.

2.4.2.d Sparse array

In computer science, a "sparse" matrix is a matrix which contains more zeros than non-zero values. It can also be understood as a matrix whose non-zero values are so rare that they form a scattered grid. Such a technique is ideal for element number reduction in a matrix array. The sparse array technique has been adapted to 2D ultrasound arrays as an element number reduction technique able to keep acceptable acoustical beam properties [Weber et al. (1999), Trucco (1999), Cardone et al. (2001)]. In the ultrasound domain, the technique is declined in two main types: the regular and the random sparse arrays. The regular sparse array consists in activating elements separated by regular distances all over the array whereas the random version breaks this regularity. The random disposition is more efficient than the regular one in terms of grating lobes reduction but the regular (periodic) disposition provides sharper main lobe than the random one [Brunke and Lockwood (1997)].

Sparse array is a very promising approach to overcome the beamformers limitations in terms of channel number but the selections of the best set of connected elements still need to be investigated. A study of Turnbull et al [Turnbull and Foster (1991)] showed that the sparse array can reduce the 2D arrays to less than one sixth (1/6) of their initial number without much deterioration of the image quality. This possibility provided by the sparse array is a

solution making possible the control of 2D arrays by the same beamformers as used in 1D array imaging. Sparse arrays do not have only good characteristics. Although it really simplifies the beamforming operation, it leads to an important energy loss, high sidelobes (random sparse array), and high grating lobes (regular sparse array). The sidelobes increase is linked to the discontinuity in the probe apodization whereas the inter-element distance greater than the mid-wavelength give rise to higher grating lobes[Turnbull and Foster (1991)]. Some simulation results of sparse array imaging by FIELD II have been published in [Austeng and Holm (2000), A. Austeng and Holm (2002), Andreas Austeng and Holm (2002)]. The efficiency of sparse array in 2D array elements number reduction is obvious but this reduced array does not provide the same image quality as the dense array. The beam profiles are simulated using the phantom of Figure 2.11c.

Periodic sparse array

The regular sparse arrays consist in connecting periodically a number of elements; the ratio between the initial 2D array pitch and the corresponding regular sparse arrays is noted p (p_x in the lateral direction and p_y in the elevation direction). In Figure 2.16a, both p_x and p_y are equal to 2 but they could be any multiple of the dense array's pitch [Brunke and Lockwood (1997), Bakary Diarra et al. (2012)]. Several periodic patterns can be used in the array conception comprising diagonal, circular, vertical and horizontal elements disposition [A. Austeng and Holm (2002)]. These techniques give an array which inter-element spacing (pitch) is larger than the mid-wavelength and consequently produce sharper main lobe and permits a powerful reduction of the necessary channel number. Figure 2.16b and d illustrate the first main drawbacks of the sparse array: the energy loss due to the active element reduction. This energy loss depends on the ratio of the active element in the array; for a reduction of about 68% the energy loss reaches – 23 dB (Figure 2.16b), about -13 dB for a 43% reduction (Figure 2.16d). The second drawback is highlighted by equation (2.12), the larger is the pitch, the higher and closer are the grating lobes [A. Austeng and Holm (2002)].

A concept permitting to correct the beam pattern of such arrays is the effective aperture. This concept consists in using different configurations in the transmission and the reception aperture in such a manner to suppress the grating lobes [Lockwood and Foster (1996), A. Austeng and Holm (2002), Bakary Diarra et al. (2012)]. This concept supposes that the final beam pattern is obtained by multiplying the transmitted beam function by the received one. In these conditions, the effective aperture represents the convolution between the transmit and receive aperture functions. Most of the time no element is common to both transmission and reception aperture but some exceptions exist. In any case the pitch of the receive and transmit aperture (array) should be different in order to efficiently reduce the grating lobes [Karaman et al. (2009)]. The grating lobes position in transmission correspond to the zeros position in reception and vice versa [Lockwood and Foster (1996), A. Austeng and Holm (2002)]. To illustrate this concept we simulate two examples shown in Figure 2.17.

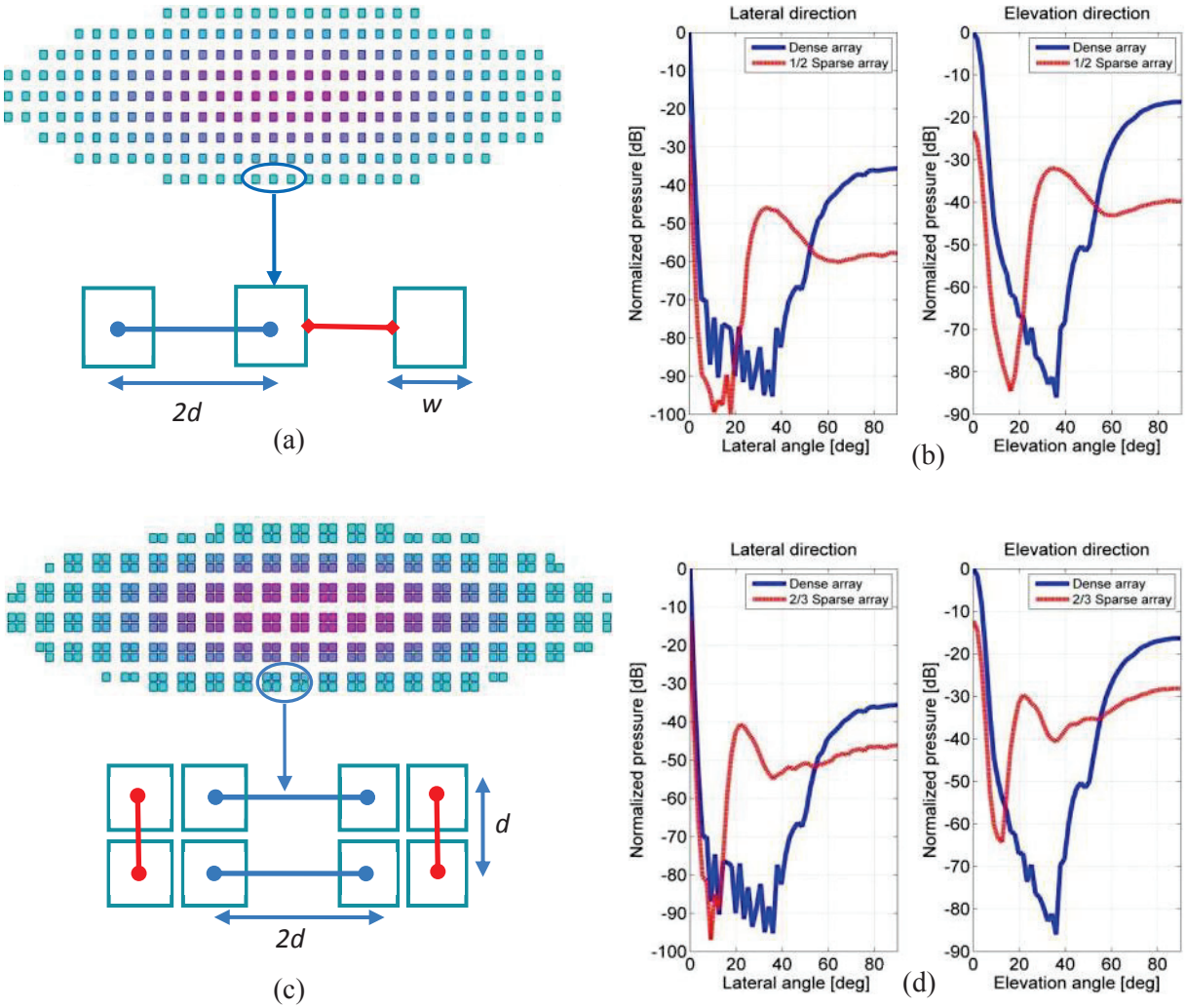

Figure 2.16 : different configurations of regular sparse arrays deriving from the 64x16 2D array considering its circular enclosed part (828 elements). In (a) the array is filled with 1/2 active elements (232 elements in total) and the beam profile compared to the dense array is displayed in (b). In (c) two elements are active out of 3 (2/3) (409 elements in total) and its beam profile compared to the dense array is displayed in (d). The energy loss is as important as the active elements reduction reaching – 23 dB in the 1/2 sparse array and – 13 dB in the 2/3 sparse array. This energy loss in a major drawback of all sparse array techniques and impedes their use more often.

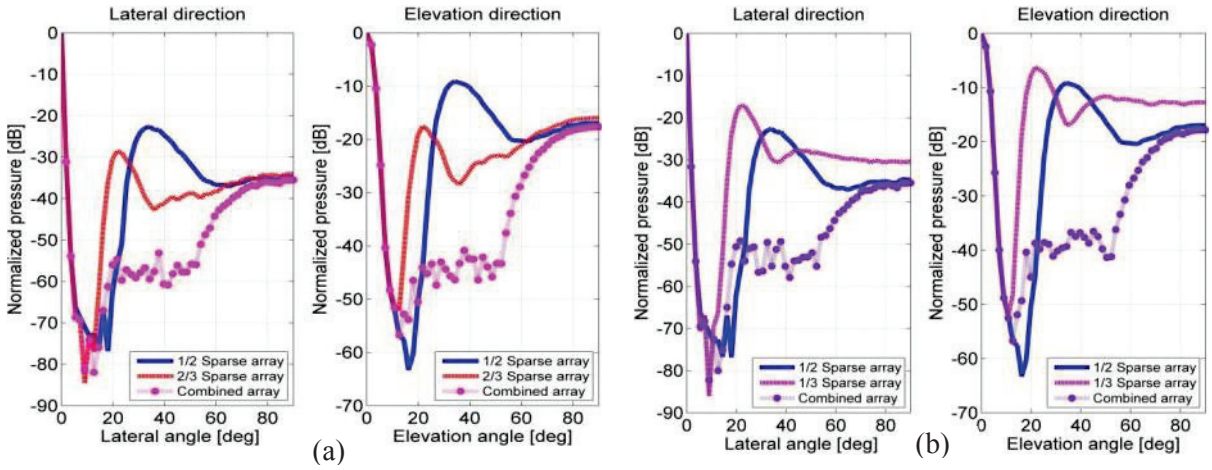

Figure 2.17 : the concept the effective aperture applied to the regular sparse array deriving from the 64x16 2D array. In (a) the beam profiles (lateral and elevation directions) correspond to: transmission and reception with the 1/2 sparse array (continuous line), transmission and reception with the 2/3 sparse array (dashed line) and transmission with the 1/2 sparse array and reception with the 2/3 sparse array (dotted line). In (b) the same simulations are performed replacing the 2/3 sparse array by an 1/3 sparse array (106 elements in total). The grating lobe reduction is significant in the neighborhood of the main lobe. The difficulty resides in the practical realization of different arrays in transmission and reception and the important energy loss.

In Figure 2.17a the 1/2-sparse array (Figure 2.16a) is used in transmission whereas the reception is done with the 2/3-sparse array of Figure 2.16c. If both the transmission and reception are made by the 1/2-sparse array the grating lobes level is - 22 dB and - 9 dB in lateral and elevation directions (continuous line) and – 29 dB and -18 dB in the 2/3-sparse array case (dashed line). Using the effective aperture concept, these grating lobes are reduced of 20 dB in both the lateral and elevation directions (dotted line). In Figure 2.17b, the 2/3-sparse array is replaced by a 1/3 sparse array (106 active elements), the grating lobes reduction is in the same order of magnitude as in Figure 2.17a, 20 dB. The limitations of this concept are the necessity of having different arrays in transmission and reception. The grating lobes seem to be moved away from the main lobe but not completely suppressed (Figure 2.17).

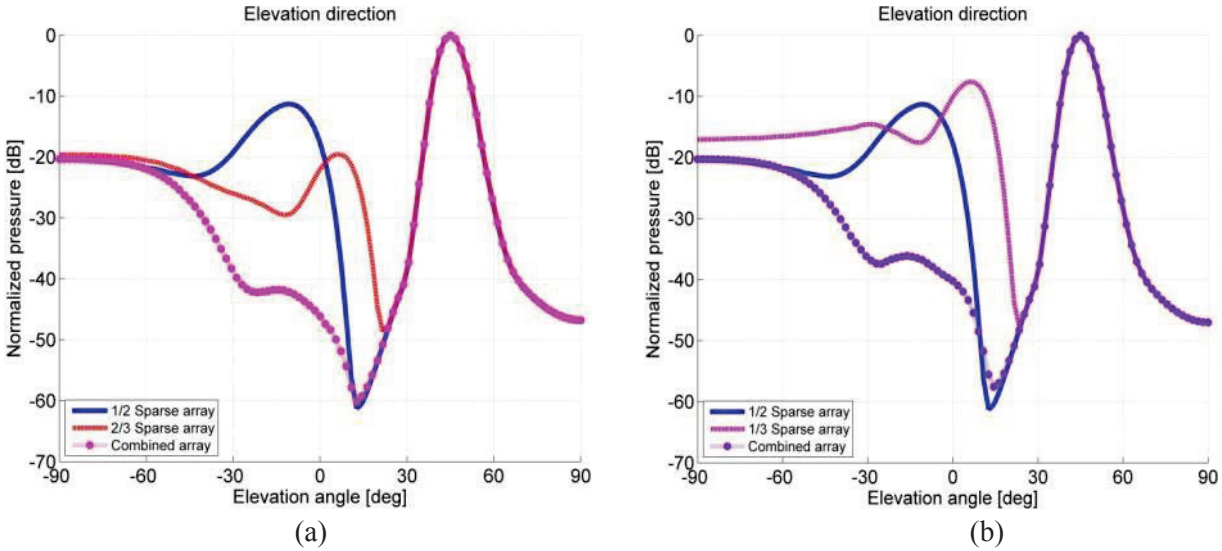

Figure 2.18: the concept the effective aperture when steering at (45°, 45°). In (a) beam profiles of the regular sparse array (deriving from the 64x16 2D array) filled with 1/2 element (continuous line), 2/3 elements (dashed line) and the result when transmitting with one configuration and receiving by the other (dotted line), (b) the same results when the 2/3 element sparse array is replaced by a 1/3 (109 elements) sparse array.

When the beam is steered on the side, its profile changes. The differences mainly concern the grating lobes position and thus their contribution to the resulting images [Lurton (2002)]. The ratio between the grating lobes level with and without using the effective aperture concept remains in the same order of magnitude as without steering, i.e. 20 dB (Figure 2.18a-b). The effective aperture allows a considerable reduction of the grating lobes in the neighborhood of the main lobe and imposes a smooth increase of the latter elsewhere.

Random sparse array on a regular grid

In the literature, the random sparse array means an array which active elements rows (or columns) are randomly selected from the dense array. Several examples deriving from the 64x16 2D array are presented to understand the impact of the active elements on the beam profile compared to the original dense array.

The beam profiles in Figure 2.19d compare the dense (fully sampled) array to the random sparse arrays. It can be noticed that a considerable energy loss occurs as the active elements number decreases like in the regular sparse array case presented in Figure 2.16. The energy reduction is about 21, 26 and 33 dB compared to the dense array when the active number is 256, 192 and 128, respectively. Contrary to the regular case another phenomenon (local maxima) can appear in the random sparse beam profiles between the main and the grating lobes: these are sidelobes. They appear at random positions from one sparse array configuration to another (even with the same number of active elements) in opposition to the grating lobes which remain at the same position. Figure 2.19d-e-f illustrate well the phenomenon.

For the 256-element sparse array, the most important sidelobe level is 35 dB in the lateral direction whereas it is 42 dB in the elevation direction. Figure 2.19e-f correspond to the beam profiles in the steering case when the scatterer is located at (45°, 45°) in both lateral and elevation directions.

As the beam characteristics can be quite different when the position of the activated element is random, one solution to ensure that the best possible configuration is reached is to use an optimization algorithm. As will be detailed later in the document optimization techniques can be used both to minimize the element number and the sidelobes level while keeping a pre-determined main lobe width.

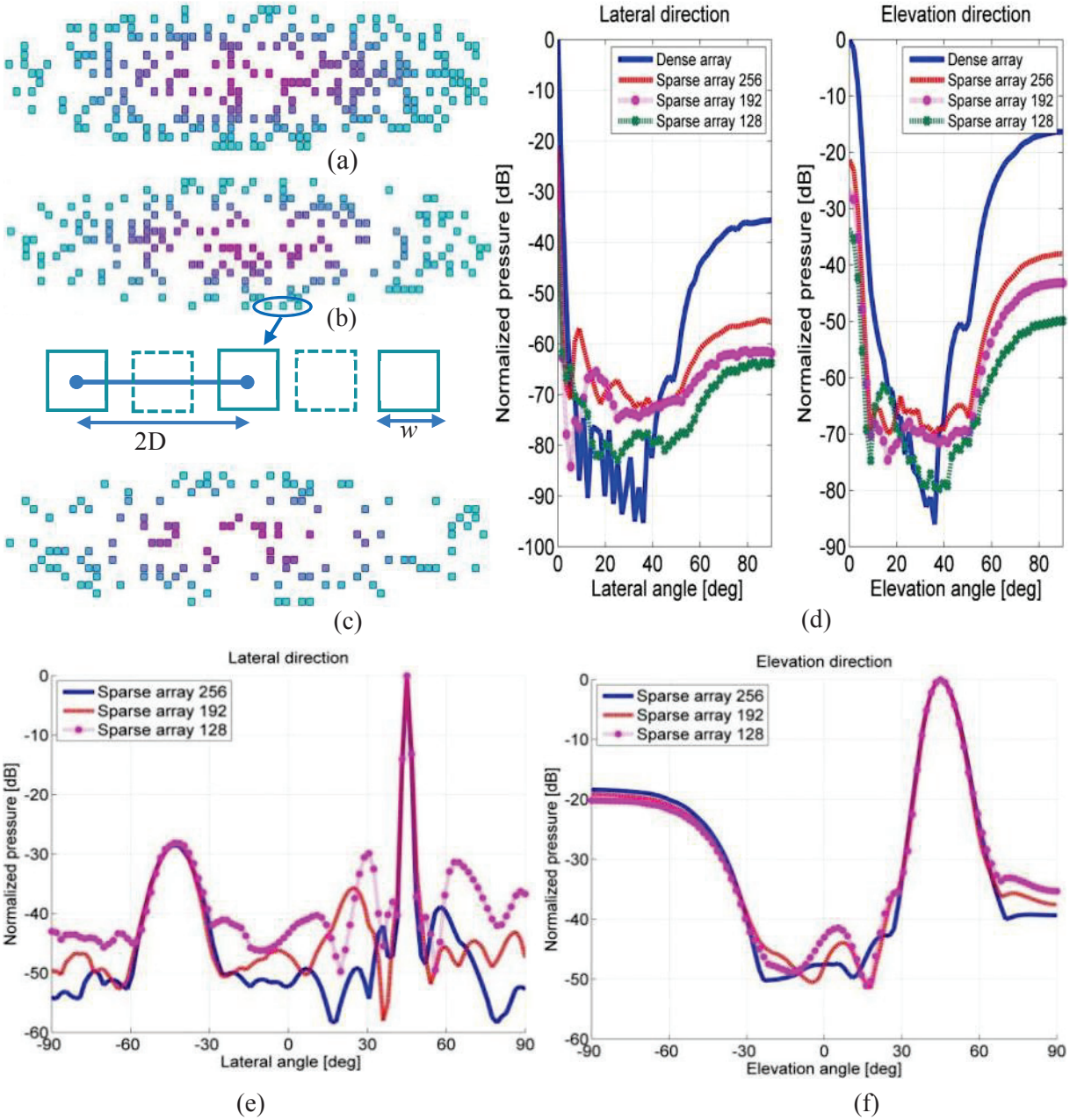

Figure 2.19 : random sparse arrays (deriving from the 64x16 2D array) with different active element number and their beam profiles normalized by that of the 64x16 dense array (a) 256 elements (dashed line) (b) 192 elements (dotted line) and (c) 128 elements (lozenge line) , (e) and (f) are the beam profiles when the scatterer is placed off axis at (45°, 45°) in lateral and elevation directions.

2.4.3. Prototypes presented in the literature

Most of the published studies on 2D arrays are theoretical or simulation studies because the realization of such probes is a real technological obstacle. The images are simulated on tissue mimicking phantoms. The inter-element distance in these probes equals (or is less than) the mid-wavelength in all these prototypes to limit the grating lobes. Some prototypes manufactured for experimental objectives in research laboratories are listed in Table 2.3. All the prototypes are fully controlled for the small ones or controlled by multiplexing circuits for the large ones to collect the signals.

Between all the prototypes, the most elaborated probe is that developed at Duke University which is driven in a configuration able to produce up to 47 volumes/second under some conditions [Light et al. (1997), Yen and Smith (2002)] with 256 elements. Each volume contains 64 sectorial images of 64 lines each one. This probe uses the row-column addressing beamforming technique to produce 16 lines at each transmission (16:1) in a sector of 65 degrees [Xie et al. (2005)]. In industry, [Savord and Solomon (2003)] proposed a 3000-elements array with beamforming modules in the handle to minimize the co-axes number. The array is divided into sub-arrays (3000/128 elements) and the ultrasound beam of each sub-array is funneled through the 128 channels in parallel. This parallelization avoids the use of too many channels and reduces the system complexity. This configuration permits to reach a great frame rate, 20 volumes per second [Daher and Yen (2006)].

Promising concepts to increase the volume rate in the real time volumetric imaging are proposed (22 volumes per second in [Canals et al. (1999)] or probably more [Taki and Sato (2007)]).

	Manufacturer	Central frequency	Elements number	Volume/second
2D arrays	Virginia University [Light et al. (1997), Girard et al. (2003), Fuller et al. (2003)]	3.3 MHz 3.5 MHz	32x32=256 40x40=3600	NC
	Thomson [A. Austeng and Holm (2002), Bureau et al. (1998)]	5 MHz	50x50=2500	NC
	Vermon [Nikolov and Jensen (2003)]	2.93 MHz	32x32=1024	NC
	GE Vingmed Ultrasound [Austeng and Holm (2000)]	3 MHz	50x50=2500	40 volumes/s
	Coastal Circuits [Eames et al. (2005)]	5 MHz	60x60=3600	NC
	Philips [Daher and Yen (2006)]	7 MHz	3000	20 volumes/s

Table 2.3: the prototypes of 2D arrays found in the literature, their different manufacturers and some imaging capabilities. It is difficult to obtain complete information about these arrays because most of the time no information is provided about the volume scanned the sector width, the scan depth and the volume size.

2.5. 2D array optimization algorithms

There are several algorithms for the random elements selection optimization and much of them are detailed with simulation results in [Holm et al. (2001)]. All these methods aim to reduce the sidelobes level while maintaining the main lobe width constant. The main methods are simulated annealing and genetic algorithms [Hopperstad and Holm (1999)].

2.5.1. Simulated annealing

The simulated annealing (SA) algorithm is a global optimization algorithm which permits to approximate the global optimum of multi-parameter functions. The optimization space can be either continuous or discrete. The name of the algorithm comes from the

annealing process consisting in heating and cooling a material to change its crystal dimensions and properties. It derived from the Metropolis algorithm [Gubernatis (2005)] which was used in substances crystallization process to superimpose a cooling profile to the materials. The key feature of SA is that it allows uphill moves (that is, moves that increase the value of the objective function) in order to escape local minima. Kirkpatrick adapted the method to informatics problem optimization like chip wiring process in electronics or travel salesman [Kirkpatrick et al. (1983)]. These problems are similar to the random choice of the piezoelectric elements in the sparse array and the SA can naturally be used to optimize this choice too.

In the 2D sparse array design, there are many possible positions (in lateral and elevation directions) for a given element as the selection is random. It will be interesting to find the most suitable position for each active element to minimize the beam pattern deterioration. This optimization depends on the elements' position, their apodization and the dense array beam profile. The application of SA to large 2D sparse-array design was first suggested by [Trucco (1999)] and recently refined by [Chen et al. (2010)]. The performance criteria of the algorithm are based on the sidelobes level, the active element number and the main lobe width. Several configurations of simulated annealing were applied to 2D array optimization with different sidelobes, element number reduction criteria and using single element weighting coefficients [Trucco (1999)], [Chen et al. (2010)]. [Murino et al. (1996)] minimize the sidelobes level when the aperture and the element number are kept fixed but most of the time the minimization concerns the element number when the beam pattern of the probe is fixed [Trucco and Repetto (1996), Holm et al. (1997)].

2.5.1.a Simulated annealing algorithm

Let f be a real-valued function to be minimized on a general but finite state space E. A SA algorithm with cost function f is a discrete time, non-homogeneous Markov chain $\left(\Gamma^{(n)}\right)_{n\geq 0}$ whose transitions are guided by a communication mechanism q and controlled by a cooling sequence $(T_n)_{n\geq 1}$. The communication mechanism gives the probabilities of the possible moves for generating a candidate solution from the current solution, and the cooling sequence decreases to zero. Formally, q is a map from E^2 to $[0,1]$ that has the following properties.

1. q is a Markov matrix: $\sum_{\eta\in E} q(\gamma,\eta) = 1$ for all $\gamma \in E$.
2. q is symmetric: $q(\gamma,\eta) = q(\eta,\gamma)$ for all $(\gamma,\eta) \in E^2$.
3. q is irreducible: for any $(\gamma,\eta) \in E^2$, there is a path $\gamma^{(1)},\dots,\gamma^{(K)}$ such that $\gamma^{(1)} = \gamma$, $\gamma^{(K)} = \eta$, and $q(\gamma^{(k)},\gamma^{(k+1)}) > 0$ for all $k \in \{1,\dots,K-1\}$.

(Property 2 means that the probability to propose a move from γ to η is the same as that to propose a move from η to γ, and property 3 means that any state can be reached from any other state in a finite number of moves.) The transitions of $\left(\Gamma^{(n)}\right)_n$ are given by

$$\mathrm{P}\left(\Gamma^{(n)} = \eta \mid \Gamma^{(n-1)} = \gamma\right) = P_{T_n}(\gamma,\eta), \tag{2.22}$$

where P_T is the Markov matrix on E defined by

$$P_T(\gamma,\eta) = \begin{cases} q(\gamma,\eta) & \text{if } f(\eta) \le f(\gamma) \text{ and } \eta \neq \gamma, \\ q(\gamma,\eta)\exp(-(f(\eta)-f(\gamma))/T) & \text{if } f(\eta) > f(\gamma). \end{cases} \quad (2.23)$$

Putting it simply, downhill moves are unconditionally accepted, whereas an uphill move from γ to η at iteration n is accepted with probability $\exp(-(f(\eta)-f(\gamma))/T_n)$. In practice, a finite-time realization $\left(\gamma^{(n)}\right)_{0\le n\le \mathcal{N}}$ of $\left(\Gamma^{(n)}\right)_n$ is generated as follows (Figure 2.20):

pick an initial state $\gamma^{(0)} \in E$;

for $n = 1$ to $\mathcal{N}$ **do**

draw a state η from the probability distribution $q(\gamma^{(n-1)}, .)$ on E;

set $\gamma^{(n)} \leftarrow \gamma^{(n-1)}$;

set $\Delta \leftarrow f(\eta) - f(\gamma^{(n-1)})$;

if $\Delta \le 0$ **then** set $\gamma^{(n)} \leftarrow \eta$;

else set $\gamma^{(n)} \leftarrow \eta$ with probability $\exp(-\Delta/T_n)$;

end (if)

end (for)

Figure 2.20: simulated annealing algorithm pseudo-code. The initialization main parameters are the temperature value, the temperature decrease coefficient and the sparsely filled 2D array steps

The robustness of SA is shown by the equation (2.23), even though the algorithm detects a local minimum, it doesn't get trapped because there is a probability of acceptance of a slight increase of the cost function during the SA running. This property permits to reach the global minimum of the cost function which is returned when the optimization conditions are satisfied.

2.5.1.b Main convergence results

As the temperature T_n goes to zero, the distribution of $\Gamma^{(n)}$ concentrates on the global minima of f, and SA does indeed converge to a global minimum if $T_n \propto 1/\ln(n+1)$ [Hajek (1988)]. However, logarithmic cooling yields extremely slow convergence, and most successful applications of SA use exponential schedules. The theoretical justification of exponential cooling is given in [Catoni (1992)], where it is shown that the convergence speed exponent of SA has an upper limit α_{opt} and that it is possible to construct a family $\{(T_n)_{1\le n\le \mathcal{N}}; \mathcal{N} \ge 1\}$ of finite cooling sequences of the form

$$T_n = T_0 \exp(-\zeta n), \quad (2.24)$$

where $\zeta \in (0, +\infty)$ depends on $\mathcal{N}$(the maximum number of iterations), such that

$$\ln\left(\mathrm{P}\left(f\left(\Gamma^{(\mathcal{N})}\right) > \inf_{\gamma\in E} f(\gamma)\right)\right) \sim \ln(\mathcal{N}^{-\alpha_{opt}}). \tag{2.25}$$

These results are not well-known, and yet they constitute the most significant advance in SA theory beyond the asymptotic properties established in [Hajek (1988)]. They imply in particular that for any $\alpha \in (0, \alpha_{\mathrm{opt}})$, there is a family $\{(T_n)_{1\le n\le \mathcal{N}}; \mathcal{N} \ge 1\}$ of finite exponential cooling sequences such that

$$\mathrm{P}\left(f\left(\Gamma^{(\mathcal{N})}\right) > \inf_{\gamma\in E} f(\gamma)\right) \sim \mathcal{N}^{-\alpha} \tag{2.26}$$

for $\mathcal{N}$ large enough. In other words, exponential cooling makes it possible for SA to have a convergence speed exponent arbitrarily close to the best achievable exponent over all possible cooling sequences. More elaborate developments in SA theory can be found in [Robini and Reissman (2013)] and [Robini (2013)].

2.5.1.c Cost function

The optimization procedure with the SA is made with a cost function which contains all the terms to be optimized. The element number and the sidelobes level are the main variables to be optimized. A general notation of this function was given first in the domain of 3D underwater imaging by [Trucco (1999)] and there exist a slight modified version of this technique published by [Chen et al. (2010)]. This function uses the pressure formulation established for the far field beam pattern given by [Nielsen (1991)]

$$p(u,v) = \left|\sum_{i=1}^{\mathcal{M}} w_i \,.\, e^{-j\frac{2\pi}{\lambda}(x_i\,.u\,+\,y_i\,.v)}\right| \tag{2.27}$$

$$u = \cos(\varphi)\sin(\theta)$$

$$v = \sin(\varphi)\sin(\theta)$$

w_i Coefficient of the i^{th} element

x_i , y_i coordinates of the i^{th} element

u, v Beam direction vectors

This beam pattern function is used to fix the sidelobes in the desired area outside the main lobe zone. Other terms are necessary to take into account the element number and eventually the range of the coefficients.

The global final function was expressed by [Trucco (1999)] as follows

$$f(V,W,\mathcal{M}) = \left[k_1 \iint_{(u,v)\in U} \left(\frac{p(u,v)}{P_M} - p_s(u,v)\right) dudv + k_2\mathcal{M}\right]^2 \tag{2.28}$$

The formulation given by [Chen et al. (2010)] is slightly different from the former.

$$f(W,\mathcal{M}) = k_1\left[\sum_{(u,v)\in U}\left(\frac{p(u,v)}{P_M} - p_s(u,v)\right)\right]^2 + k_2\mathcal{M}^2 + k_3(R_0 - Rd)^2 \qquad (2.29)$$

P_M Maximum of pressure

p_s Desired sidelobes level to be obtained

U The area excluding the main lobe, the set of (u,v) values satisfying the relation $p(u,v)/P_M > p_s(u,v)$

R_0 , R_d Respectively the obtained and desired ratio between the w_i maximum and minimum

$\mathcal{M} = M\text{x}N$ Active elements' number

The third term in the equation (2.29) is not necessary as the variation of the coefficients can be set up directly in the optimization algorithm without making more complex the cost function. The area (U) is the whole space excluding the main lobe width at – 6 dB in both the lateral and elevation directions. A study of the SA was applied to wide-band linear arrays too by [Cardone et al. (2001)] and by [Trucco (2002)] with good optimization results.

Other studies based on the SA algorithm for array optimization are presented without more details on the optimization process [Hopperstad and Holm (1999), Behar and Nikolov (2007)]. There isn't any precise manner to determine the values of the coefficients $k1$, $k2$ and $k3$ used in the optimization process. The value of each coefficient indicates the importance of its corresponding term in the cost function. It would be interesting if there was a technique to determine optimal values of these parameters depending on the applications.

2.5.1.d Algorithm steps for 2D array

The basic principles of the SA are maintained when applied to the 2D optimization completed by some additional steps. These steps include the random selection of the elements and their death and resurrection probabilities. The algorithm begins with the initial value of the temperature and the 2D array filled sparsely. An element is randomly selected; in [Chen et al. (2010)] version if this element is active it is simply turned off but if it is inactive it is resurrected with a certain probability. In Trucco's version [Trucco (1999)] both the element resurrection and the death are managed by a probability value. After each modification of an element state (coefficient), the cost function is re-evaluated to know whether its value decreases in which case the modification is maintained otherwise the old state of the element is restored based on a probability function that depends on the current temperature. At each complete exploration of the 2D array, the active element number is updated and compared to its previous value to know if it decreases. The satisfaction of the optimization criteria or the reach of the maximum iteration terminates the optimization procedure. For large probes, the computation takes much time. A flow chart detailing the different steps of the algorithm is shown in Figure 2.21.

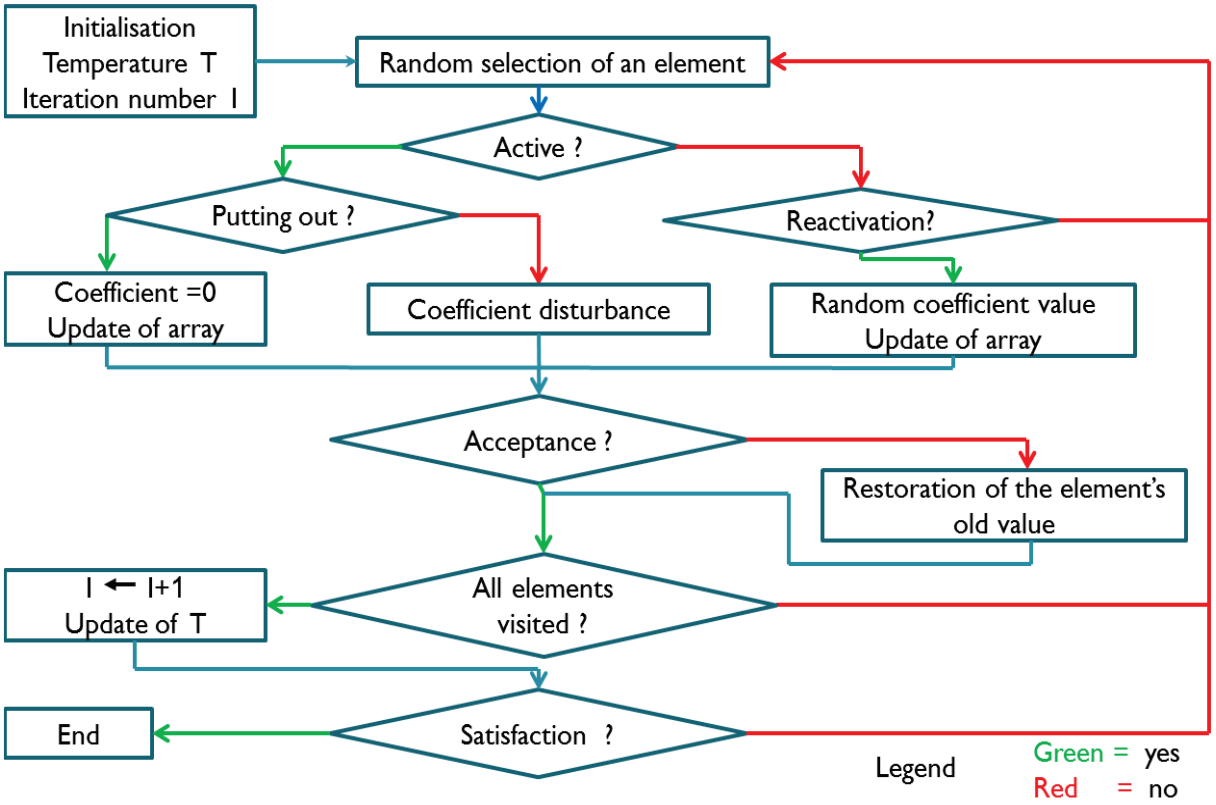

Figure 2.21 : flow chart of the simulated annealing algorithm applied to the thinning of the 2D arrays [Trucco (1999), Chen et al. (2010)].

2.5.2. Genetic algorithms

Genetic algorithms are used to find a set of parameters that optimizes the output of an objective function. As the simulated annealing, they are suitable for the optimization of non-linear problems that do not admit any exact solution such as the thinning of the arrays [Haupt (1994)]. The random choice of the elements in sparse arrays can also be optimized using genetic algorithms. The expected outputs are identical to those of the SA namely the element number and the sidelobes minimization. The main difference between the two algorithms is linked to the 2D array dimension. Genetic algorithms are suitable for small 2D arrays optimization but not efficient for large scale 2D arrays compared to the simulated annealing [Chen et al. (2010)]. Some optimization studies on medium 2D arrays with these algorithms are reported [Haupt (1994), Lommi et al. (2002), Caorsi et al. (2002), Yang et al. (2006)].

2.5.2.a Cost function

Many different cost functions (known as the fitness) are proposed in the literature for 2D array thinning using the genetic algorithms. The first one proposed by [Haupt (1994)] is suitable for both the 1D and 2D arrays optimization. The same notation is adopted by [Zhang et al. (2012)] and a slightly different version by [Kesong et al. (2007)]

$$f(W,u,v) = \sum_{m=1}^{M}\sum_{n=1}^{N} w_{mn}\cos[\pi(2m-1)d_x u]\,.\cos\left[\pi(2n-1)d_y v\right] \qquad (2.30)$$

where $u = sin\theta cos\varphi$ and $v = sin\theta sin\varphi$ are the direction vectors, d_x and d_y are respectively the inter-element distance in lateral and elevation directions ($pitch = \lambda/2$ generally) and W is the coefficient matrix of the array. Contrary to the simulated annealing, most of genetic algorithms array thinning are based on the binary state of the array elements, the coefficient (w_{mn} in equation (2.30)) are 1 for active elements and 0 for inactive ones. Another approach consisting in minimizing the error between the dense array beam and the sparse array was used [Weber et al. (1994), Weber et al. (1999)]. In the 1D array case, genetic algorithms gives interesting results mainly when combined with MRL (minimum redundancy linear-array) [Yang et al. (2006)].

2.5.2.b Algorithm steps

The genetic algorithms differ from the SA algorithm because they don't use the parameters (element coefficients) themselves but a coded value of the latter. In the first step each coefficient is coded using the binary coding (most of the time) because of its simplicity. The fitness value of the element coefficients permit to establish a probability table used in the next steps. The main drawback of the algorithms is their complexity if there are a lot of parameters in the problem to solve. A simple flow chart of the algorithm is represented in Figure 2.22.

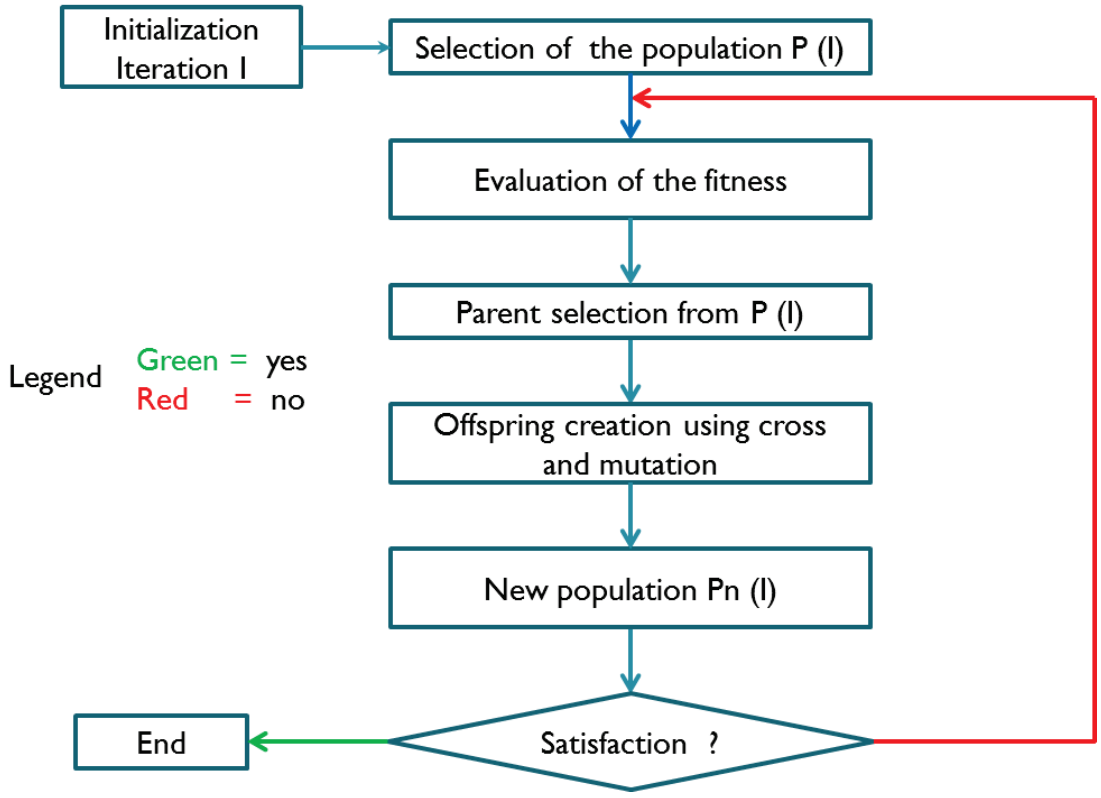

Figure 2.22: flow chart of the genetic algorithm applied to the thinning of 2D array

2.6. Conclusion

Important advances have been made in 3D ultrasound imaging but obstacles remain in the use of the 2D arrays. The mathematical background of the 2D array permits to identify the

points to be improved to achieve acceptable and fast imaging with these arrays. The combination of the simulated annealing and the reduction techniques give encouraging way towards real time 3D imaging.

In the next chapter, our contributions to overcome the limitations inherent to the dense arrays are presented. An improved version of the simulated annealing algorithm and new element positioning strategies are developed. The performances between the proposed methods and those available in the literature are compared in terms of beam energy, image contrast and element reduction capabilities.

Chapter 3

New positioning strategies in 2D arrays

3.1. Introduction

From the bibliography investigation, we have identified the current advances in 2D array imaging and also noticed the obstacles encountered in this domain regarding both physical and technological aspects. The physical limitations concern mainly the spatial sampling conditions which impose very small element to reduce the grating lobes at the expense of the probe sensitivity (signal-to-noise ratio) and the great number of channels needed to drive them. The technological challenges concern the connection of thousands of elements on recent beamformers. For this purpose complex multiplexing systems are implemented lowering more the array performances.

Our contribution presented in this chapter can be divided into two main parts:

1. The first point concerns an improvement the mathematical aspects of the problem and proposes a more rigorous formulation
2. The second point concerns the proposition of new degrees of freedom to improve the beam characteristics. Here we propose to use different element positioning strategies and elements with variable sizes.

A comparison between the new elements positioning strategies, called non-grid (sparse) array and variable size (non-grid) array, and the standard sparse array without and with optimization are presented in this chapter. All simulations results are performed using the Field II program and the reference array is the 64x16 array designed in Section 2.4.1.c . Furthermore, a square 64x64 2D array is studied to validate the new strategies in a larger and more general-purpose array.

3.2. Optimization cost function

The cost function is the most important part of the optimization process. It contains the different terms that fix the expected specifications of the beam profile. The optimization procedure becomes necessary because of the inconstancy of the beam profile of the sparse arrays from a random filling to another, even with the same number of elements. Alternatives proposed in the literature to constraint the probe beam to a desired value depending on the application has been investigated since years and presented previously. These optimizations (often known as thinning) are limited to the ultrasound 2D array design but they are used in many fields as the electromagnetic antennas optimization in telecommunications.

The optimization process can be represented by the simplified chart of Figure 3.1. The input parameters are the initial sparse array and the expected beam properties whereas the outputs are the optimized array containing the number of active elements and the cost energy function. The optimization is also possible with a fixed number of active elements to find the suitable coefficients to fit well a given application. The latter method may not guaranty the

fulfillment of all the beam criteria unless the active element number is high enough to fit them. The initialization step is important and is realized as follows:

- Make a quick simulation of the beam profile of the dense array to determine the average value of the main lobe width at - 6 dB and use that value to define the optimization zone U
- Approximate by making some simulations with the sparse array to know approximately the number of elements which fills the sidelobes constraints expected and use the same range of element number at the algorithm beginning. This second point is useful but not necessary. It is just a mean to considerably reduce the algorithm convergence time.

The algorithm principal stop condition is the maximum number of iterations fixed preliminarily.

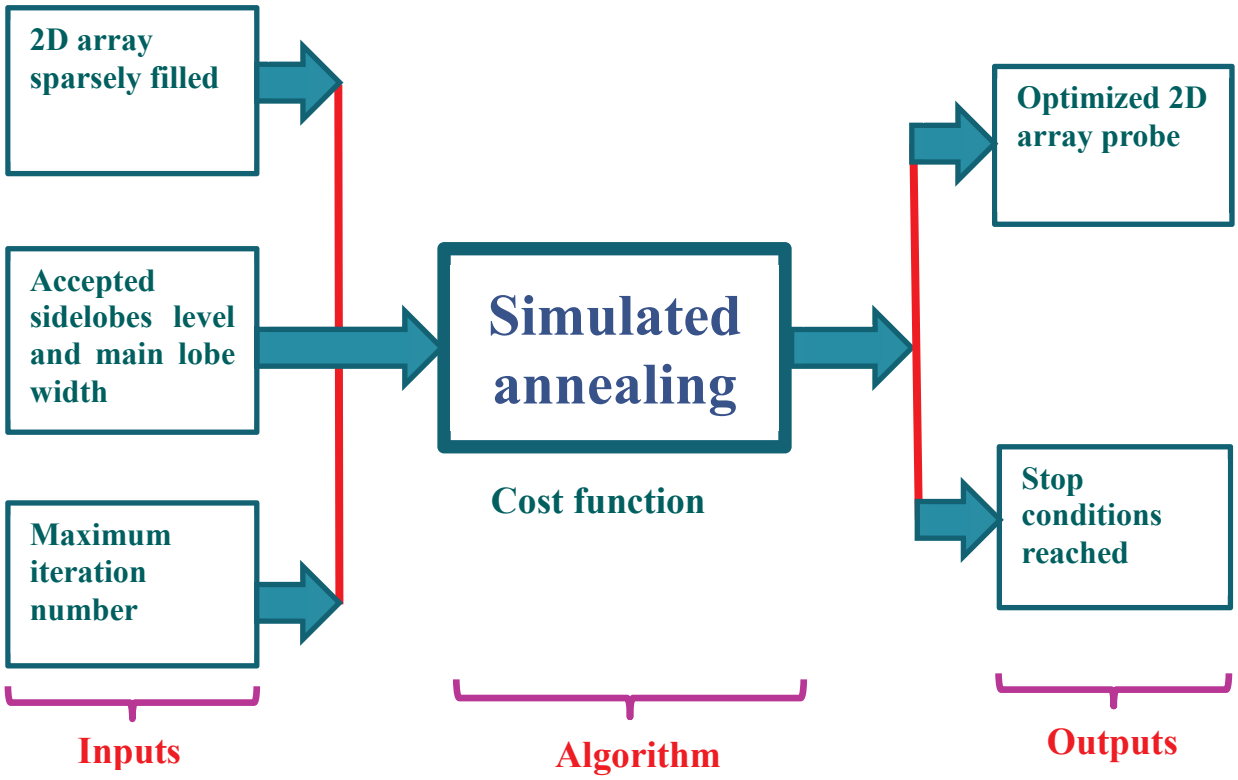

Figure 3.1: bloc diagram of the complete optimization scheme applied to the 2D sparse arrays. The inputs of the algorithm are the sparse array, the desired beam characteristics such as the sidelobes level, the main lobe width. The outputs are the optimized array.

3.2.1. Cost function reformulation

A general cost function including the parameters of our optimization problem—namely, the set of active elements and the maximum side-lobe level—was proposed by [Trucco (1999)] (see also [Trucco et al. (2008)]) and refined in [Chen et al. (2010)]. We start with a modified description of this function which serves as a basis for discussing our choice.

Assume that each possible element position is indexed by an integer $m \in \{1, \dots, \mathcal{M}\}$, where $\mathcal{M}$ is the total number of positions. Then, any sparse-array configuration can be represented by a set $A \subset \{1, \dots, \mathcal{M}\}$ defining the active elements and by a vector $\gamma \in [\gamma_{\min}, \gamma_{\max}]^{|A|}$ containing the weighting coefficients of these elements. More precisely, for

any $i \in \{1, \dots, |A|\}$, the i-th entry γ_i of γ is the weighting coefficient of the active element $\sigma_A(i)$, where σ_A is the bijection from $\{1, \dots, |A|\}$ to A such that $\sigma_A(1) < \cdots < \sigma_A(|A|)$. Using this representation, the set S of all possible sparse-array configurations is given by

$$S = \{(A, \gamma) : A \subset \{1, \dots, \mathcal{M}\} \text{ and } \gamma \in [\gamma_{\min}, \gamma_{\max}]^{|A|}\}. \tag{3.1}$$

Let $p(A, \gamma)$ be the normalized far-field beam pattern [Nielsen (1991)] of the array (A, γ), that is,

$$p_{(A,\gamma)}(u, v) = \frac{1}{\|\gamma\|_1} \left| \sum_{i=1}^{|A|} \gamma_i \exp\left(\frac{2j\pi}{\lambda} \left(x_{\sigma_A(i)} u + y_{\sigma_A(i)} v \right) \right) \right|, \tag{3.2}$$

where $u, v \in [-2, 2]$ are the first two coordinates of the difference between the unit arrival and steering directions, $\|\gamma\|_1 = \sum_{i=1}^{|A|} |\gamma_i|$ is the l_1-norm of γ, and (x_m, y_m) denotes the position of the mth element on the surface of the probe. The optimization problem considered in [Trucco (1999)] is equivalent to that of minimizing the function $f_{\mathrm{T}} : S \to \mathbb{R}$ defined by

$$f_{\mathrm{T}}(A, \gamma) = \mu |A| + \iint_U \left(p_{(A,\gamma)}(u, v) - p_{\mathrm{s}} \right)^+ \mathrm{d}u \, \mathrm{d}v \,, \tag{3.3}$$

where $\mu > 0$ controls the strength of the sparsity constraint, p_s is the maximum sidelobe authorized outside the main-lobe region, t^+ stands for the positive part of t (that is, $t^+ = \max(\{t, 0\})$), and U is the set of coordinate pairs (u, v) outside the main-lobe region.

To define our cost function, we first simplify the manipulation of the array configurations by representing them by vectors in a subset E of the closed rectangle $[0, \gamma_{\max}]^{\mathcal{M}}$. Then, the mth element of an array γ is active if $\gamma_m > 0$, and the sparsity promoting functional used in (3.3) is the l_0-norm $\|.\|_0 : \gamma \in E \to |\{m : \gamma_m \neq 0\}|$. We propose to further reduce the complexity of the optimization problem by replacing the l_0-norm by the l_1-norm $\|.\|_1 : \gamma \in E \to \sum_{m=1}^{\mathcal{M}} |\gamma_m|$, which, unlike the l_0-norm, is continuous and convex (the use of the l_1-norm as a sparsity-promoting functional is reviewed in [Candès et al. (2008)] and [Daubechies et al. (2010)]). The solutions to our optimization problem are thus the global minima of the cost function $f : E \to \mathbb{R}$ defined by

$$f(\gamma) = \mu \|\gamma\|_1 + \left(\iint_U \left(p_{(A,\gamma)}(u, v) - p_{\mathrm{s}} \right)^+ \mathrm{d}u \, \mathrm{d}v \right)^2 \tag{3.4}$$

(taking the square of the integral rather than the integral itself is merely a matter of choice), where the beam pattern p_γ is given by

$$p_\gamma(u, v) = \frac{1}{\|\gamma\|_1} \left| \sum_{m=1}^{\mathcal{M}} \gamma_m \exp\left(\frac{2j\pi}{\lambda} (x_m u + y_m v) \right) \right|. \tag{3.5}$$

Minimizing f over E is significantly easier than minimizing f_{T} over S, but it remains a difficult optimization problem, which is the reason why we also use SA. It is important to realize that the computed solutions are not sparse in the strict sense that their entries are mostly zeros; they are sparse in the weak sense that a great proportion of their entries are very close to zero. Consequently, the final solution is obtained by applying a hard-threshold to the entries of the output of the minimization process. Denoting this output by $\hat{\gamma}$, the weighting coefficients ${\gamma_1}^*, \ldots, {\gamma_{\mathcal{M}}}^*$ of the optimized sparse array are given by

$$\gamma_m^* = \begin{cases} \hat{\gamma}_m & \text{if } \hat{\gamma}_m \geq \beta\,, \\ 0 & \text{if } \hat{\gamma}_m < \beta\,, \end{cases} \tag{3.6}$$

where β is a predefined threshold.

3.2.2. Optimization strategy

Designing an efficient SA algorithm means smartly choosing the communication mechanism q and carefully selecting the cooling sequence $(T_n)_{n\geq 1}$. In this section, we describe our communication strategy and the associated SA algorithm. The tuning of the cooling sequence is discussed in Section 3.2.3.

First of all, to satisfy the finite-state space assumption of the SA theory outlined in Section 2.5.1.b , we let the domain of f be the discrete set

$$E = \Lambda^{\mathcal{M}}, \qquad \Lambda = \left\{ \frac{l\gamma_{\max}}{L} : l \in \{0, \ldots, L\} \right\}, \tag{3.7}$$

where the positive integer L can be arbitrarily large. That said, we use a communication mechanism that generates candidate solutions that differ from the current states by at most one element, as in [Trucco (1999)] and [Chen et al. (2010)]. However, since the representation of the sparse-array configurations as elements of E (3.7) is simpler than the representation in S (3.1), our single-element updating dynamics is simpler than those proposed in [Trucco (1999)] and [Chen et al. (2010)]. Indeed, we generate a candidate solution $\eta = (\eta_1, \ldots, \eta_{\mathcal{M}})$ from a configuration $\gamma = (\gamma_1, \ldots, \gamma_{\mathcal{M}})$ by picking an element index $k \in \{1, \ldots, \mathcal{M}\}$ and a weighting coefficient $c \in \Lambda$ uniformly at random and setting $\eta_k = c$ and $\eta_m = \gamma_m$ for all $m \neq k$. Formally, the associated communication matrix has a quite simple expression: for any $(\gamma, \eta) \in E^2$,

$$q(\gamma, \eta) = \begin{cases} 1/\big(\mathcal{M}(L+1)\big) & \text{if } \exists!\, k \in \{1, \ldots, \mathcal{M}\},\ \eta_k \neq \gamma_k, \\ 1/(L+1) & \text{if } \eta = \gamma, \\ 0 & \text{otherwise}\,. \end{cases} \tag{3.8}$$

This Markov chain is clearly symmetric and irreducible, which are the two requirements on the communication mechanism for the convergence of SA.

The exponential cooling sequence (2.24) can be written under the form

$$T_n = T_{\max}\left(\frac{T_{\min}}{T_{\max}}\right)^{\frac{n-1}{\mathcal{N}-1}}, \tag{3.9}$$

where $T_{\max}$ and $T_{\min}$ denote the initial and final temperatures, respectively, and $\mathcal{N}$ is the total number of iterations. Given these parameters, and letting ε^k be the k-th vector of the standard basis of $\mathbb{R}^{\mathcal{M}}$, the pseudo-code of our SA algorithm for sparse-array optimization is presented in Figure 3.2:

pick an initial array configuration $\gamma^{(0)} \in E$;
  set $\xi \leftarrow \ln(T_{\min}/T_{\max})/(\mathcal{N}-1)$;
  for $n = 1$ **to** $\mathcal{N}$ **do**
    draw $k \in \{1, \ldots, M\}$ and $c \in \Lambda$ uniformly at random;
    set $\eta \leftarrow \gamma^{(n-1)} + (c - \gamma_k^{(n-1)})\varepsilon^k$;
    set $\Delta \leftarrow f(\eta) - f(\gamma^{(n-1)})$;
    if $\Delta \leq 0$ **then** set $\gamma^{(n)} \leftarrow \eta$;
    else
      set $T \leftarrow T_{\max}\exp((n-1)\xi)$;
      draw $a \in [0,1]$ uniformly at random;
      if $a \leq \exp(-\Delta/T)$ **then** set $\gamma^{(n)} \leftarrow \eta$;
      else set $\gamma^{(n)} \leftarrow \gamma^{(n-1)}$;
      end (if)
    end(if)
  end (for)

Figure 3.2: the pseudo-code of the modified simulated annealing algorithm. The 2D array is put in one vector and the algorithm running is speed up by computing only the cost function modification due to the disturbance of an element state

3.2.3. Cooling schedule

The performance of a SA algorithm is strongly influenced by the tuning of its cooling sequence. Making a dichotomy between the asymptotic and finite-time convergence theories, one can use either logarithmic or exponential cooling. For instance, [Trucco (1999)] uses logarithmic sequences of the form

$$T_n = \frac{T_{\max}\ln(2)}{\ln(\kappa\mathcal{M}\lfloor n/\mathcal{M}\rfloor + 2)}, \tag{3.10}$$

where $\kappa > 1$, and $\lfloor . \rfloor$ is the floor function, whereas [Chen et al. (2010)] use exponential sequences of the form

$$T_n = T_{\max} \tau^{\lfloor n/\mathcal{M} \rfloor} \tag{3.11}$$

with $\tau = 0.85$. In both cases, the temperature is updated after each sweep (that is, after each cycle through all the elements), and the initial temperature $T_{\max}$ is chosen empirically so that most transitions are accepted at the beginning of the annealing process. The final temperature can be fixed in advance by setting the number of sweeps, as in [Trucco (1999)], or it can be set adaptively via a termination criterion, as in [Chen et al. (2010)], where it is proposed to stop the algorithm when the number of active elements does not decrease over a given number of sweeps.

Contrary to [Trucco (1999)], we suggest to use exponential cooling, which is more robust than logarithmic cooling in the finite-time case [Catoni (1992)], and unlike [Chen et al. (2010)], we prefer to fix the horizon N of the algorithm so as to keep control over the running time. This leaves us with the problem of finding appropriate values for the initial and final temperatures, which has been extensively addressed in the early ages of SA (see, e.g., [Laarhoven and Aarts (1987)]). From our experience, we suggest to select $T_{\max}$ and $T_{\min}$ so that the uphill acceptance rates (that is, the ratios of the number of accepted uphill moves to the number of proposed ones) at the beginning and at the end of the optimization process are close to some given values $\chi_{\max}$ and $\chi_{\min}$ such as $0 < \chi_{\min} \ll \chi_{\max} < 1$. Accurate methods to perform these estimations are given in [Robini et al. (1999)], but they are time-consuming. In fact, as long as the horizon N is large enough, correct orders of magnitude are satisfactory, and thus fast appropriate estimation methods do the job.

We propose a simple and efficient procedure based on the homogeneous Markov chain $(\Gamma^{(n)})_n$ with transition probabilities

$$\mathrm{P}\left(\Gamma^{(n)} = \eta \,\middle|\, \Gamma^{(n-1)} = \gamma\right) = q(\gamma, \eta)\,, \tag{3.12}$$

where q is the communication matrix defined in (3.8). Given a positive integer K, we generate a finite-time realization of $(\Gamma^{(n)})_n$ with K uphill moves, and we set $T_{\max}$ and $T_{\min}$ to be the temperature values such that the average acceptance probabilities over these uphill moves are equal to $\chi_{\max}$ and $\chi_{\min}$, respectively. More formally, we simulate $(\Gamma^{(n)})_n$ until we obtain K pairs $(\gamma^{(n_k)}, \gamma^{(n_k+1)})$ of successive states such that $f\left(\gamma^{(n_k)}\right) < f\left(\gamma^{(n_k+1)}\right)$, and we let $T_{\max}$ and $T_{\min}$ be the solutions of

$$\frac{1}{K} \sum_{k=1}^{K} \exp\left(-\left(f\left(\gamma^{(n_k+1)}\right) - f\left(\gamma^{(n_k)}\right)\right)/T\right) = \chi \tag{3.13}$$

for $\chi = \chi_{\max}$ and $\chi = \chi_{\min}$. The left-hand side of (3.13) increases with increasing temperature, and thus, for any $\chi \in (0\,, 1)$, this equation has a unique solution which can be determined by any standard root-finding method. In practice, effective cooling sequences are obtained by taking $\chi_{\max} \in [0.6, 0.9]$, $\chi_{\min} \in [10^{-4}, 10^{-3}]$, and K of the order of 10 to 100 times the number $\mathcal{M}$ of possible element positions.

3.3. Non-grid based array

In this section, the principle of the non-grid array is explained going from the standard regular grid element disposition. The beam characteristics (PSF, beam profiles of the standard and the non-grid sparse arrays are simulated and compared when both of them are filled with the same number of active element. The main purpose of these comparisons in to illustrate the beam pattern improvement capabilities in terms of the grating lobes reduction and the main lobe thinning provided by the proposed non-grid technique. A hanning apodization is applied to both arrays.

3.3.1. Method description

The non-grid based array is a new element placement strategy aimed to overcome the limitations of the regular grid-based methods used in the standard 2D arrays [B. Diarra, Liebgott, Cachard et al. (2012)]. This technique removes the periodicity in the element placement.

The non-grid array maintains all the characteristics of the main lobe of the beam and contributes to suppress its unwanted parts, i.e the grating lobes. In the standard regular grid placement, the grating lobes come from the periodicity in the element disposition and the relation between the inter-element distance and the wavelength (spatial sampling). The effect of the grating lobes is not noticeable in linear scanning but in sectorial scanning, depending on the sector width, the contribution of the grating lobes can be as important as the main lobe. In that case, the resulting image contains artifacts (fake echoes) which make difficult or even impossible its interpretation. Currently, a solution to reduce the grating lobes is to use small elements but this choice leads to a poor resolution and, unless a huge number of elements is used, a decrease of the probe sensitivity as its active surface is too small. The non-grid based (sparse) array is an efficient alternative for the 2D arrays beam pattern improvement. Placing the array elements independently from any rows and columns considerations presents several advantages; it permits to sharply decrease the grating lobes, and allows overstepping the spatial sampling condition which classically limits the element size in the 2D arrays. Figure 3.3 describes the principle of the non-grid sparse array.

[Jian-Yu Lu and Greenleaf (1994)] stated that a random element placement is expected to give a better result in terms of grating lobes reduction than the other techniques studied until now but they pointed out the difficulty of the conception of such a 2D array. The new technology based on the CMUT (Capacitive Micromachined Ultrasonic Transducer) elements is a suitable solution to make probes based on the non-grid approach [Bavaro et al. (2008)]. Information collected from ultrasound probe manufacturers confirms the feasibility of such an array even with the piezoelectric elements under some geometrical constraints such as element size and the kerf.

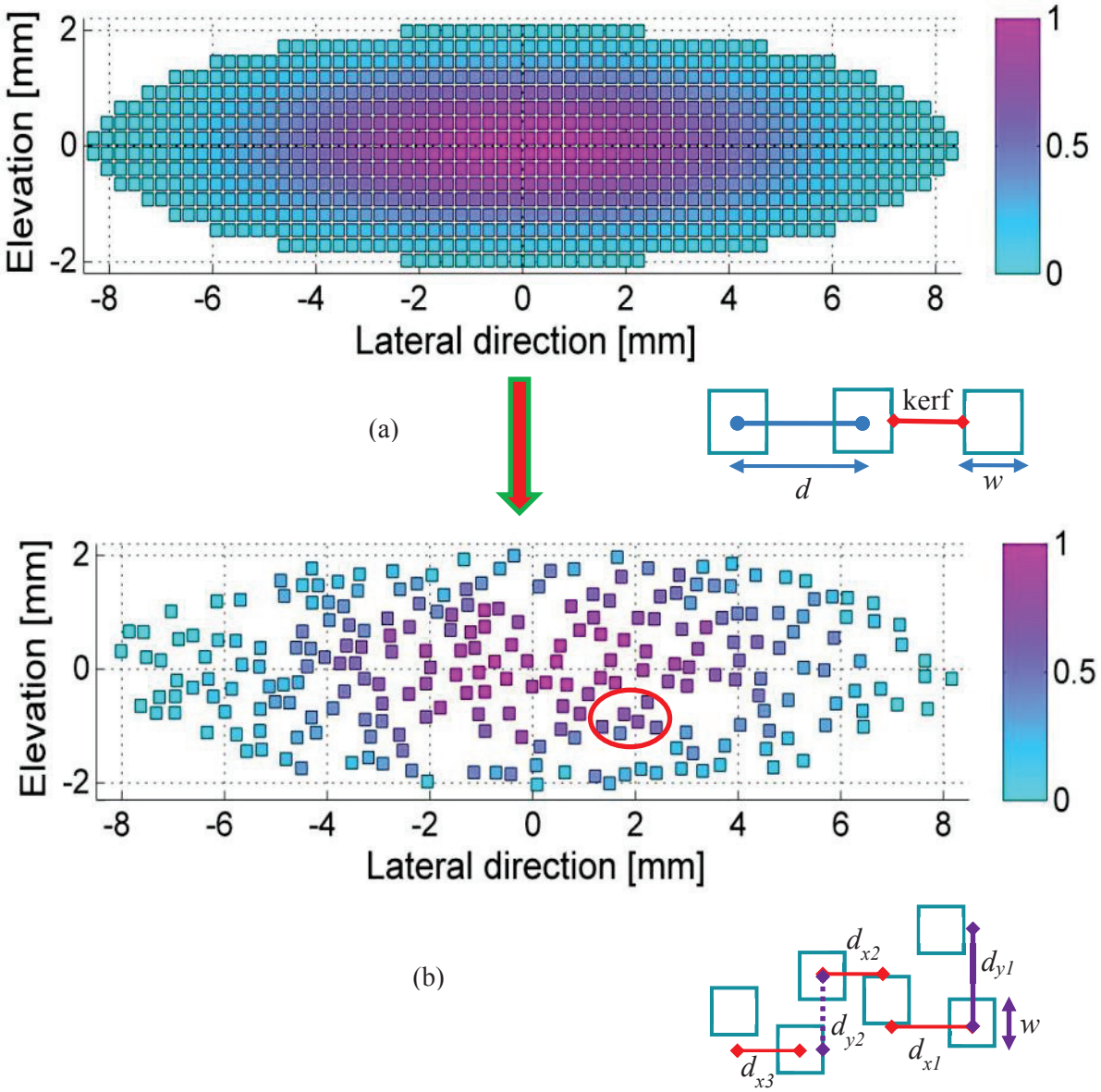

Figure 3.3 : (a) the circular part of the 64x16 2D array (828 elements) in which the inter-element distance is maintained constant and (b) the illustration of the non-grid random sparse array with a completely random position for each element avoiding overlap between elements (256 elements). The elements position does not follow a specific law, so any periodicity does not exist which implies theoretically a complete suppression of the grating lobes making possible the use of wide elements to improve the array energy and a natural reduction of the active element number for a given array footprint.

3.3.2. General beam characteristics

The beam characteristics of the standard sparse array are compared to those of the non-grid sparse array. In this comparison the same footprint is adopted and the same active element number (256). This comparison aims to understand the consequences of unwanted parts (grating lobes) of the beam pattern on the resulting images.

3.3.2.a Comparison of the PSF

To obtain the PSF of the two arrays, the phantoms of Figure 2.11a-b are used in the steered and unsteered cases, respectively. A dynamic focusing is realized in reception at five focal points (40, 45, 50, 55, 60 mm) to coincide with the scatterers positions whereas only one focus point is used in transmission at 50 mm.

Unsteering case

In the lateral direction, as the elements are $\lambda/2$ wide, if no steering is involved the five reflectors are clearly visible without any apparent effect of grating lobes in both array configurations (Figure 3.4c-d).

In the elevation direction, because of the probe small size, the ratio between the main and the grating lobes energy is lower. The consequence of this low energy ratio is a significant image contrast reduction compared to the lateral direction. When the scatterers are on the probe axis, the grating lobes remain important in the standard sparse array (Figure 3.4e) while they disappear completely in the non-grid sparse array in Figure 3.4f.

Steering case

In the lateral direction, the standard sparse array PSF presents copies of the real scatterers (Figure 3.4g). The first copies close to the main scatterers are due to the sidelobes and can be considerably reduced using an optimization algorithm whereas the second copies beginning at -30° come from the grating lobes. The latter have more energy and cause an image contrast reduction by deteriorating the signal to noise ratio. Using the proposed non-grid array, the side and grating lobes effect is not visible. More generally some sidelobe effects may still exist depending on the apodization (Figure 3.4h).

In the elevation direction, the grating lobes become more important and get closer to the probe axis (Figure 3.4i). With the non-grid array, the grating lobes are suppressed (Figure 3.4j). This example shows how important is finding a strategy to remove the unwanted parts of the array beam to guarantee a better images quality.

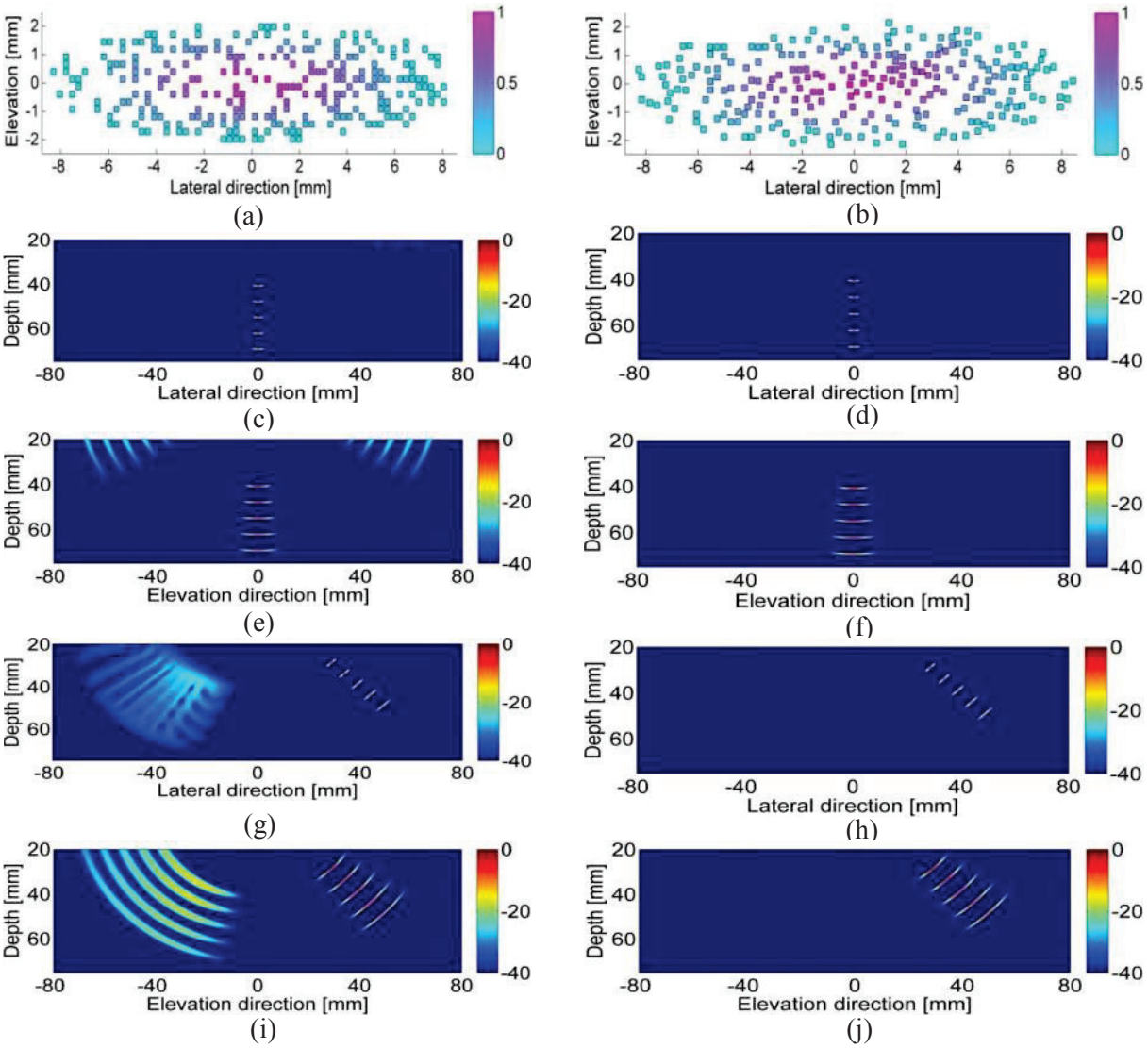

Figure 3.4 : basic examples of comparison of the PSF of the 256-elements (0.5 λ width) (a) standard sparse and (b) non-grid arrays with a hanning apodization. Illustration and comparison of the grating lobes effect in unsteered case (c)-(d) and (e)-(f) and in the steered case (g)-(h) and (i)-(j) in the lateral and elevation directions, respectively of the two 2D arrays. In the standard sparse array the grating lobes are so important that they modify the image quality and make difficult its interpretation while in the non-grid array technique the effect the grating lobes is negligible.

3.3.2.a Comparison of the beam profiles

The beam profile phantom, reported in Figure 2.11c is used for the beam pattern study. Both cases, i.e. with and without steering, will be addressed.

Unsteering case

In the unsteering case, the c-scan planes permit to put in evidence the presence of the grating lobes on the axis and on the diagonals in the standard sparse array (Figure 3.5a) whereas they are almost null in the non-grid technique (Figure 3.5b). The sidelobes are spread over the whole plane in both methods.

In the lateral direction the grating lobes level is -35 dB in the standard sparse array (Figure 3.5c) and - 41 dB in the non-grid array (Figure 3.5d), 6 dB better. In both cases the maximum sidelobes (around the main lobes) are about -35 dB.

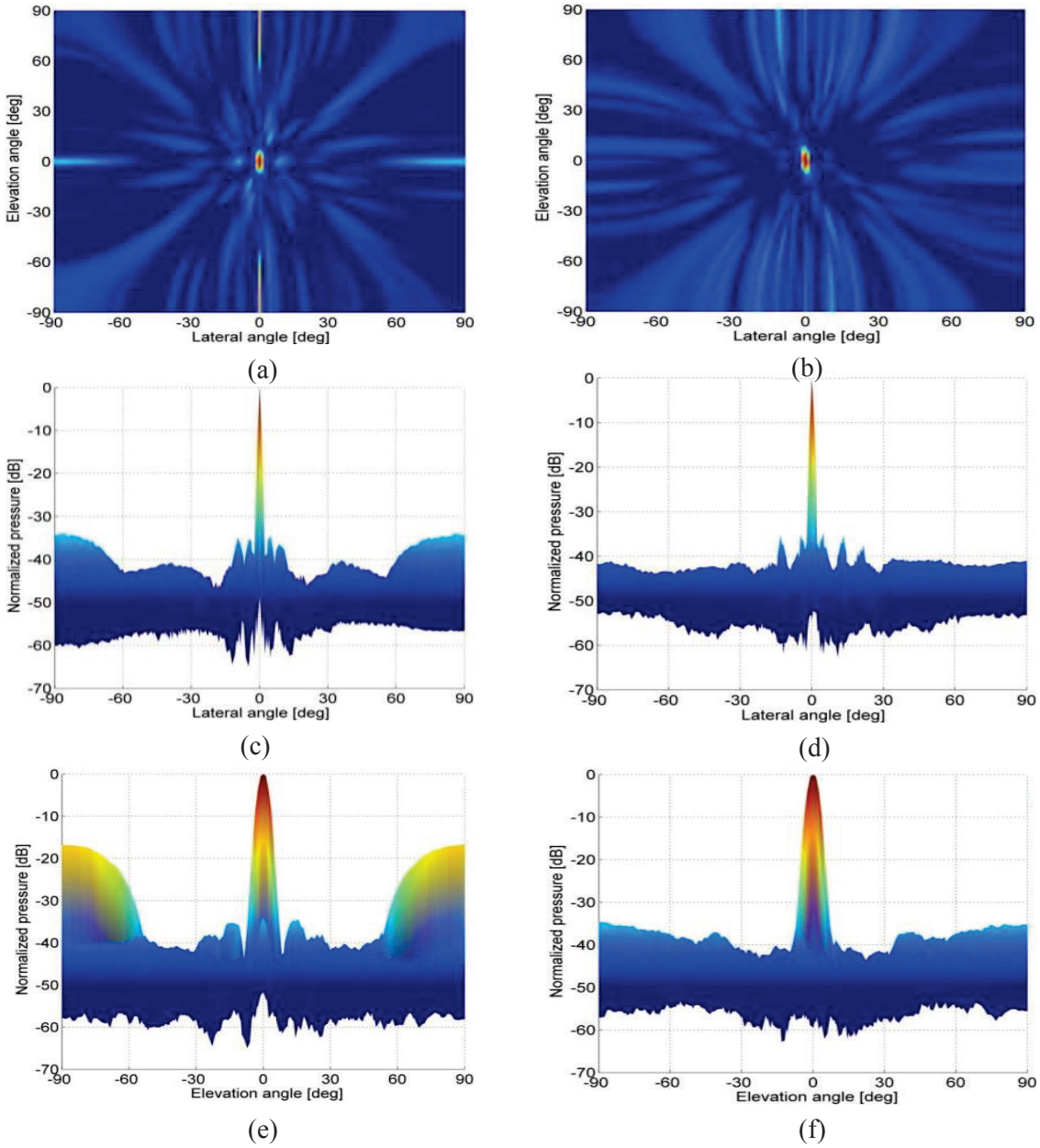

Figure 3.5 : Beam pattern of the two arrays (c)-(d) c-scan, (e)-(f) lateral direction and (g)-(h) elevation direction beams with the standard sparse and the non-grid sparse array, respectively. The scatterer is placed on the array axis.

In the elevation direction, the grating lobes reach -18 dB in the standard sparse array (Figure 3.5e), 16 dB higher than those of the non-grid array (Figure 3.5f). The main lobes remain constant as they are not much sensible to the individual elements position. The major improvement shown by Figure 3.5 provided by the non-grid array is the cancellation of the grating lobes. The grating lobes are very disturbing in phased array imaging because they constitute a source of image artifacts (noise). Their echoes can even be greater than that of the main lobe in some configuration distorting the images interpretation. They hinder the optimal use of the 2D array by imposing small elements as established in (2.12) deteriorating the array

sensitivity. By removing this obstacle, it becomes possible to propose arrays with wide element leading to an increased active surface, thus a better sensitivity (high signal-to-noise ratio) and to scan large sectors.

Steering case

The same experiment is carried out with the scatterer placed at 45° in both directions using the same arrays presented in Figure 3.5a-b.

The beams of Figure 3.6a-b correspond to the c-scan planes of the standard and the non-grid sparse arrays. The main lobe has the same properties in the two arrays but the principal difference is the grating lobes as in the unsteering case. In both the lateral and elevation directions, with the standard (Figure 3.6c-e) as the non-grid (Figure 3.6d-f) sparse arrays, the grating lobes results remain in the same order compared to the unsteering case (Figure 3.5). The main change is in their positions.

To generalize the potential improvement provided by the non-grid positioning strategy, we realize a statistical study with a huge number of simulations and compare the results to the regular-grid sparse arrays. The footprint of the two probes is maintained identical for each configuration. The results of this in-depth study are presented in the next section.

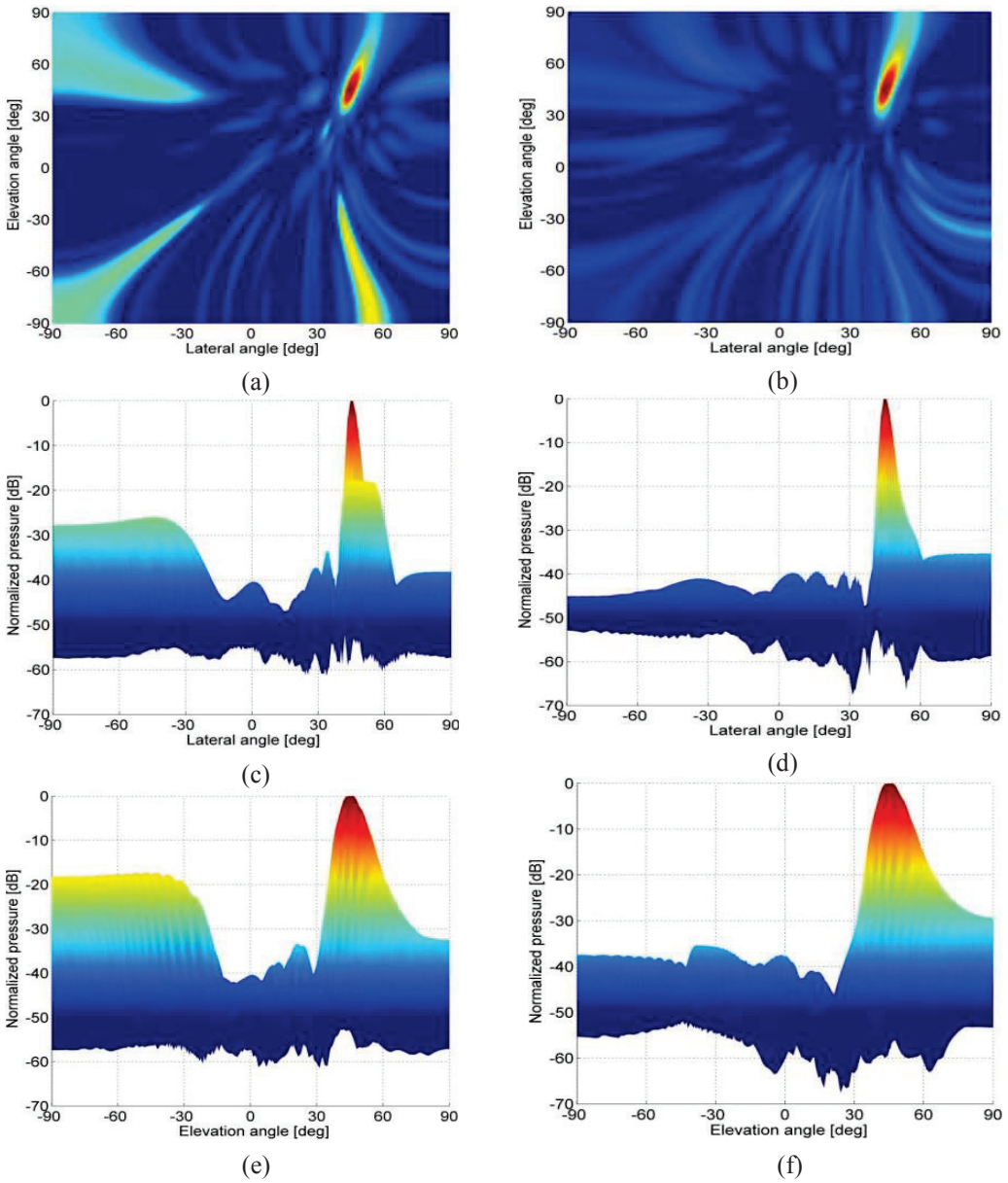

Figure 3.6 : example of comparison of the beams of the 256-elements (a) standard sparse and (b) non-grid array. Beam correspond to (c)-(d) c-scan, (e)-(f) lateral direction and (g)-(h) elevation direction with the standard sparse and the non-grid sparse array respectively. The scatterer is placed at (45°, 45°) in lateral and elevation directions.

3.3.3. Influence of the element size

The effect of the piezoelectric elements size on the 2D arrays beam characteristics (main and grating lobes) is presented. The aim of this simulation is to put in evidence the possibility of using few elements with larger surface to increase the array's sensitivity and to make easy the connection of the 2D arrays to current scanners keeping good beam properties.

In the literature, the impact of single element size on the beam of the full array is established by [Brandwood (2012)] emphasizing the importance of the element size on the beam amplitude. The theoretical background of the single element contribution to an array beam is detailed in the Section 2.4.1.b (equation (2.13) to (2.17)). The direct consequence of the element widening is the increase of the active surface of the array (better sensitivity). In addition, for a constant array footprint the active element number is reduced (for instance the 64x16 2D array contains 1024 elements of 0.5 λ while only 400 elements of 0.8 λ width are needed).

The example to put in evidence these theoretical expressions uses three regular dense arrays covering the same footprint about 17x4.2 mm². Figure 3.7a presents the array containing 828 elements of 0.5λ wide each (0.6 λ pitch), in (b) the 440 elements are 0.7 λ wide each (0.8λ pitch) and the last array in (c) composed of 264 elements of 0.9 λ wide (1 λ pitch). The beam profiles in Figure 3.7d illustrate the advantages and the disadvantages of the element size on the 2D array beam when the footprint is maintained constant. In one hand, the sensitivity of the arrays increases as a function of the element size as the active surface of the probe is maximized [Kojima (1986), Jian-Yu Lu and Greenleaf (1994)]. On the other hand the grating lobes get higher and higher and become closer to the main lobe. This example shows the limitations of the standard element disposition techniques in the realization of such arrays. The in-depth simulations aim to test the additional improvement and possibilities provided by the non-grid array. The ideal and expected result is an efficient suppression of the grating lobes independently of the element size to be able to make use of the advantages of the element widening.

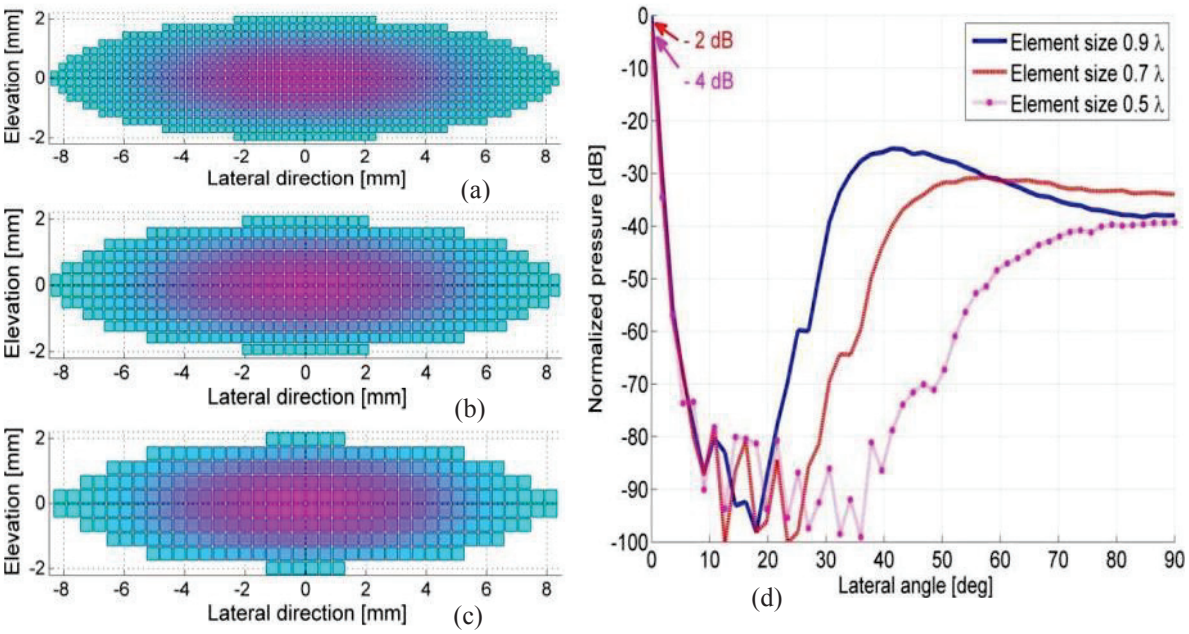

Figure 3.7 : the same probe footprint filled with (a) 788 elements of 0.5 λ (b) 440 elements of 0.7 λ (c) 264 elements of 0.9 λ and (d) their beam profiles normalized by that of the array in (a). The kerf is fixed to 0.1 λ for each case.

3.3.3.a Simulation set-up

All the results correspond to simulations of the two-way beams obtained using the phantom of Figure 2.11c and by steering the transmitted beam over a wide range of angles (typically from - 90° to 90°). The transmit (TX) and receive (RX) foci are set to coincide with the scatterer depth.

Two reference dense-arrays are considered: a square 64×64 grid and a rectangular 64×16 grid, both with deactivated edge elements [Turnbull and Foster (1991)]. The sizes of these dense array probes are 17 mm × 17 mm in the square case and 17 mm × 4.2 mm in the rectangular case. The latter dimensions were suggested by physicians for possible liver biopsy applications needing intercostal imaging. The elements are squares. In the 4:1 rectangular case, the direction of the largest dimension of the probe is called the lateral direction, and the other is called the elevation direction. In the square case there shall be no distinction since the beam is symmetric. The standard and the non-grid sparse arrays are derived from the dense arrays by using respectively the methods described in Sections 2.4.2.d and 3.3.1. The performance of sparse arrays with and without grid-positioning constraints is systematically compared.

Parameter	Value	
	64x64 array	64x16 array
Central frequency	3.5 MHz	
Wavelength (λ)	0.44 mm	
Element number	256	100
Pitch (*d*)	From 0.3 to 1.1 λ	

Table 3.1: simulation parameters used for studying the influence of the element size. Exceptionally both 64x64 and 64x16 arrays are studied in this section to have more general results. The number of active elements is 100 in the 64x16 array and 256 in the 64x64 arrays.

3.3.3.b Results

Figure 3.8 and Figure 3.9 show the grating-lobe level and the width of the main lobe obtained with standard and non-grid sparse arrays when the element size varies between λ/5 and λ. The number of active elements has been set to 256 for the square case and to 100 for the rectangular case. Each box summarizes the statistics of 100 simulations for a fixed element size (the upper and lower edges of each box represent the 75th and 25th percentiles, respectively, and the central mark is the median). The grating-lobe level of standard sparse arrays tends to increase with increasing element size, while the grating-lobe level of non-grid sparse arrays remains approximately constant. Moreover, the latter one is 9 dB to 25 dB lower than the level obtained with standard sparse arrays. Besides, we can see from Figure 3.9 that non-grid positioning does not increase the width of the main lobe but even slightly reduces it in the elevation direction.

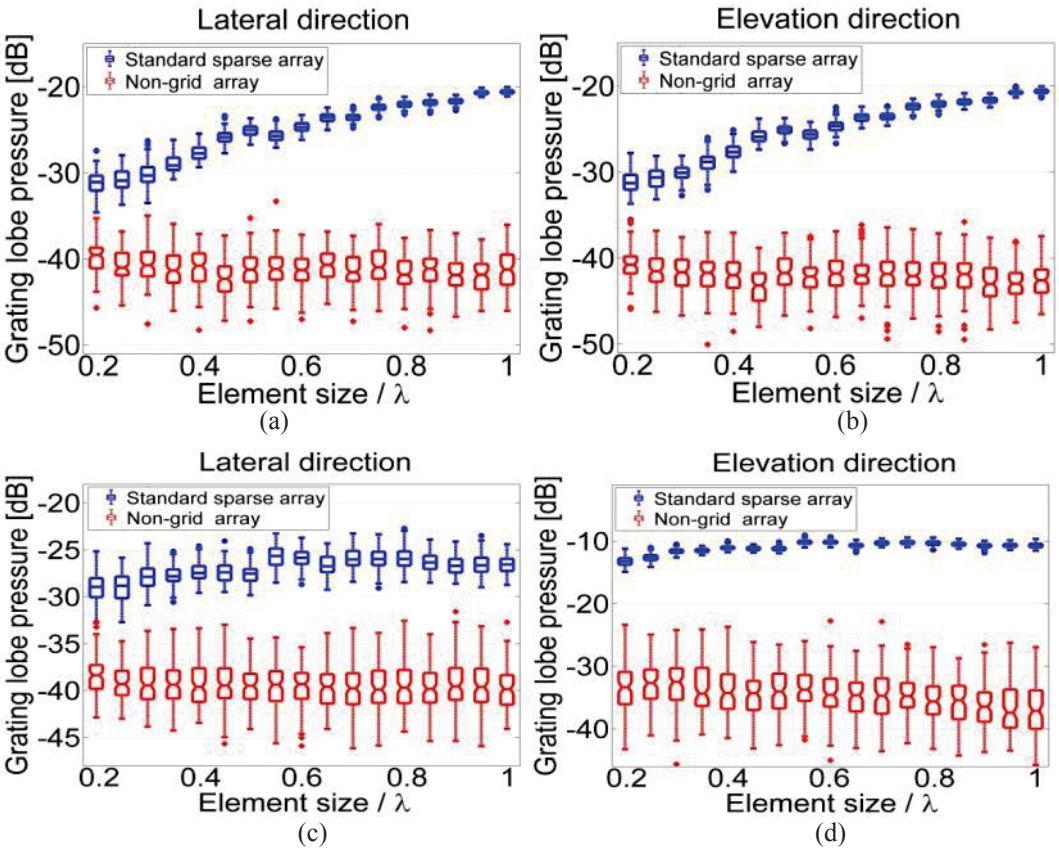

Figure 3.8: these boxplots represent the evolution of the grating lobes as a function of the active element size in the standard and the non-grid array techniques (each box represents 100 simulations): (a)-(b) square probes with 256 active elements; (c)-(d) 4:1 rectangular probes with 100 active elements. The results confirm the efficiency of the non-grid array to provide much reduced grating lobes even though the element size increases contrary to the standard sparse array which grating lobes increase as the element size does. This property of the non-grid array permits to maximize the 2D arrays imaging capabilities and to reduce their necessary usual huge number of channels.

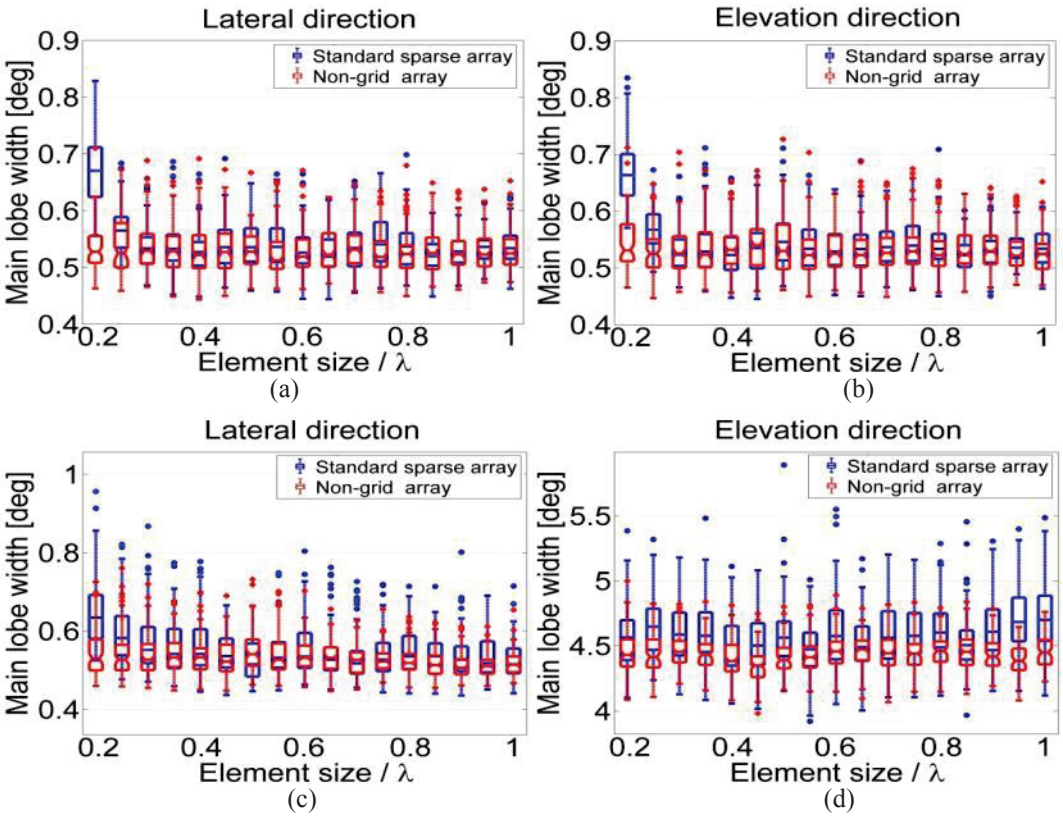

Figure 3.9: the evolution of the main-lobe width as a function of the elements size (each box represents 100 simulations): (a)-(b) square probes with 256 active elements; (c)-(d) 4:1 rectangular probe with 100 active elements. The main-lobe width determines the lateral and elevation resolution of the 2D array. The boxplots show that the non-grid array has at least the same (or better) man lobe as the standard sparse array.

3.3.4. Influence of the element number

The impact of the number of piezoelectric elements on the 2D arrays beam characteristics (main and grating lobes) is presented. The main purpose of this simulation is to compare the standard and the non-grid sparse arrays in terms of beam properties on a wide range of active elements number.

Theoretically, under the assumption that all elements have the same apodization coefficient, the equation (2.17) shows, by the term w_{ij}, that with more active elements the PSF of the array has a more important energy. The active element number has less impact on the main lobe width when the probe footprint is fixed, but the probe energy level considerably increases. An illustration of the main lobe width constancy is shown in Figure 3.10 whereas the energy loss passing through the dense to the sparse arrays was discussed the Section 2.4.2.d .

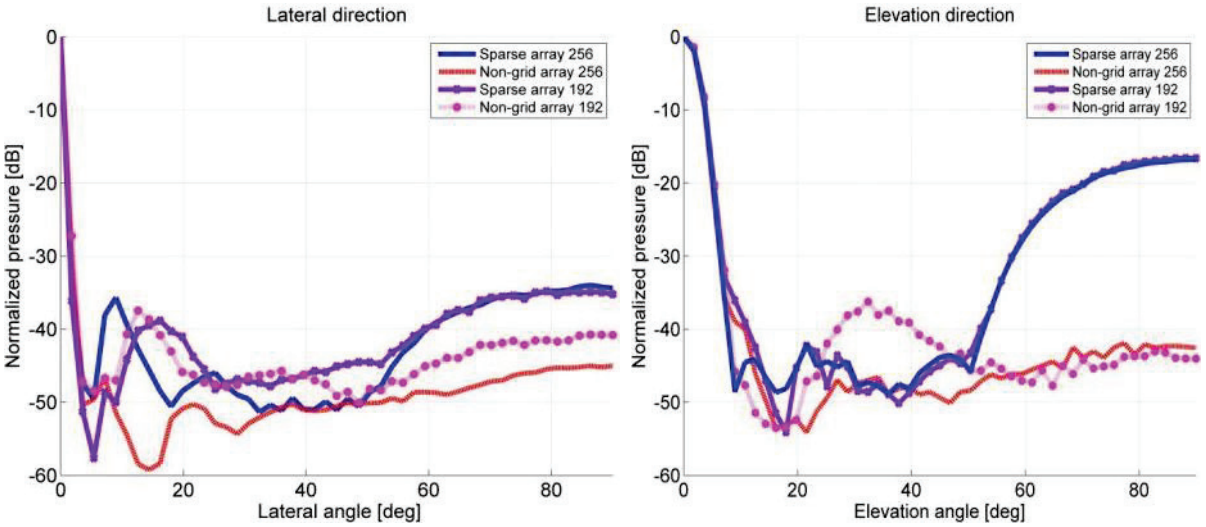

(a) (b)

Figure 3.10 : comparison between the sparse and the non-grid arrays when element number is 256 (continuous line and dashed line respectively) and 192 (lozenge line and dotted line respectively) in (a) lateral and (b) elevation directions. These results illustrate the constancy of the main lobe and the variation of the grating lobes as the active elements number varies. Element size is kept to 0.5 λ.

Figure 3.10 shows the idea of active element number variation developed and represented by the boxplots in Figure 3.11 and Figure 3.12. The beam profiles present a comparison between the standard and the non-grid sparse arrays when filled with 256 and 192 active elements. With 256 active elements, the grating lobes value is -35 dB in the standard sparse array against – 45 dB in non-grid array in lateral direction (Figure 3.10a), both methods present the same main lobe width. The sidelobes are subject to the elements apodization and can change from an example to another. In elevation direction the grating lobes value are -18 dB and - 41 dB in standard and non-grid array, respectively. When filled with 128 elements the difference of the grating lobes is 6 dB and 25 dB in lateral and elevation direction at the advantage of the non-grid array. To generalize these values, the simulation is made on the large range of active elements to establish a global tendency of the behaviors of the non-grid array compared to the standard one.

3.3.4.a Simulation set-up

For standard sparse arrays, the condition (2.12) causes a widening of the main lobe.

Parameter	Value	
	64x64 array	64x16 array
Central frequency	3.5 MHz	
Wavelength (λ)	0.44 mm	
Element size (λ/2)	0.22 mm × 0.22 mm	
Element number	From 64-1024	From 64- 576
Pitch (*d*)	0.6 λ	

Table 3.2: Simulation parameters used for studying the influence of the number of active elements. The active element number in 64x64 array varies from 64 to 1024 and from 64 to 576 in the 64x16 arrays. The footprint of the standard and the non-grid sparse arrays is kept constant for each element number.

Hence, a pitch value slightly above the half-wavelength is a good trade-off. We set $d = 0.6\,\lambda$ and $w = 0.5\,\lambda$, and the simulation parameters are listed in Table 3.2 (the pitch value is not relevant for non-grid sparse arrays). A number of elements ranging from 64 to 1024 is activated for the square 64x64 arrays and from 64 to 576 in the 4:1 rectangular arrays. The positions of the activated elements are random when there is no grid constraint.

3.3.4.b Results

The results are presented in box plots and each box summarizes the statistics of 100 simulations for a fixed number of active elements (the upper and lower edges of each box represent the 75th and 25th percentiles, respectively, and the central mark is the median). The rationale for this type of representation is to provide a comparison between standard and non-grid arrays that is independent of the optimization method. Figure 3.11 displays the statistics of the grating-lobe levels in the lateral and elevation directions as functions of the number of active elements. The grating-lobe level of non-grid arrays is significantly lower and decreases faster than that of standard arrays. For square probes, the average reduction of the grating-lobe level produced by random element-positioning ranges from -3 dB to -15 dB. In the 4:1 rectangular case, this reduction ranges between -3 dB and -17 dB in the lateral direction and between -12 dB and - 27 dB in the elevation direction.

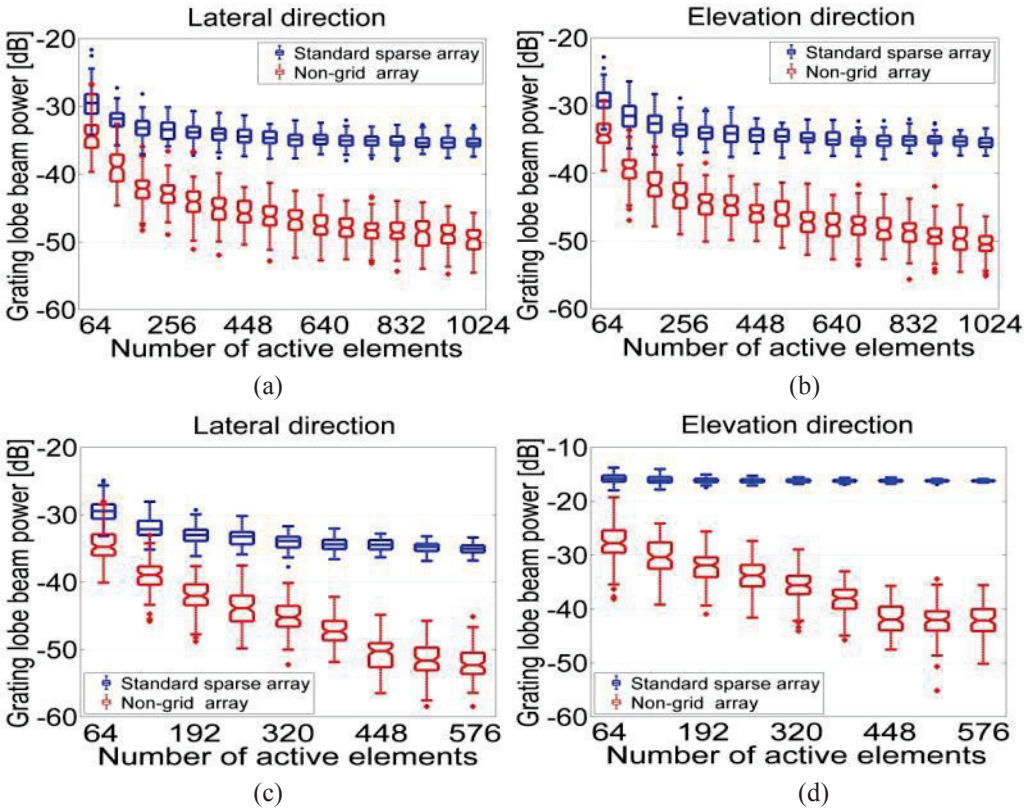

Figure 3.11: Grating-lobe level in the lateral and elevation directions as a function of the number of active elements (each box represents 100 simulations): (a)-(b) square probes; (c)-(d) 4:1 rectangular probes. The grating lobes decrease as the active element number increase in both methods but the non-grid array presents a faster and more decreasing scheme.

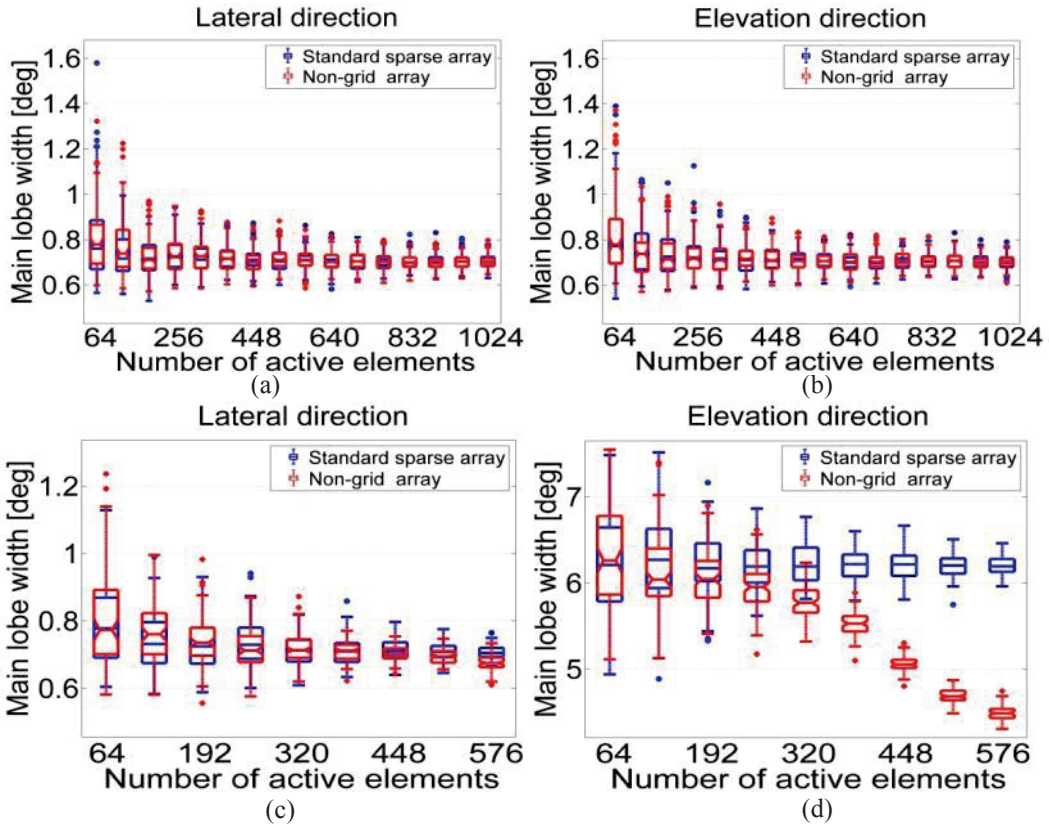

Figure 3.12: Main-lobe width as a function of the number of active elements (each box represents 100 simulations): (a)-(b) square probes; (c)-(d) 4:1 rectangular probes. The main lobe width remains the same in all directions except the elevation direction of the 64x16 arrays. In this latter, the non-grid array present a thinner main lobe when active element get greater than 256. This advantage may come from a better use of the probe surface in this direction using the non-grid technique.

3.4. Variable size non-grid array

In this section, the variable size array, a declination of the non-grid element placement strategy is presented. A comparison is realized with the standard sparse array when both are filled with 256 elements.

3.4.1. Method description

The variable size non-grid array is an extension of the non-grid array technique [B. Diarra, Liebgott, Cachard, et al. (2012)] described in the Section 3.3. It aims at improving some limitations which may be due to the non-grid array technique. For ultrasound imaging, the non-grid array is a better solution than the standard grid based arrays as it provides better resolution and a better sensibility to the array but for applications needing a large main lobe (directivity), the use of wide elements is not the best solution as they are too directive. To keep the signal-to-noise ratio improvement property of the non-grid array technique and at the same time maintain a large directivity, size varying elements is good solution (Figure 3.13). The small elements contribute a lot to the beam directivity whereas the large ones provide a good sensitivity. This array presents the property to increase the irregularity of the non-grid array and thus contributes to a more reduced grating lobes effect [Bakary Diarra et al. (2013)].

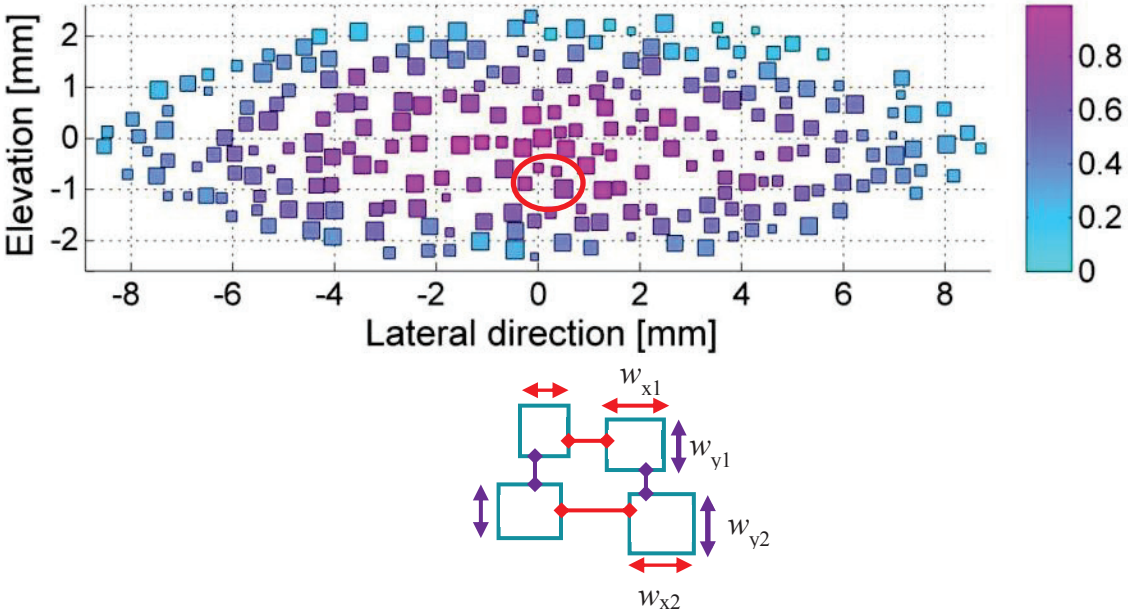

Figure 3.13: principle of variable-size non-grid array. The element size is randomly chosen in an interval between 0.4 λ and 0.8 λ. The conjugation of the randomness of the element size and their positions extremely decreases the grating lobes and permit to obtain a good sensitivity and directivity.

The realization of such an element positioning from the non-grid array is not easy. In the non-grid array presented in Section 3.3. , the element size is constant and it is quite simple to choose a condition controlling the overlap between neighboring elements. In the variable size array, each element has its size chosen randomly in the predefined interval and any condition does not suit to all of them to avoid overlap. To resolve this problem, the overlap control function uses the size of each single element during its placement to know if any previous element has not occupied the position chosen. This strategy permits to maintain the same probability of finding a position for each element.

3.4.2. General beams characteristics

The beam characteristics of the variable size array are compared to those of the standard sparse array with a number of active elements fixed to 256. The size of the elements of the standard sparse arrays (w) is kept equal to a mid-wavelength ($\lambda/2$) when the element size ranges from 0.4 λ to 0.8 λ (a wider interval can be used) in variable size array (Figure 3.14b). The array footprint is constant and identical in the two cases.

The PSF phantoms presented in Figure 2.11a-b are used to perform the PSF of both arrays. In the lateral direction, if no steering is considered, the two arrays have the same PSF given by Figure 3.14c and d. When the scatterers are off-axis, the mirror images of the scatterers due to the grating lobes appear in the standard sparse array PSF (Figure 3.14e) while any effect is detected using the variable size array (Figure 3.14f).

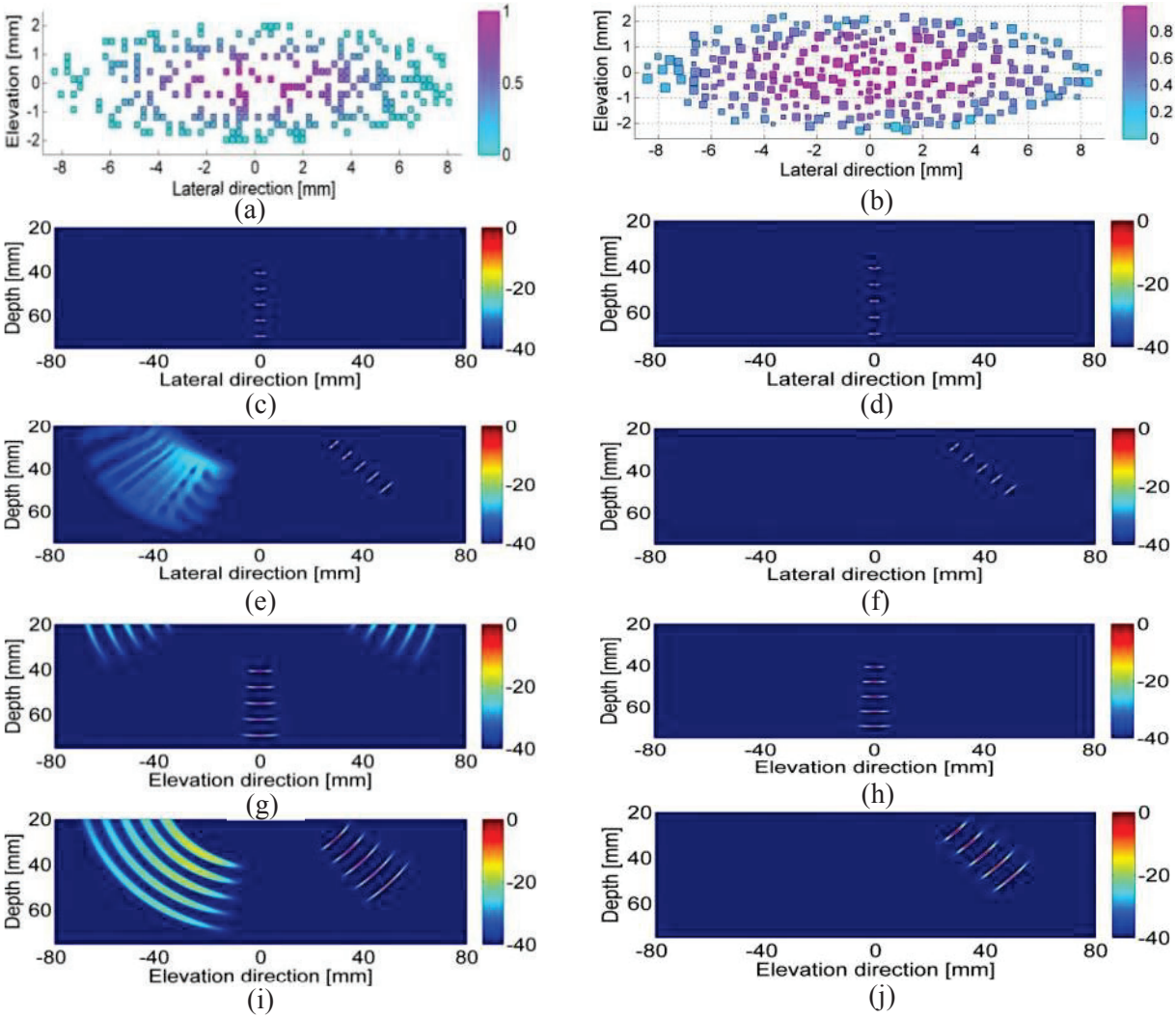

Figure 3.14 : comparison of the PSF of the 256-elements of 0.5 λ width (a) standard sparse and (b) variable size array with a hanning apodization. Illustration of the grating lobes effect in unsteered (c)-(d) and steered (at 45°) cases on the 2D array PSF. In standard sparse array the grating are so important that they modify the image quality and make difficult its interpretation while in the variable size array technique any grating lobes effect is not visible.

In the elevation direction, in both steering and unsteering cases, the standard sparse array present grating lobes effect (Figure 3.14g-i) whereas any grating lobes is noticeable with the variable size (Figure 3.14h-j).

3.5. Optimization results

In this section, first, the optimization methods proposed in literature (equation (2.28) and (2.29)) and our improved version (equation (3.4)) are compared. This comparison is conducted only on the regular standard sparse array. In the rest of the optimizations, we use the improved version of the algorithm. Secondly, the optimization is applied to the non-grid and the variable size arrays, new element positioning strategies proposed in this study. In all the optimizations, the edge elements reduction technique is combined to the sparse filling of the arrays to further reduce its active elements number.

The optimization is applied to all the array configurations presented: the standard sparse array, the non-grid array and to the variable size element array. The final active element number and the sidelobes level value are the main outputs of the optimization. In each case, the PSF and the beam profile of the optimized array are compared to those of the corresponding dense array. The energy loss and the beam deterioration due to the element number reduction are presented too. The main purpose of these comparisons is to illustrate the beam improvement capabilities in terms of grating lobes reduction, energy maximization, main lobe thinning and active element number reduction, provided by the proposed non-grid technique. The reference dense array is the ellipsoidal part of the 64x16 2D array containing 828 elements.

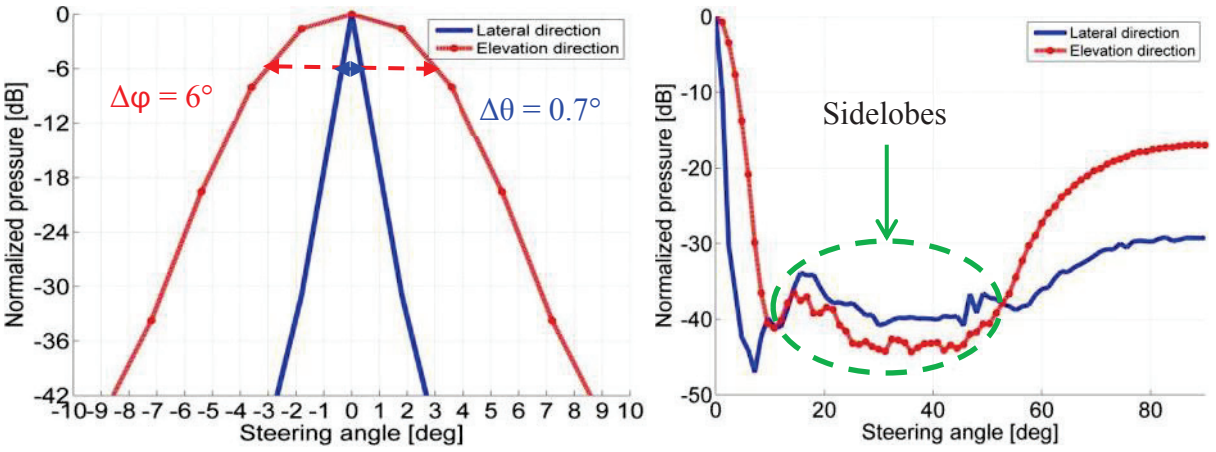

Figure 3.15: (a) 64x16 dense array main-lobe width in lateral and elevation direction and (b) the sidelobes apparition when the 2D array is sparsely filled without any optimization. The main-lobes are used to initialize the algorithm when optimizing sparse arrays.

The algorithm input parameters are:

- the authorized sidelobes level $p_s = -40$ dB,
- the main lobe width set to be equal to that of the dense array at – 6 dB,
- the number of iteration M fixed in each optimization with a complete visit of the whole probe in each iteration.

The stabilization term determining the relative importance of the different parts of the cost function (μ) is set to $4e^{-5}$ and to $1.5e^{-5}$ as in [Trucco (1999)]. This stabilization

coefficient can vary between 1e−5 and 1e−3 without noticeable change on the optimization results. The threshold of optimization coefficients is $\beta = 0.2$. The 2D array is filled about 50 to 40% at the beginning of the algorithm (any percentage can be used but not directly the dense array).

3.5.1. Optimized standard sparse array

The optimization results presented are performed using the new approach we proposed [B. Diarra, Liebgott, Robini, et al. (2012)] and they are compared to the best one obtained with the (reference) methods of [Trucco (1999)] and [Chen et al. (2010)]. The number of iterations is fixed to 5000.

3.5.1.a Evolution of element number and beam profiles

The optimization enables a reduction of 79% of the element number (from 828 to 170) using the proposed technique. For the same beam characteristics, the reference methods provide a reduction of about 72% (from 828 to 235). The mean value of active element number decreases to 172 after 200 iterations and remains stable till 1500 iterations. The lowest value 170 is reached after 1501 iterations and remains till the end of the optimization (Figure 3.16a). The standard deviation of the active element number is 6 and the cost function mean value decreases slightly during the optimization (Figure 3.16b).

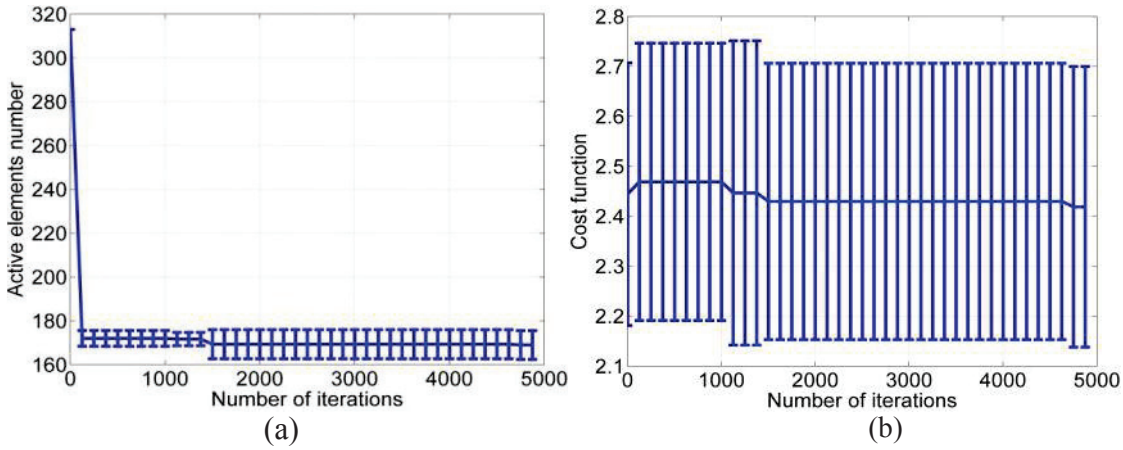

Figure 3.16: (a) the evolution of active elements number in 7 optimizations processes of the 64x16 sparse array and (b) the cost function evolution as a function of the iterations number. The standard deviation of the active element number is 6 and that of the cost function is about 0.3 unit.

In terms of beam features, the lateral direction sidelobes are lower than -40 dB as expected and its main lobe width is 0.6° in the sparse array against 0.7° in dense array (Figure 3.17c). The sparse array provides a main lobe of 4.6 degree while that of the dense array is 6° in elevation direction. The sidelobes are 3 dB higher than expected in this direction (Figure 3.18d). A slight reduction of the grating lobes level is noticed falling from -35 to -39 dB and from -16 to -19 dB in lateral and elevation direction, respectively. The energy loss caused by the element reduction to 170 is about 15 dB, the same in each direction (Figure 3.19e-f). In practice, this energy loss is important and it has an impact on the array imaging features mainly the penetration depth.

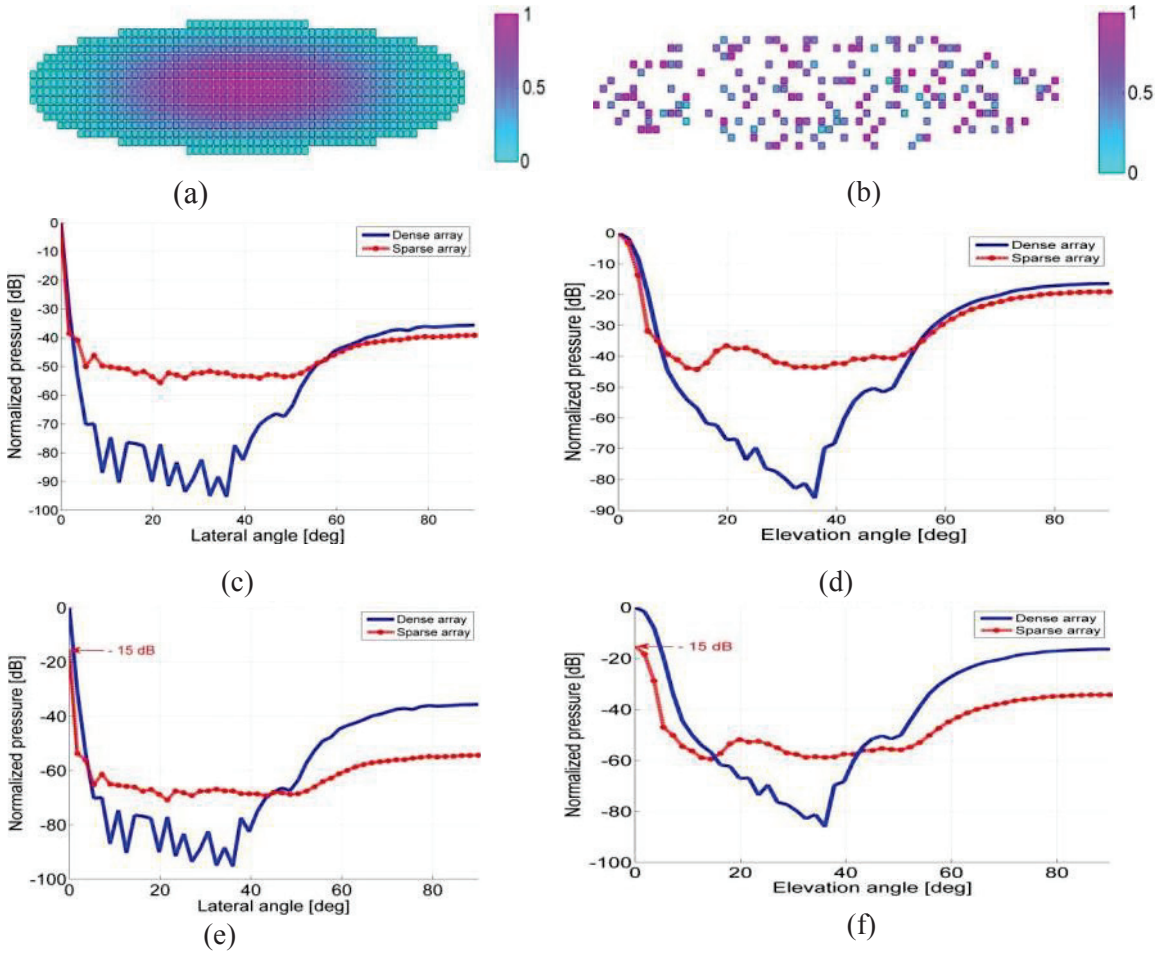

Figure 3.17: comparison of the beam profiles of (a) the dense array of 828 elements and (b) the optimized sparse arrays of 170 elements in (c)-(e) lateral and (d)-(f) elevation directions. Beams (c)-(d) show the ratio between the main lobe and the grating of each array, (e)-(f) represent the energy loss caused by the sparse array technique which is 15 dB.

3.5.1.b Comparison of PSF

The comparison aims to put in evidence the imaging capabilities of the optimized arrays compared to the dense array. The PSF is simulated in both unsteered and steered cases using the PSF phantoms presented in Figure 2.11a-b. If no steering is involved, the PSF of the dense array (Figure 3.18a) and that of the sparse array (Figure 3.18b) are similar in the lateral direction while an improvement of the resolution is provided by the sparse array in elevation direction (Figure 3.18d). This resolution improvement comes from the main lobe reduction noticed in Figure 3.17d, the grating lobes effect is less significant too. In the steering case, the scatterers are placed at (45°, 45°) in the two directions. Contrary to the unsteering case the grating lobes are visible in the lateral direction with both the dense (Figure 3.18e) and the sparse array (Figure 3.18f) and their effect is more increased in the elevation direction (Figure 3.18g-h). This increase is linked to the fact that when the beam is steered, the grating lobes which were outside the field of view become completely visible at the same time as the main lobe. The sidelobes are slightly higher than – 40 dB in the elevation direction (Figure 3.18d-h).

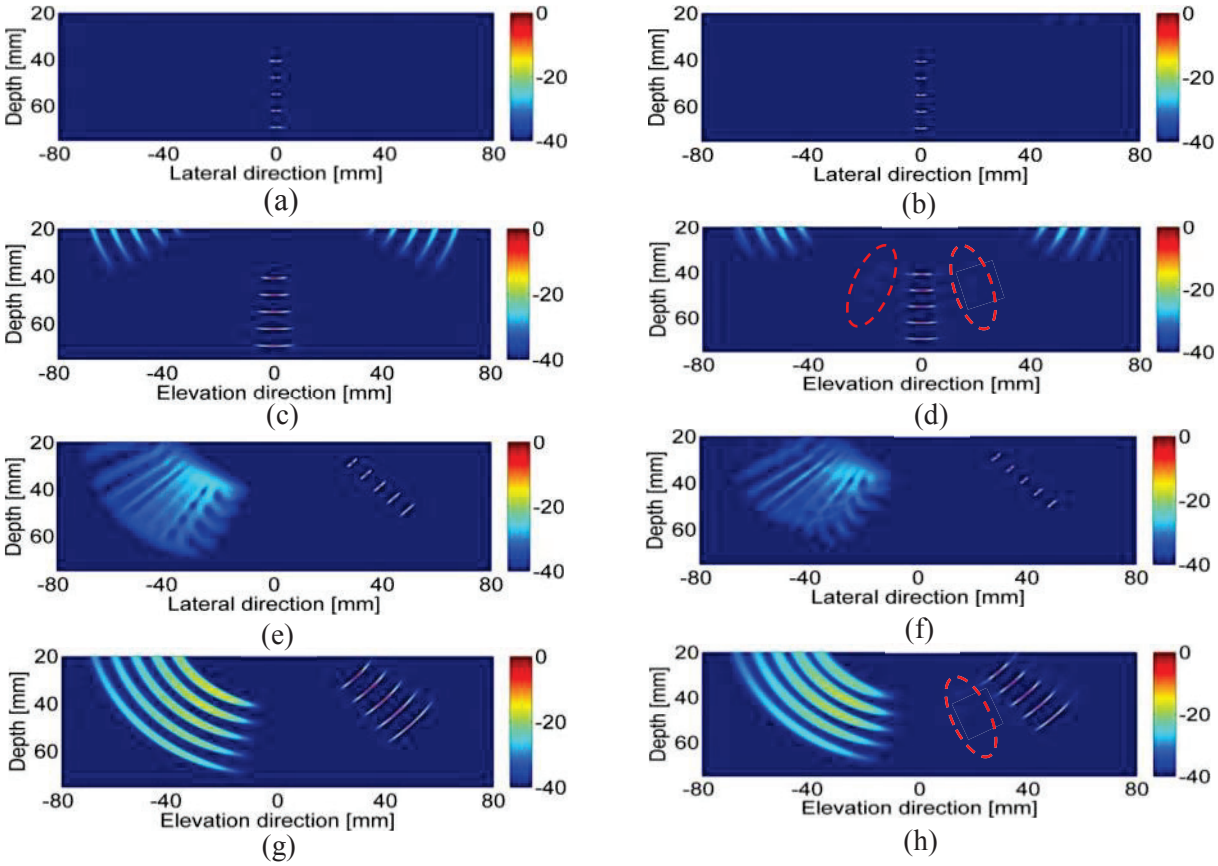

Figure 3.18: (a)-(b) and (c)-(d) are respectively the PSF in lateral and elevation direction with the dense and the optimized sparse arrays when no steering is considered, (e)-(f) and (g)-(h) are the same PSF when the scatterers are placed at (45 °, 45°) off axis. The PSF of the sparse array is similar to that of the dense array but with more important sidelobes. Howether the sparse arrays has better grating lobes reduction capabilities and a better spatial resolution (thinner main lobe).

3.5.2. Optimized non-grid sparse array

The non-grid array optimization necessitates adapting the element coordinates in the cost function because there is any relation between them as in the standard sparse array. The comparison of the results of optimized 2D sparse array and the dense array (reference) permits to appreciate the potentiality of the SA algorithm when applied to the non-grid array to allow the design of usable probes for 3D imaging.

3.5.2.a Optimization of 0.7 λ element arrays

Evolution of element number

The optimization of the non-grid array is performed when elements size is maintained constant and greater than a mid-wavelength (0.7 λ in this case) to maximize the probe active surface. For element size lower or equal to 0.5 λ, the optimization results are similar to that of the standard sparse arrays (except the grating lobes) presented in Section 3.5.1.

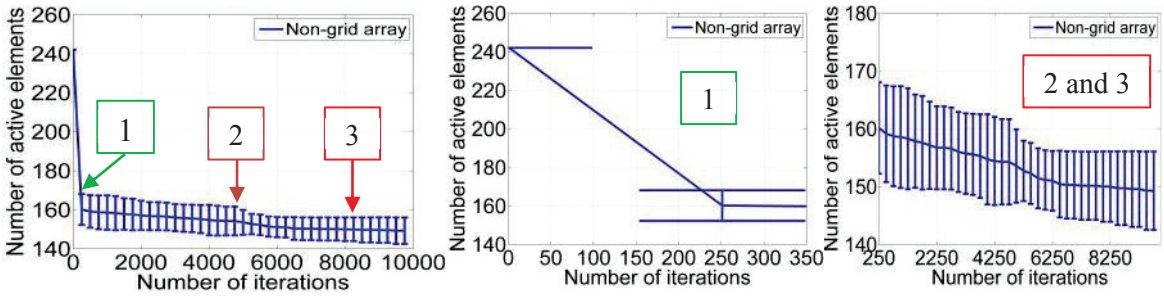

Figure 3.19: mean and standard deviation values of seven optimized non-grid arrays. The variation is about +/- 8 elements. The mean active element at the end of the optimization is 142 and presents only 8 dB energy loss compared to the dense array. Such an array can be easily controlled by most of the current scanners and makes possible fast 3D imaging. The iterations number can be chosen less than 10000 to have a good optimized array.

Figure 3.19a represents the evolution of the number of active elements during the optimization of the 64x16 non-grid array initially filled with an element number between 300 and 200. The element size is fixed to $0.7\,\lambda$ (possible with the non-grid array). The array footprint is constant and equal to that of the 64x16 dense array (Figure 3.17a). The initial element number is subject to a criterion: it must fulfill the expected beam features. If this initial number is too low to provide the imposed beam constraints (sidelobes, main lobe width) the algorithm keeps this number during all the optimization procedure because the active element number increase is not allowed during the optimization.

In the optimization process, the number of iterations is important even though up to a certain value the array thinning is slow (with few elements turned off). The evolution of the active element number in Figure 3.19a shows 3 main zones zoomed in (b) and (c); the first zone (Figure 3.19b) goes from 1 to about 250 iterations, the important part of the thinning is performed in this zone with a fast element number decrease going from 240 to 160 active elements. The second zone (Figure 3.19c) is between 250 and 6000 iterations and is characterized by a slight but a continuous decrease of the active element number from 160 to 150. Depending on the application, one may stop the optimization after some hundreds of iterations because only few elements will be deactivated after the first zone (about 10 elements in this case). The last zone goes from 6000 to 10000, only two elements are deactivated (from 151 to 149) in 4000 iterations. It is not relevant to let the optimization continue as far. The standard deviation of the optimization is about +/-8 elements between the different runs independently of the iterations number. The minimum active elements number reached is 142. This number is used for the PSF simulations.

Comparison of the PSF of the dense and the optimized arrays

The beam profile phantoms presented in Figure 2.11a-b-c are used. The sector considered ranges from -90 degrees to 90 degrees, corresponding to the maximum possible scanning area. The transmission focus is at 50 mm whereas those in reception go from 40 to 60 mm by a step of 5 mm. The results in the lateral direction when the scatterers are on the arrays axis have the same features in the two methods shown by Figure 3.20c-d. In the elevation direction, the mirror images due to the grating lobes are important in the dense array (Figure 3.20e) whereas the non-grid permits a complete suppression of any undesired effect on the PSF (Figure 3.20f). The effect of the grating lobes is more important in the steering case because the latter get close to the probe axis and thus their effect becomes more significant on the array resulting echoes.

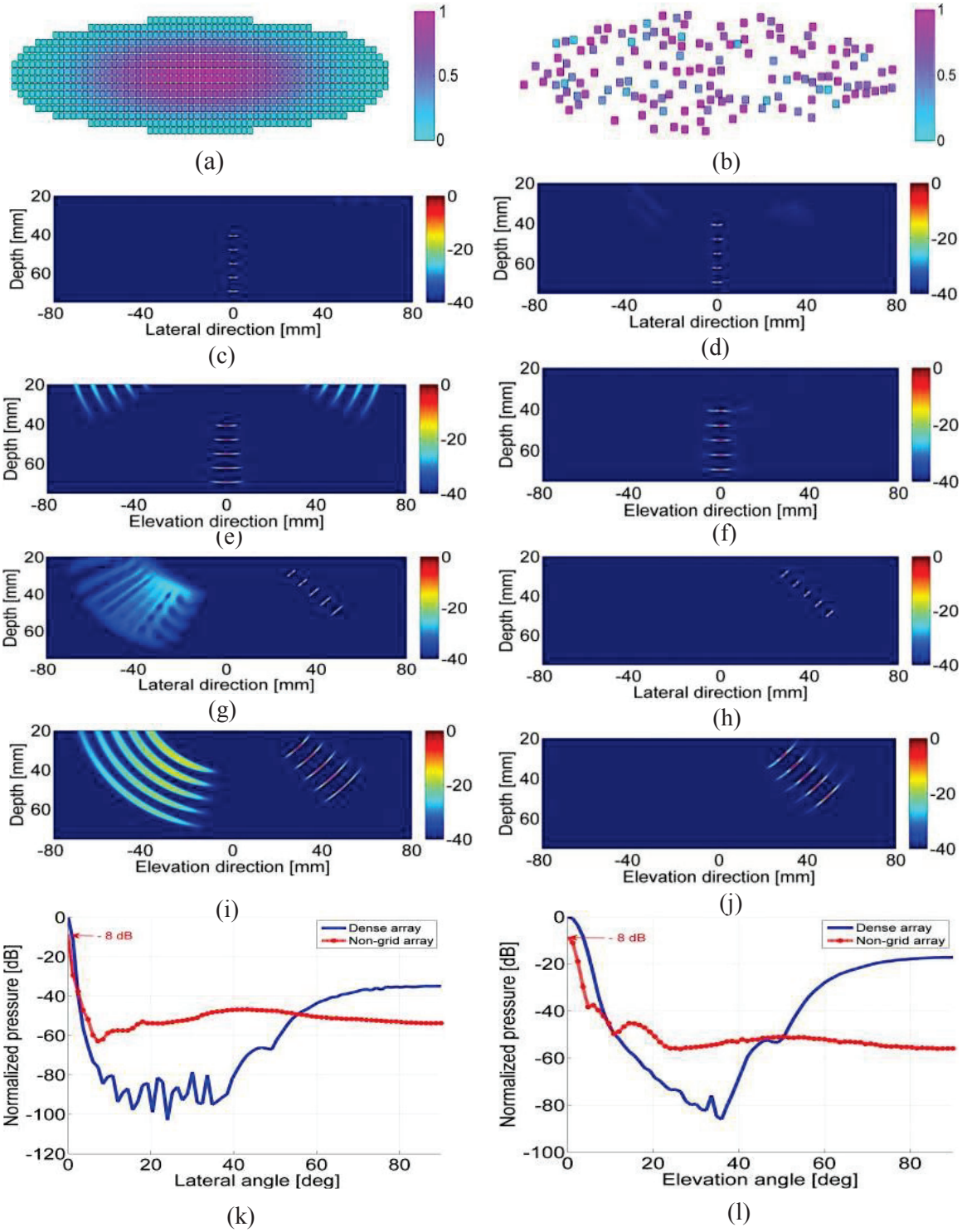

Figure 3.20: comparison between (a) the dense 64x16 array and (b) the optimized non-grid array of 142 elements, (c)-(d) and (e)-(f) are respectively the PSF in lateral and elevation direction with the two arrays when no steering is considered, (g)-(h) and (i)-(j) are the same PSF when the scatterers are placed at (45 °, 45°) off axis, (k)-(l) represent the beam profiles in lateral and elevation direction showing the energy loss caused by the element number reduction. The PSF of the non-grid array is very similar to that of the dense array but with a better grating lobes reduction capabilities in the cases of steering. The energy loss is limited by the increase of the element size and is about 8 dB against 15 dB in the standard sparse arrays.

In Figure 3.20g, performed by the dense array, the mirror images of the scatterers appear near the left-hand corner, but in the non-grid array any mark does not exist on the PSF presented in Figure 3.20h. In the elevation direction, the ratio between the main lobe and the grating is about 20 dB in the dense array against 48 dB in the non-grid array (Figure 3.20l), for that reason the PSF presents stronger mirror images (Figure 3.20i) capable of modifying the array image characteristics in a realistic imaging situation. The non-grid array, in addition to the grating lobes reduction, improves the spatial resolution in the elevation direction giving thinner scatterer points than the dense array in (Figure 3.20f-j).

After the undesired lobes suppression, an important characteristic expected from the optimized arrays is the energy level compared to the dense array. In this purpose, the beam profile of the non-grid array is normalized by that of the dense array to know exactly the energy ratio between them. Figure 3.20k-l corresponding to the beam profile in the lateral and elevation direction confirm that the energy loss is only 8 dB for an element number reduction going from 828 (dense array) to 142 (non-grid array), a reduction of 83%, in addition an improvement of the main lobe is noticed in the elevation direction leading to an better image resolution.

3.5.2.b Optimization of 0.8 λ element arrays

Evolution of element number and energy function

The same optimization process is applied to a 0.8 λ non-grid array with the same beams criteria. Such wide element cannot be used in the standard 2D array design at the risk of deteriorating the array beam features due to the grating lobes as shown in the Section 3.3.3. During the optimization, the active element number decreases sharply from the beginning to 250 iterations falling to 103 elements in Figure 3.21a. At the end of the optimization the standard deviation is less than 2 elements. Concerning the energy function, its variation follows the same dynamic as the element number with a standard deviation less than one unit (Figure 3.21b). A number iteration fewer than a thousand is largely sufficient in this case.

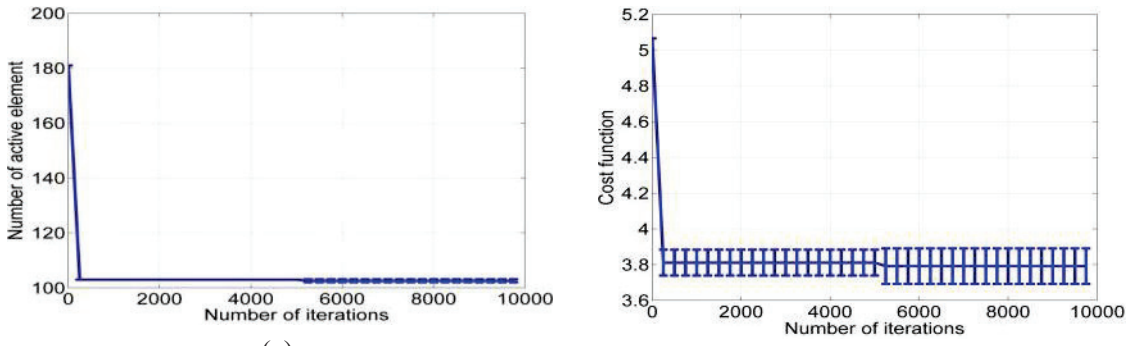

(a) (b)

Figure 3.21: the mean and standard deviation values of seven optimized non-grid array. The variation is about +/- 2 elements. The mean active element at the end of the optimization is 102 and presents only 9 dB energy loss compared to the dense array. The reduction ratio is about 88% compared to the dense array.

Comparison of the PSF of the dense and the optimized arrays

The PSF simulations are performed on the PSF phantoms in Figure 2.11a-b-c. Only the steering case is considered here as it presents the worst case of the array beam pattern. The

simulations are realized by the optimized non-grid array of 102 active elements (Figure 3.21a). The PSF of the non-grid array does not present any grating lobes neither in the lateral (Figure 3.22d) nor in the elevation directions (Figure 3.22f) contrary to that of the dense array (Figure 3.22c-e). Moreover, the elevation direction resolution is improved since a thinner main lobe is provided by the non-grid array (Figure 3.22h).

Concerning the energy loss caused by the element number reduction, it is about 9 dB with 102 active elements (88% thinning). After the main lobe zone, the optimized array beam profile presents a flat beam pattern without any undesired lobes. These non-grid arrays are controllable by current scanners. They constitute a hope for 3D ultrasound imaging.

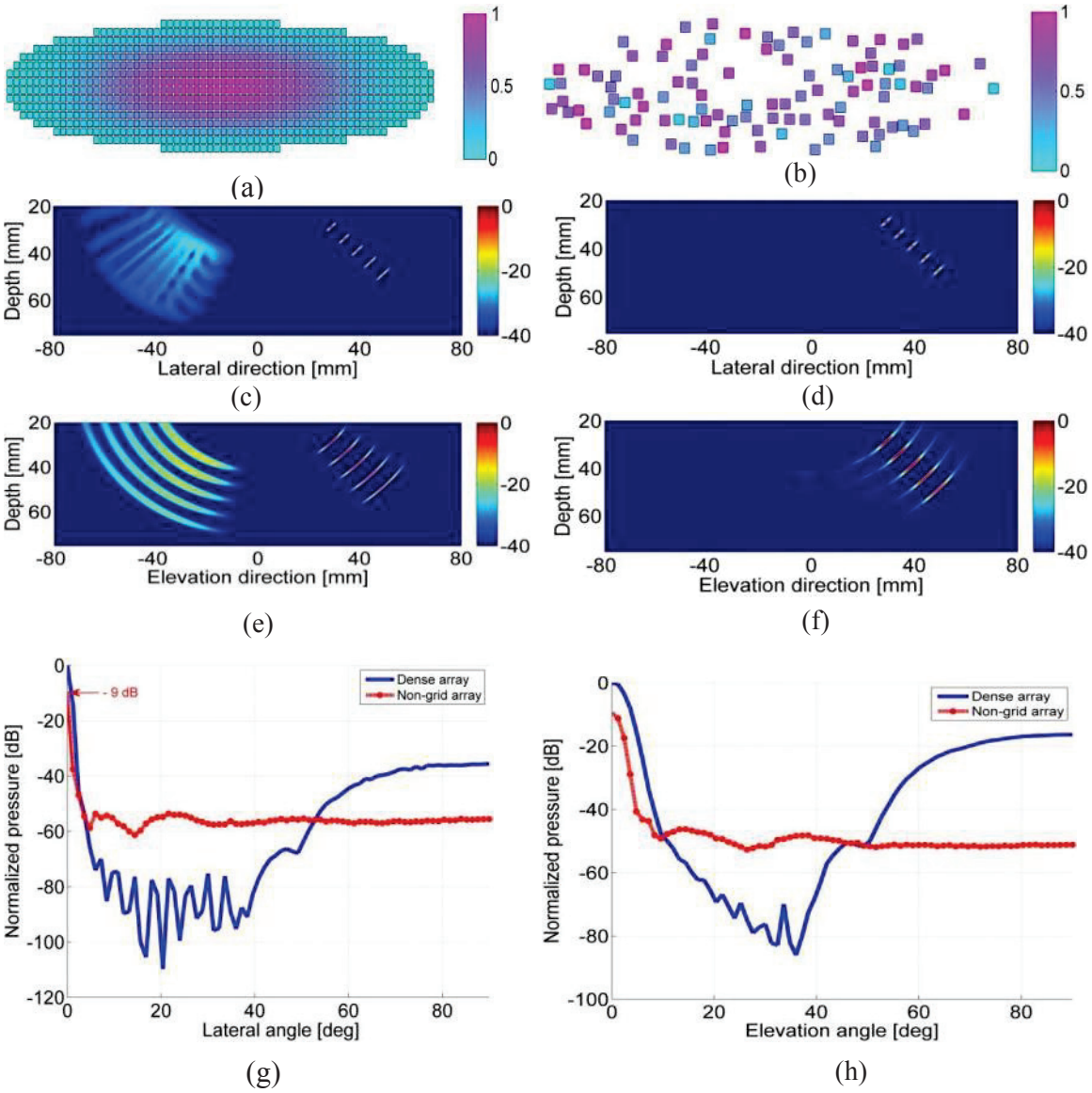

Figure 3.22: comparison between (a) the dense 64x16 array (828 elements of 0.5 λ) and (b) the optimized non-grid array of 102 elements (of 0.8 λ width), (c)-(d) and (e)-(f) are respectively the PSF in lateral and elevation direction with the two arrays when steering at (45 °, 45°) off axis. The PSF of the non-grid array is very similar to that of the dense array but with better grating lobes reduction capabilities mainly in the case of steering. The energy loss is limited by the increase of the element size and is about 9 dB against 15 dB in the standard sparse arrays.

3.5.3. Optimized variable size (non-grid) sparse array

Firstly, the variable size non-grid array is optimized to its possible low element number based on the optimization criteria defined in the standard and the non-grid sparse arrays before. The results of this optimization are compared to the dense array.

Evolution of element number

The optimization of the variable size array is performed with an iteration number of 2500, enough to reach a steady optimized element number. The lowest active element number obtained after 1200 iterations is 161. This active element number is maintained for the comparison with the dense array.

Comparison of the PSF of the dense and the optimized arrays

The comparison between the dense array (Figure 3.23a) containing 828 elements and the optimized variable size array (Figure 3.23b) with 161 elements is made using the phantoms of Figure 2.11. The comparison is about the PSF and the beam profiles. The PSF of the dense array, when any steering is involved was presented previously (Figure 3.20a-e) with important grating lobes effect while any mirror image exist on the PSF of the variable size array (Figure 3.23c-e). This efficiency of the variable size array comes from the non-grid placement conjugated to the variation of the elements size. In case of steering, the gating lobes become more important in the dense array (Figure 3.20g-i). This steering does not impact the capabilities of the variable size case for which the PSF is clean of any unwanted effect (Figure 3.23d-f). The beam profiles confirm that the grating lobes of the dense array are 35 dB and 17 dB against 42 dB and 38 dB in the variable size array in the lateral and elevation directions, respectively. In terms of energy ratio, despite the considerable elements number reduction (80%), the energy loss is about 11 dB against 15 dB in the standard sparse arrays. The variable size array is a good strategy able to include the advantages of the non-grid array and the standard regular grid. The size of the element can be chosen in a large interval based on the targeted application.

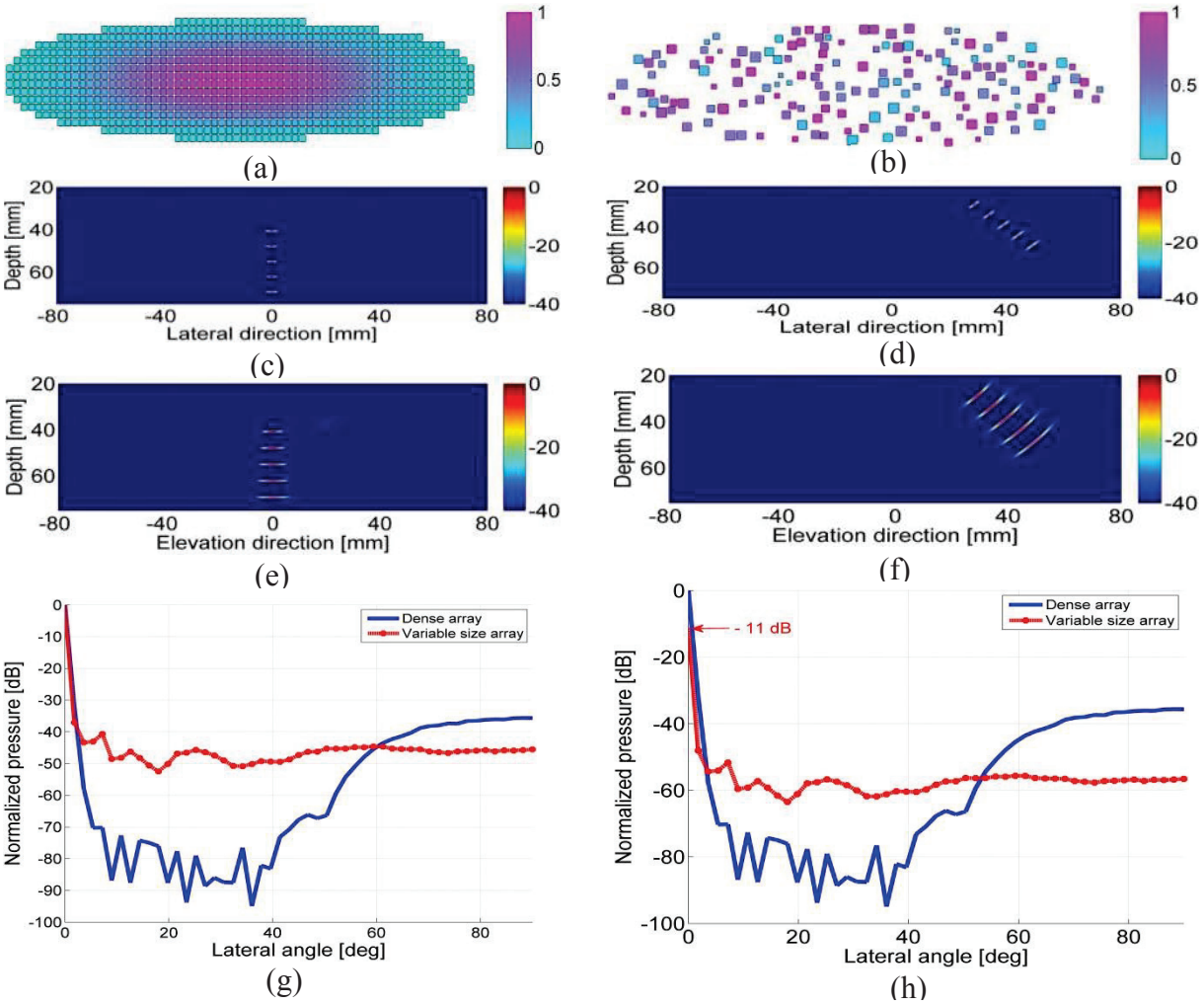

Figure 3.23: (a) the 64x16 dense array of 0.5 λ-width elements and (b) the optimized variable size array of 161 elements sized between 0.4 λ and 0.8 λ, (c)-(d) the lateral and (e)-(f) the elevation PSF without and with steering at (45°, 45°) using the variable size array. The beam profiles in (g) show the ratio between the main lobe energy and the grating lobe energy ratio in each case whereas (h) shows the energy loss compared to the dense array (11 dB).

3.5.4. Comparison between the three methods

Three element disposition techniques (the standard, non-grid and variable-size arrays) are studied in this thesis. To give an overview of all these techniques, all three are optimized at a fixed element number for comparison purposes with an iteration number of 2500. This comparison aims to evaluate their relative efficiency in terms of overall imaging capabilities: the signal-to-noise ratio (beam energy), the resolution (main lobe width) and contrast (grating lobes). The array footprint is constant and identical in all three cases.

3.5.4.a Element number fixed to 128

The arrays studied are represented in Figure 3.24 with (a) the standard sparse, (b) the non-grid sparse and (c) the variable size non-grid arrays. In the standard and the non-grid sparse arrays the element size is kept equal to a mid-wavelength ($\lambda/2$) and varies from $0.4\,\lambda$ to $0.8\,\lambda$ in the variable size array. The active surface of the latter is more important than that of the two formers which have identical surfaces. The comparison of the PSF aims at

highlighting the grating lobe reduction capability of each method and the energy ratio between the three techniques.

Comparison of the PSF

The PSF of the three configurations are compared by simulations using the phantoms presented in Figure 2.11a-b. The simulations are performed in both unsteering and steering cases. More often the scanning sector exceeds seldom 60 degrees (+/- 30°) but to really study the limits, we extend this sector to 180 degrees (+/- 90°) the maximum sector width. The transmit focus is situated at 50 mm and the multiple reception foci are set to coincide with the scatterers positions (Figure 2.11a-b). When the scatterers are on the probe axis (unsteering) the results of the standard sparse, the non-grid and the variable size arrays are displayed by Figure 3.24d-e and f respectively. The result of the standard sparse array shows important mirror images of the scatterers visible on the two upper corners of the PSF (Figure 3.24d). In the non-grid based array case presented by Figure 3.24e, the grating lobes are quasi-inexistent with just one small mirror image in the right-hand corner while in the variable size array the grating lobes are so weak that any mark can be detected on the PSF (Figure 3.24f).

In the steering case, in both the lateral and elevation directions, the grating lobes effect are more significant in the standard sparse arrays (Figure 3.24g-h) with an effect more emphatic in the elevation direction. This latter is due to the small number of elements in this direction leading to a grating lobe level about – 20 dB. The non-grid array results (Figure 3.24i-j) are clearly better than that of the standard sparse array. In the lateral direction, there is any visible effect of the grating lobes but residual marks exist in the elevation direction Figure 3.24j.

The optimal performances are provided by the variable size (non-grid) array which completely removes any grating lobes effect on the resulting PSF in both directions (Figure 3.24k-l). The efficiency of this latter technique resides in its deep randomness in both element positions and size. The beam profile shows a grating lobes below – 45 dB with a quasi-flat beam features outside the main lobe area contrary to the standard techniques Figure 3.24a.

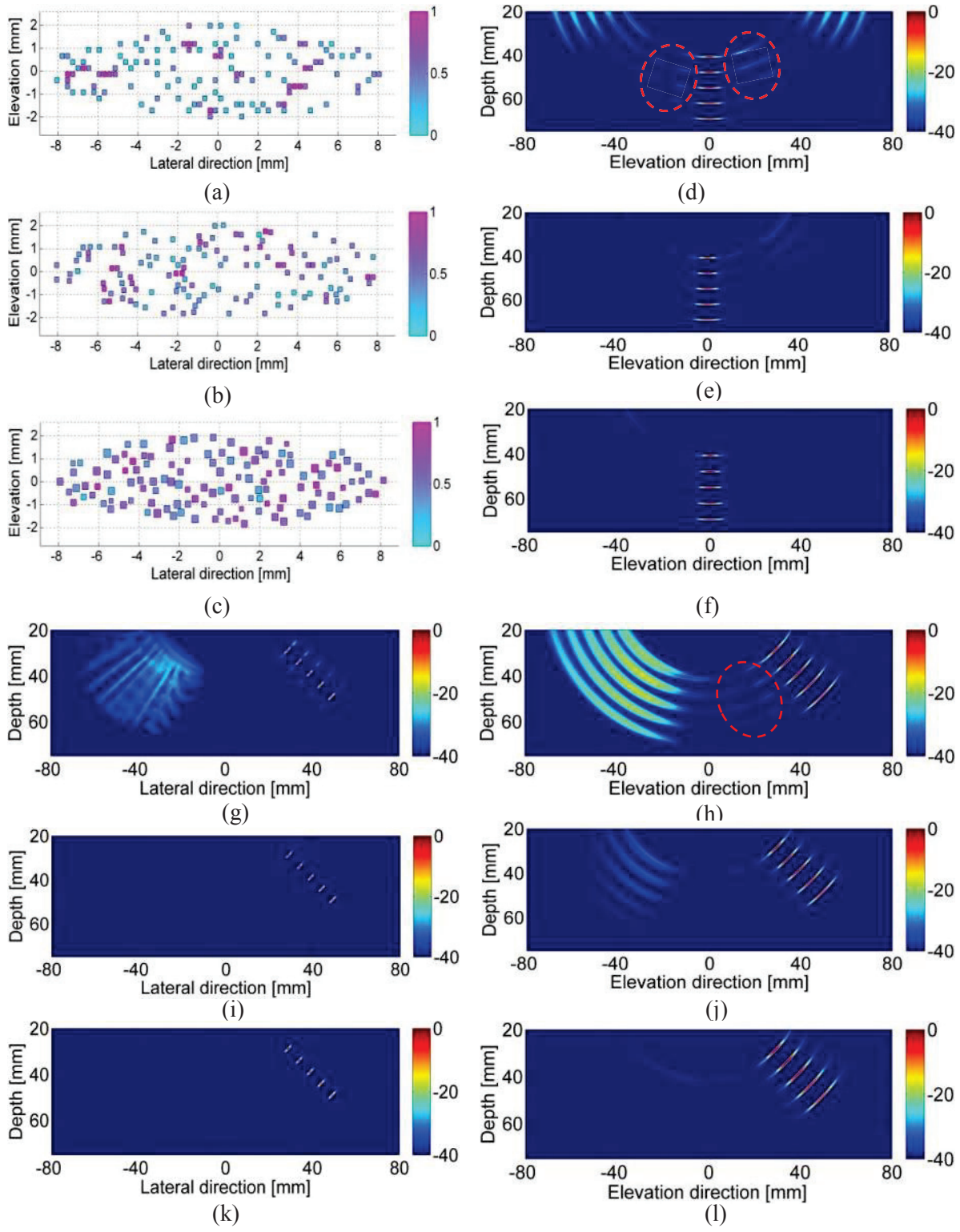

Figure 3.24: the optimized (a) standard sparse with 128 elements of 0.5 λ, (b) non-grid with 128 elements of 0.5 λ and (c) variable size arrays with 128 elements between 0.4 λ and 0.8 λ, (d)-(e)-(f) represent the elevation direction PSF without unsteering using standard, non-grid and variable size array respectively. In the steering case, the scatterer are placed at (45°, 45°) and the results in lateral and elevation direction are displayed in (g)-(h) in standard sparse, (i)-(j) the non-grid and (k)-(l) in the variable size arrays.

Comparison of beam profiles and energy ratio

The beam profiles of the three techniques are compared in terms of main and grating lobes. The main lobe width of all configurations is identical despite the use of wide elements in the variable size (Figure 3.25a). The grating lobes are respectively – 20 dB, – 40 dB and – 45 dB in the standard, the non-grid and the variable size arrays. In this optimization process the constraint was the number of active elements which is fixed and the expected sidelobe lobes level (– 40 dB). As output, the sidelobes value is about – 35 dB in the standard array against – 39 dB in the non-grid array and less than – 42 dB in the variable size array.

In terms of energy, the beams of the sparse and the non-grid arrays are all normalized by that of the variable size array. The variable size provides an energy 16 dB more important than the standard sparse array and 13 dB better than the non-grid array (Figure 3.25b). These results prove the superiority of the new approaches over the standard methods. These results will be different when wider elements are used in the non-grid array ($0.7\ \lambda$ or $0.8\ \lambda$) mainly in terms of energy. Realistic simulations are made on a cyst phantom to validate all these results obtained with the three arrays.

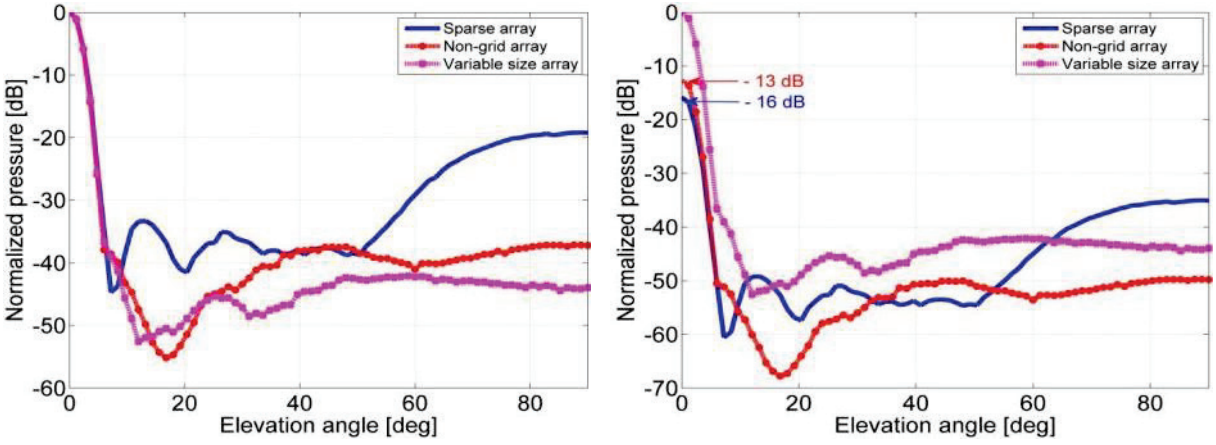

Figure 3.25: beam profiles of (a) the standard sparse, the non-grid and the variable size arrays showing the ratio between the main and the grating lobes of each method and (b) the energy ratio between the three techniques for the same number of active element of 128. The variable size array method provides a better overall sensitivity with an energy 16 dB and 13 dB greater than that of the standard sparse and the non-grid arrays, respectively. Moreover, the variable size array presents the lowest grating lobe level, 25 dB compared to the standard sparse array and 5 dB compared to the non-grid array.

3.5.4.b Element number fixed to 256

The common channel number in the most advanced ultrasound scanners today is 256. To exploit all the capability of these scanners using sparse 2D arrays, the active element number of the standard sparse array and the non-grid sparse arrays is fixed to 256 during the optimization. Their beam profiles are then compared to that of the dense array of 828 elements to evaluate their suitability to 3D ultrasound imaging. The arrays studied are represented by Figure 3.26 with (a) the dense array, (b) the standard sparse, (c) the non-grid sparse and (d) the variable size non-grid arrays. The element size is kept equal to a mid-wavelength ($\lambda/2$) in the dense and the standard sparse array, 0.7λ in the non-grid sparse array and varies from $0.6\ \lambda$ to $0.8\ \lambda$ in the variable size array. Consequently, the active surface of the non-grid arrays (Figure 3.26c-d) is more important than that of the standard sparse array even though the array footprints are the same in all cases.

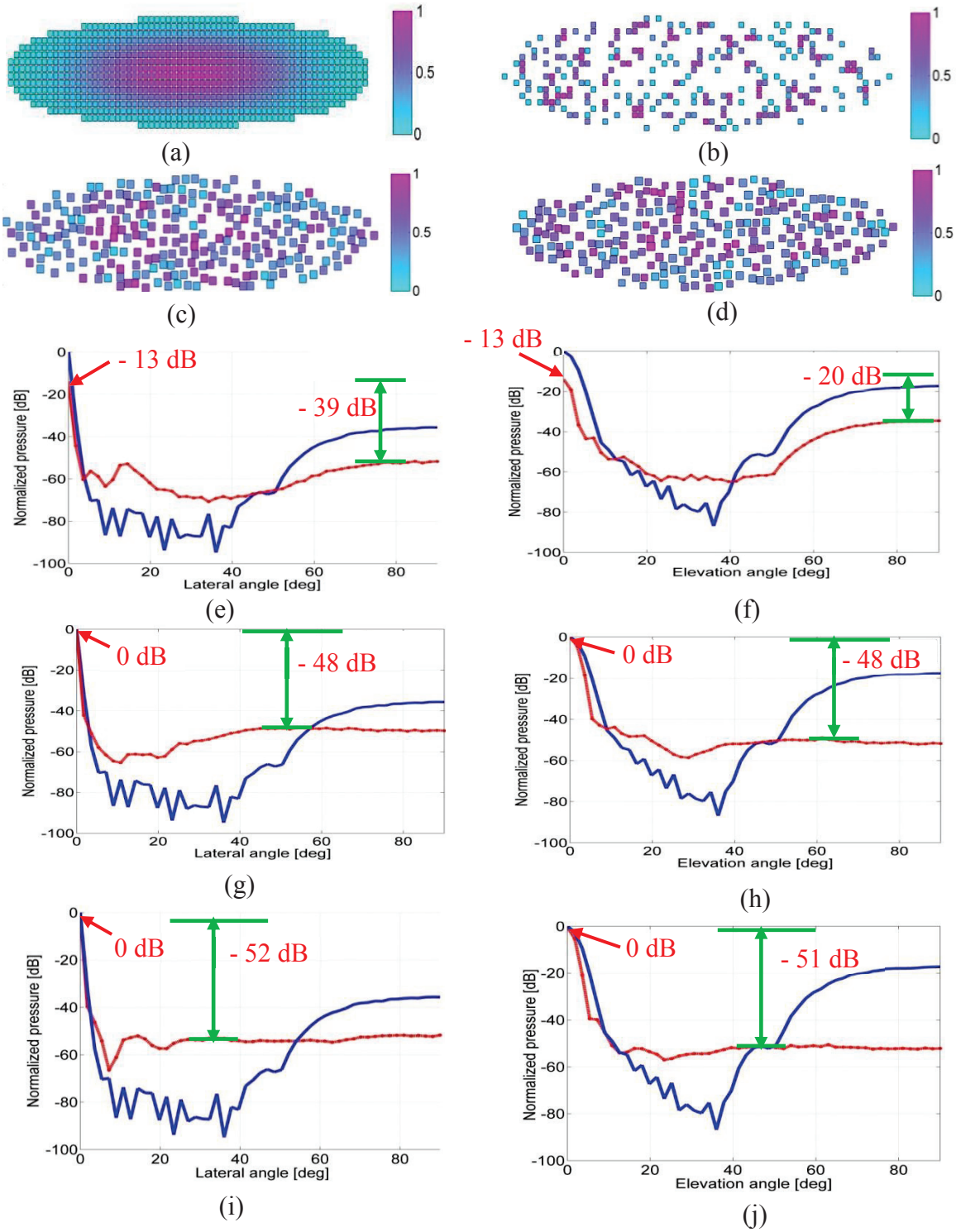

Figure 3.26: (a) the ellipsoidal part of the 64x16 2D array of 828 elements, the optimized (b) standard sparse array with 256 elements of 0.5 λ, (b) non-grid array with 256 elements of 0.7 λ and (c) variable size arrays with 256 elements between 0.6 λ and 0.8 λ . The beam profile of each array is compared to that of the dense array to evaluate the energy loss and the grating lobes due to the element number reduction. The comparison to the dense array in both lateral and elevation direction is (e)-(f) for the sparse array, (g)-(h) for the non-grid array and (i)-(j) for the variable size array. In the standard sparse array, the energy loss is about 13 dB compared to the dense array whereas it is 0 dB in the non-grid arrays. The grating lobes are -39 dB and – 20 dB in standard sparse array, – 48 dB in non-grid array and at least – 51 dB in variable size array against -36 dB and -17 dB in dense array in lateral and elevation directions respectively.

The beam profile of each optimized array is normalized by that of the dense array to evaluate the energy loss due to the element number reduction; a great importance is also attached to the grating lobe reduction capability of each array in relation to the dense array. In the standard sparse array, the energy loss is about – 13 dB compared to the dense array and the grating lobes are slightly more reduced with –39 dB against – 36 dB in lateral direction (Figure 3.26e) and –20 dB against –17 dB in the elevation direction (Figure 3.26f). Using the non-grid and the variable-size arrays, the energy loss is completely compensated and the grating lobes are drastically reduced (Figure 3.26g to j). With the non-grid array, the grating lobes are 12 dB (– 48 dB against –36 dB) and 31 dB (– 48 dB against – 17 dB) lower compared to the dense array in lateral and elevation directions respectively (Figure 3.26g-h). In the variable-size array, thanks to the randomness of the element size, the grating lobes reduction goes from 16 dB (– 52 dB against –36 dB) in lateral direction to 34 dB (–51 dB against –17 dB) in elevation direction compared to those of the dense array (Figure 3.26i-j). These results show the potential of optimized arrays in terms of real-time 3D ultrasound imaging using few active elements within the 2D matrix arrays without any deterioration of their beam properties. The methods developed are independent from the array dimensions as presented in [B. Diarra et al. (2013)].

3.6. Phantom simulations

In this section, the different optimized arrays of the standard, the non-grid and the variable size arrays are tested in realistic phantom simulations. The dense array is always the reference array except in the variable array‘s case. In the latter a direct comparison is made between the three optimized arrays when the active element number is fixed.

3.6.1. Comparison of the dense and standard sparse arrays

The first simulation compares the non-grid array technique to the standard sparse array. The main expected improvement from the non-grid method is a considerable reduction of the image noise (grating lobes) which translates in an increase in image contrast and the use of wide element maximizes the probe’s active surface leading to a better sensitivity (more energy). In the standard sparse array, the element reduction efficiency is an interesting property but, because of its important energy loss, the sparse array remains most of the time a theoretical approach not exploited in practice. In the first example, the same number of active elements is used in both standard and non-grid sparse arrays but with different size. The squared element size is 0.5 λ in dense and sparse array to limit the grating lobe whereas their size is 0.8 λ in the non-grid array (larger element size can be used to more maximize the probe sensibility).

3.6.1.a Cyst phantom

The cyst phantom is a 60×10×60 mm^3 numerical phantom. There are five anechoic cysts (empty of scatterers) aligned at different depths and parallel to five hyper-echoic inclusions (mean scattering amplitude ten times higher than the background amplitude). The cysts have a spherical shape with their diameter ranging from 2 to 6 mm. Five hyper-echoic point scatterers are also placed at −20 mm in the lateral direction. In this case, the simulations were performed using the same number of active elements (177) for both the standard and non-grid sparse arrays. The TX focus is at 60 mm and the foci in reception are located at 30, 50, 70, and 90 mm. Figure 3.27 displays the simulation results for (a) the dense array, (b) the

standard sparse array, and (c) the non-grid array. The B-mode images are shown together with the profiles at a 60-mm depth. All data are normalized to the peak echo value in the profile obtained using the dense array.

Using the non-grid array, the energy loss is about −5 dB compared to the dense array, whereas it is about −18 dB in the standard sparse array. The difference between the background and the hyper-echoic cyst (at a 60-mm depth) is 20 dB for the dense array, 21 dB for the standard sparse array, and 23 dB for the non-grid sparse array. This contrast improvement can be explained by the lower grating-lobe level of the non-grid sparse array.

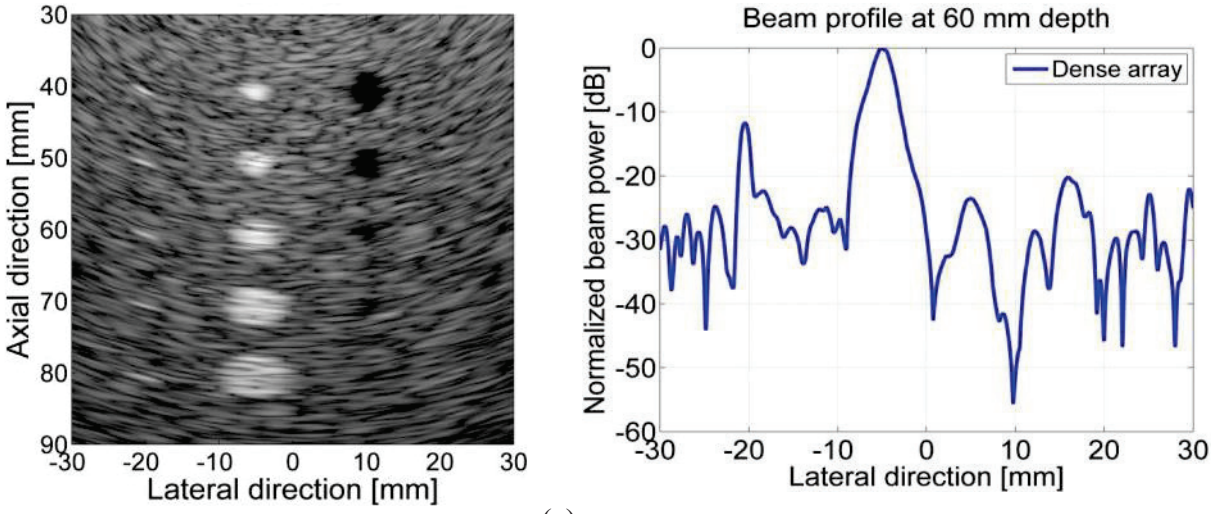

(a)

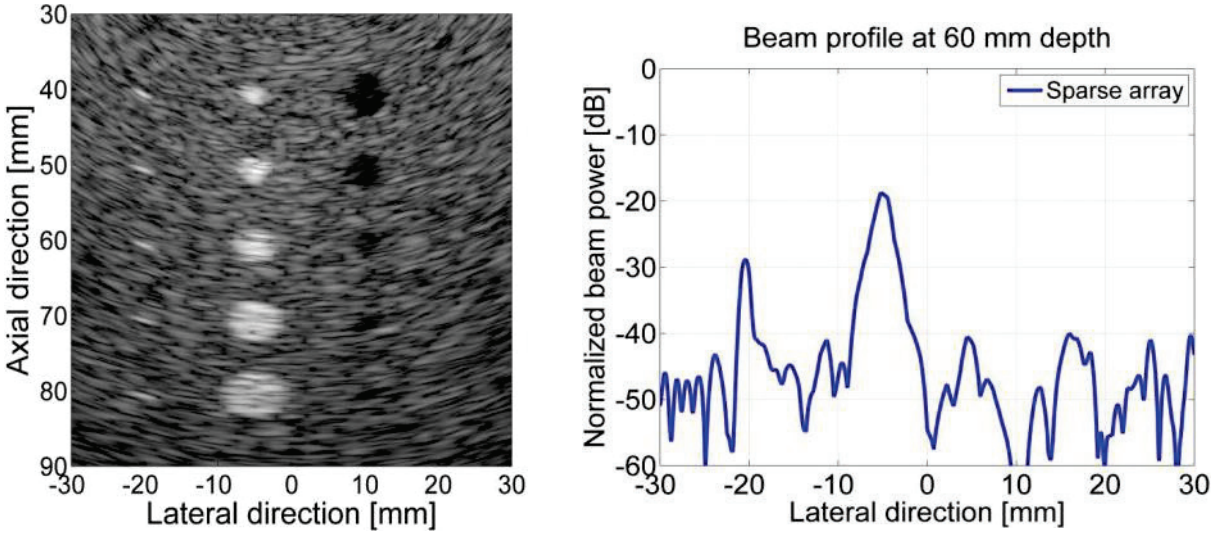

(b)

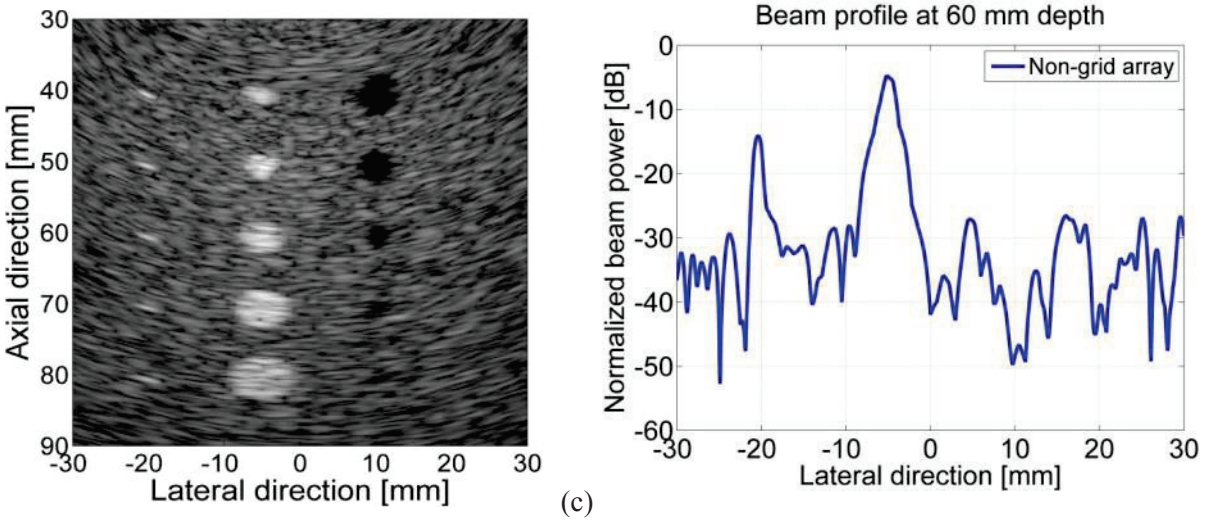

(c)

Figure 3.27: Imaging of a cyst phantom: frames and 60-mm-depth profiles obtained with (a) the 64×16 dense array, (b) the optimized standard sparse array with 177 elements, and (c) the optimized non-grid sparse array with 177 elements.

3.6.1.b Needle phantom

The second numerical phantom is a 50×50×30-mm^3 tissue volume in which a needle is inserted. The homogeneous tissue region is filled with scatterers whose positions are randomly sampled and whose strengths follow a Gaussian distribution. The needle is cylindrical, 20 mm long with a 0.3-mm radius, characterized by a scatterer concentration 50 times higher than that of the tissue. The TX focus is at 60 mm and the foci in reception are located at 35, 45, 55 and 65 mm. The images obtained with the dense, standard sparse, and non-grid sparse arrays described in the previous section are shown in Figure 3.28 together with a reference A-line intersecting the needle. All data are normalized to the peak echo value obtained from the needle using the dense array. Compared to the dense array, the energy loss is about −18 dB for both the non-grid and standard sparse arrays. The needle echo is 26 dB higher than tissue for the dense array and 25 dB higher for both the non-grid and standard sparse arrays.

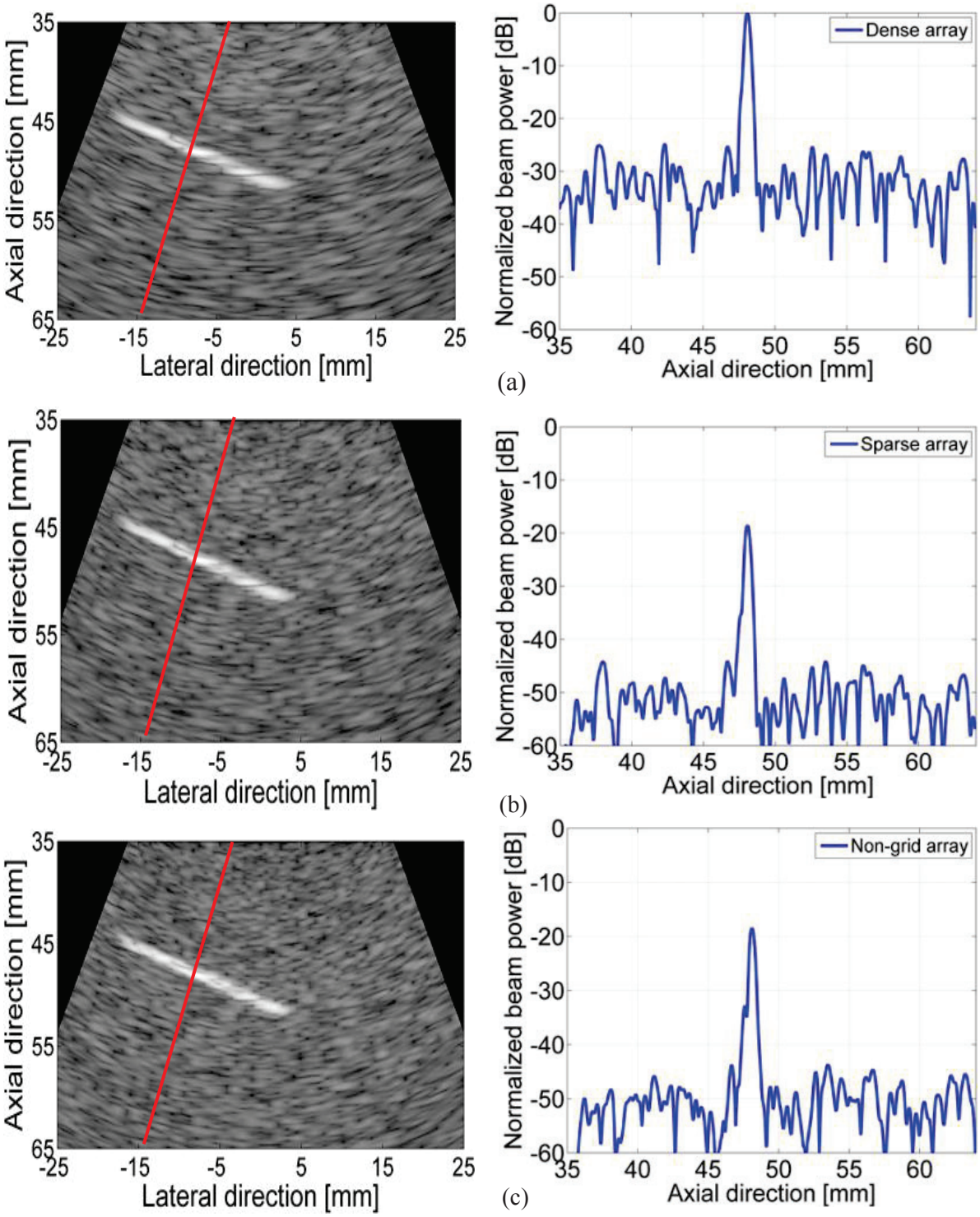

Figure 3.28: Imaging of a numerical phantom (needle inserted in an homogeneous tissue volume): frames and A-lines obtained with (a) the 64×16 dense array, (b) the optimized standard sparse array with 177 elements, and (c) the optimized non-grid sparse array with 101 elements.

3.6.2. Simulation of the variable size non-grid array

3.6.2.a Cyst phantom

The phantom used in the simulations to compare the optimized sparse, non-grid and variable size arrays is a General Purpose Ultrasound phantom of the Model 054GS (Figure 3.29a) manufactured by the society CIRS and containing wires and different echogenicity inclusions [Rachedine and Zerhouni (1993)]. Its dimensions are 18x16x10 cm^3 (depth x width x height). All gray scale inclusions have a diameter of 8 mm, the horizontal and vertical targets are 0.1 mm-diameter points spaced of 2 cm. The resolution targets have a diameter of 0.8 mm and those of the near-field are placed from 1 to 6 mm with a radius of 0.1 mm. For the simulations the penetration depth is fixed to 10 cm, thus the theoretical phantom containing 500 thousand scatterers has a dimension of 10 x16 x 10 cm^3. Figure 3.29b shows only the part of the phantom chosen in these simulations going from 0 to 10 cm depth. The size of the wires was kept identical to 0.8 mm in the simulations to be able to see them correctly in all the depth range.

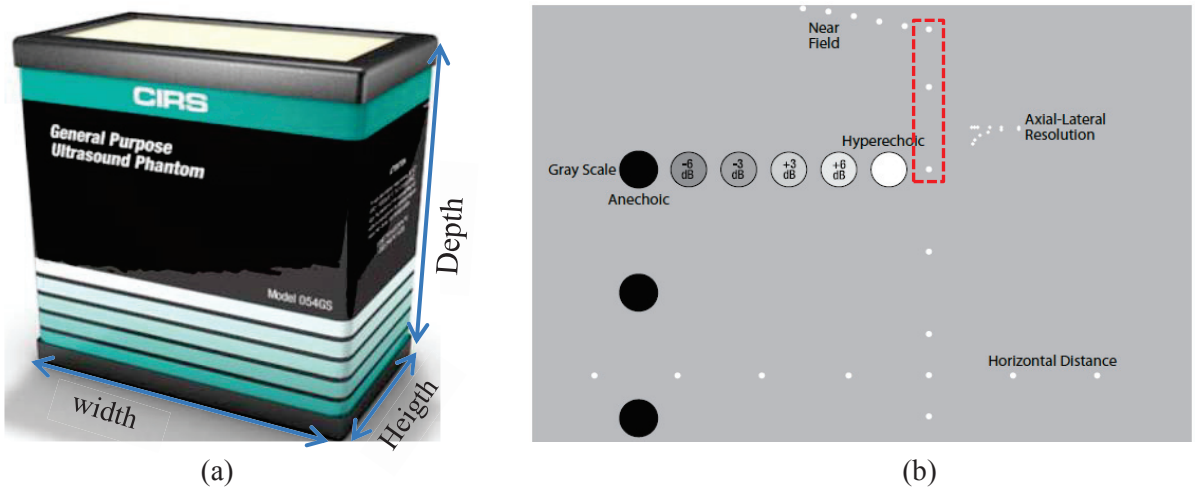

(a) (b)

Figure 3.29: the experimental phantom (a) its dimensions and (b) its internal characteristics. Information from the website of CIRS (http://www.cirsinc.com/products/all/80/general-purpose-ultrasound-phantom/).

3.6.2.b Simulation results

The simulations are realized on the phantom presented in Figure 3.29. The images confirm the better signal-to-noise ratio of the variable size array compared to both sparse and non-grid array. An A-line is selected to emphasize the amplitude ratio shown before in Figure 3.28. The overall image quality is improved decreasing more the grating lobes as shown by Figure 3.30 The image of Figure 3.30a obtained by the standard sparse array allows observing all the wires and cysts in the phantom but the near-field wires presents a worse contrast compared to the non-grid arrays (Figure 3.30b). The best contrast is provided by the variable size array with any noticeable undesirable effect on the whole simulated image Figure 3.30c.

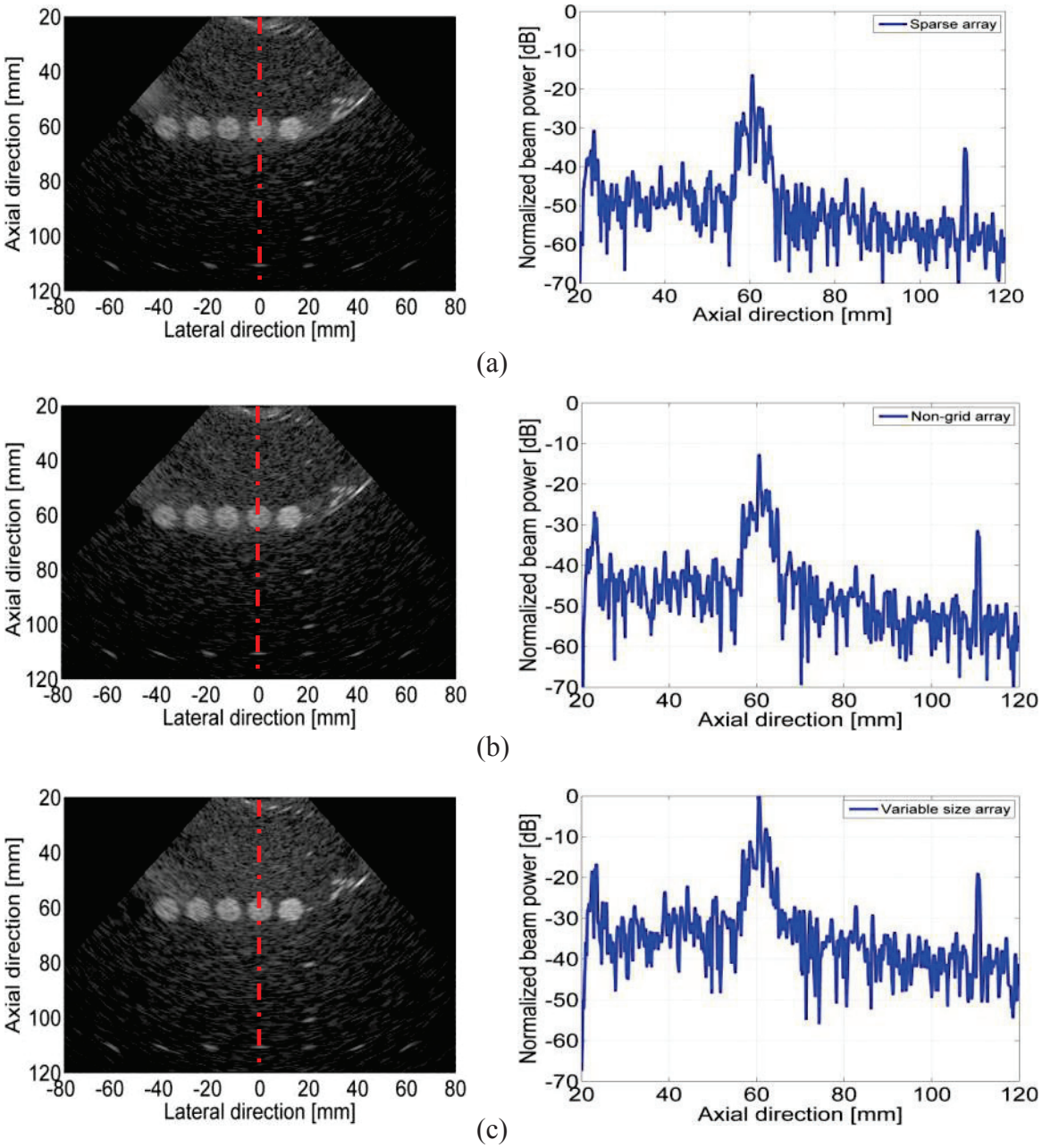

Figure 3.30: the cyst phantom simulations and the energy ratio using the optimized (a) standard sparse, (b) non-grid and (c) variable size arrays for the same number of active element of 128. The variable size array permits to obtain an energy 16 dB and 13 dB better than the standard sparse and the non-grid array respectively.

3.7. Summary of optimized arrays

The beam characteristics of the dense and the optimized arrays are summarized in Table 3.3. The number of active elements, the grating lobes and the energy are compared to those of the dense array to emphasize the potentiality of each array configuration. The non-grid array permits to reduce the active element till 102 elements with better energy conservation against 170 elements in the standard sparse array with an important energy loss. For big arrays such as a 64x64 array the difference between the energy of the standard and non-grid sparse arrays can exceed several tens of dB [B. Diarra et al. (2013)].

		Dense array	Standard sparse array	Non-grid sparse array		Variable size array
		64x16	64x16	64x16		64x16
Number of elements		828	170	142	102	161
Element size		$\lambda/2$	$\lambda/2$	$7\lambda/10$	$4\lambda/5$	$2\lambda/5 - 4\lambda/5$
Lateral / Elevation main lobe width at −6 dB (degree)		0.7 / 6	0.6 / 4.6	0.6/ 3.7	0.6 / 3.9	0.6/4
Lateral/ Elevation grating-lobe (dB)	On-axis	−35.6/−17.3	−38.6 / −19.2	−40.9/ −40	−40.1/ −39	−42/−41
	Off-axis(Steering)	−27.8/−16.3	−28.5 / −21	−38.2/ −33.8	−38 / −30.2	−42/−38
Energy (dB)		0	− 15	− 8	− 9	− 11
Active surface (mm²)		49.5	8.2	13.5	12.6	11.5

Table 3.3: the comparison of the standard ,the non-grid and the variable size arrays to the 64x16 dense array. The grating lobes, the main lobe and the energy ratios between each sparse array are mentionned. The non-grid array give the best configuration in terms of energy and active element whereas the variable size array presents the lowest grating lobes.

The optimization when the active element number is fixed to 256 shows the superiority of the non-grid and the variable size arrays proposed in this study over the standard sparse array. With only 256 active elements (about 70% reduction), the same energy is transmitted as in the dense array containing 828 elements whereas a loss of 13 dB is noticed with the standard sparse array (Table 3.4). In addition the grating lobes are suppressed as they remain at least 40 dB lower than the main lobe energy in the two non-grid arrays.

	Dense array	Standard sparse array	Non-grid sparse array	Variable-size array
Number of elements	828	256	256	256
Element size	λ/2	λ/2	7λ/10	3λ/5- 4λ/5
Lateral / Elevation main lobe width at −6 dB (degree)	0.7 / 6	0.6 / 4.6	0.6/ 3.7	0.6/ 3.8
Lateral/ Elevation grating-lobe level (dB)	−35.6/−17.3	−39 / −20	−48/ −48	−52/ −51
Energy (dB)	0	−13	0	0
Active surface (mm²)	49.5	12.4	26	25

Table 3.4: the comparison of the standard, the non-grid and the variable size arrays to the 64x16 dense array when each array is optimized to 256 active elements. The grating lobes, the main lobe and the energy ratios between each sparse array are mentionned. The non-grid and the variable-size arrays give the same property in terms of energy whereas the variable size array presents the lowest grating lobes.

3.8. Conclusion

In conclusion, the extension of the optimization algorithm based on the simulated annealing allows obtaining at least the same thinning level as the reference methods available in the literature. The beam profile well fulfills the expected beam features. The new element positioning strategies permit obtaining a grating lobe reduction from 5 dB to 20 dB compared to the classical methods used currently. When the number of the active elements is fixed to 256, the energy loss compared to the initial dense array can be completely compensated and the grating lobe reduction goes from 9 dB to 31 dB in lateral and elevation direction

respectively. These new strategies allow the use of wide elements leading to a significant improvement of the sensitivity of the arrays (better signal-to-noise ratio) and an intrinsic active element number reduction for a given array footprint. The increase of the element size, even slightly, provides a resolution improvement by giving sharper main lobes. In applications needing a large directivity, both wide and small elements can be put together to keep the advantage of both sensitivity and directivity. The simulations on phantoms confirm the results obtained by the PSF.

The technological realization of the proposed technique seems more difficult than regular grid based array used nowadays. But discussion with many manufacturers confirms the feasibility of these arrays even with the piezoelectric elements [Fleury (2013)] and no problems exist in the CMUT elements case.

In the next chapter, the measurement results performed by the 8x8 sub-array of 8x24 2D array prototype manufactured during this study are exposed. The measurements aimed at validating the optimized sparse array techniques proposed in the previous chapter.

Chapter 4

Experiments

After the theoretical studies of the acoustical beam properties of the 2D arrays, this chapter presents a short experimental investigation of the proposed techniques with two small prototype probes. The first prototype is an 8x8 2D array available in MSDLab (Florence) and the second, an 8x24 2D array, has been manufactured by Vermon (Tours) for CREATIS (Lyon). The Ula-OP [Tortoli et al. (2009), Boni et al. (2012)] scanner used in these measurements is described, the beam profiles and the imaging capabilities of the two probes are presented with the comparison between the measurements and simulations in the 8x24 2D array case.

4.1. Introduction

The characteristics of the two prototype probes are summarized in the Table 4.1. The 8x24 array probe was realized based on bibliography and simulation results. Two configurations of the 8x24 array are considered in the optimization: (a) the full array with the 192 elements and (b) the central 8x8 sub-array of 64 elements. The measurements are realized only with the 8x8 sub-array and its corresponding optimized sparse arrays as the scanner can control at most 64 elements simultaneously.

The objective is to validate experimentally the optimization algorithm developed in the previous chapter by comparing the results obtained in the measurement to those of the simulations. The phantom considered for this validation is the cyst phantom described in the Section 3.6.2.a and represented by Figure 3.29.

In the volume scanning, both the rotational and the pyramidal acquisition techniques (Figure 2.4) are tested. The rotational acquisition is used to show simultaneously perpendicular planes while the pyramidal acquisition permits to fix the maximum number of parallel planes that can be acquired in the elevation direction without much image quality deterioration. This latter technique gives an idea on the size of volumes that can be acquired by the array.

4.2. The ULA-OP scanner

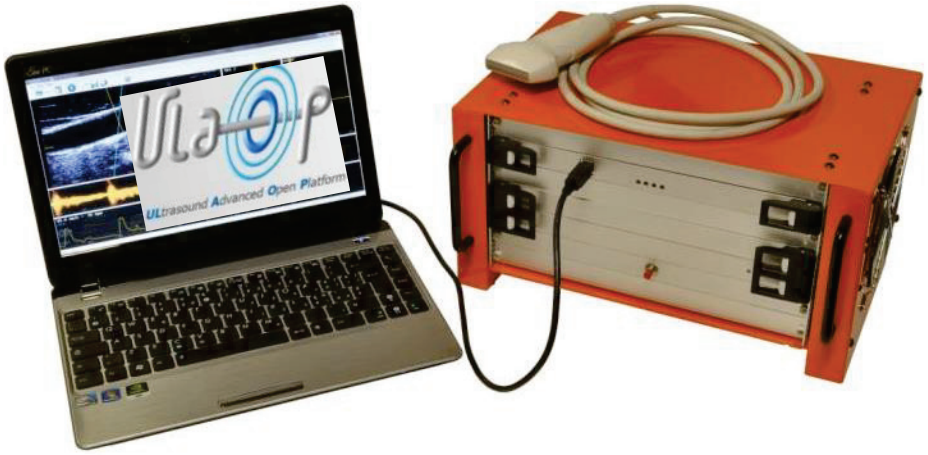

Figure 4.1: the Ula-Op scanner system used in the experimental measurements

The innovative ultrasound scanner used in the experiments is conceived in the MSDLab laboratory of Florence, Italy. This scanner can connect at most 64 elements simultaneously in its current version and this number can reach 192 by using a multiplexing system. This scanner has the particularity to be completely open and adaptable to the user's own configurations. The transmit and receive signal for each single element of an array can be set different and in the same manner small 2D arrays can be controlled fully or randomly filled. In this study the sparse array technique is optimized by the simulated annealing algorithm to find the best coefficient and position for the active elements. By default the Ula-OP is not conceived for volume imaging but by modifying the software, this imaging modality becomes possible even though the display of volume images is not possible. For 3D imaging, the possibility offered currently is the visualization of the individual slices composing a volume in real-time. The Ula-Op has a sampling frequency in transmission of 600 MHz and 50 MHz in reception.

Parameters	Probes	
	MSDLab	Vermon
Central frequency	2 MHz	3.9 MHz
Wavelength	0.77 mm	0.39 mm
Element number	8x8=64	8x24=192
Element dimensions (width and height)	1.2x1.2 mm²	0.37x0.37 mm²
Array active surface	92.16 mm^2	26.28 mm^2
Pitch	1.4 mm	0.4 mm

Table 4.1 : the characteristics of 8x8 probe of MSDLab and the 24x8 probe of Vermon

4.3. 8x8 2D array of MSDLab

This prototype probe constitutes a beginning in the 2D array experimental study. It permitted to test the adaptation of the Ula-OP software to the 3D imaging.

4.3.1. Probe beam profile

According to the theoretical expression of equation (2.12) the beam pattern of the 8x8 probe is subject to important grating lobes and does not permit a good imaging quality for large sectors as the pitch (1.4 mm) is much larger than the mid-wavelength (0.385 mm). The grating lobes exist in lateral, elevation and also in the diagonal directions. In small arrays (like 8x8), all these grating lobes have about the same amplitude as shown by the c-scan plane (Figure 4.2a). The ratio between the main lobe and that of the grating lobes energy is less than 10 dB (Figure 4.2b) which limits considerably the imaging capability of this probe. The beam profile in lateral direction (the same in the elevation by symmetry) presents the grating lobes around 25°. The reference PSF phantoms presented Figure 2.11 are used in the simulations. The PSF shows the scatterers and their mirror images coming from the grating lobes in both unsteering (Figure 4.2c) and steering (Figure 4.2d) cases. To realize an image with less effect of these lobes, the sector must not exceed 40° (from -20° to 20°). This PSF gives an idea of the results obtainable in the practice case.

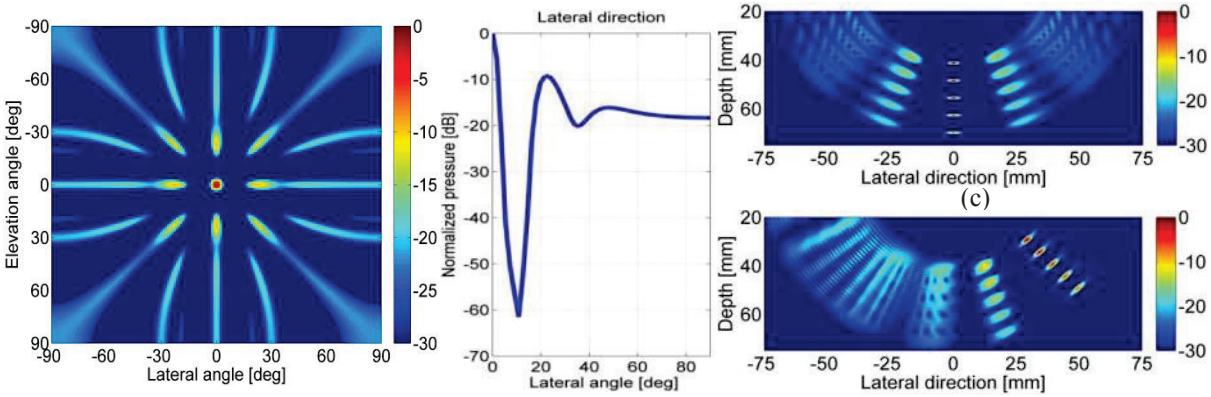

Figure 4.2 : beam pattern of the 8x8 array probe (a) c-scan plane at 50 mm, (b) and beam profile and (c) - (d) PSF in unsteering and steering cases, respectively. The ratio between the main lobe and the grating lobes is less than 10 dB (b). The PSF shows the effect of the grating lobes which can deteriorate the probe practical imaging features.

4.3.2. Imaging capabilities

The measurements with the 8x8 array of MSDLab are made on a Gammex 404GS phantom containing anechoic and hyperechoic cysts and 0.1 mm nylon fibers (Figure 4.3a). The fibers are separated by a distance of 5 mm and go from 1 to 9 cm in vertical direction; they are separated by 10 mm and situated at 5 cm depth in the horizontal direction (Figure 4.3). The objective is to determine the probe imaging capability as a function of the depth in both lateral and elevation directions.

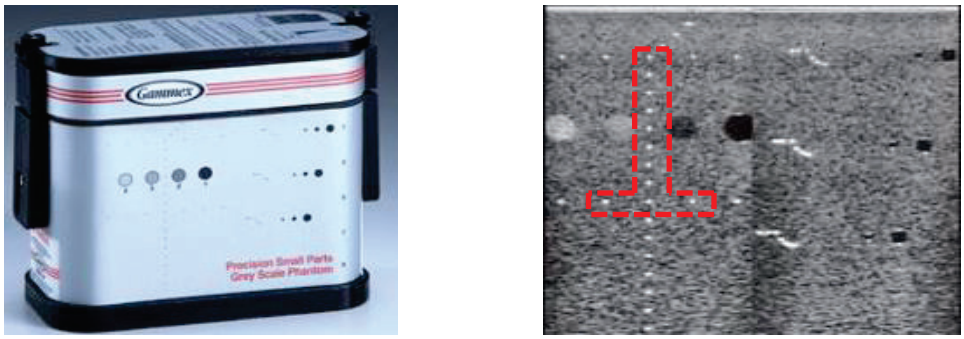

(a) (b)

Figure 4.3: (a) the cyst and nylon fibers phantom from Gammex and (b) its components (from the website http://www.physics.uk.com/Ultrasound.html). The vertical fibers go from 1 to 9 cm by a step of 5 mm and the horizontal ones situated at 1 and 5 cm depth going from 5 mm to 45 mm.

4.3.2.a Pyramidal volume scanning

The first experiment is about the possibility of doing several planes together in the elevation direction to make a volume imaging (pyramidal scanning). The focalization point is fixed at 40 mm depth and the sector angle value is 40 degrees. The number of lines per image is 64 in the lateral direction and 8 in the elevation one (memory limitation of the scanner). The images in Figure 4.4 represent seven planes with the six outer planes symmetrical in twos around the central one (largest one). Each plane permits to see the fibers included in the phantom. The image resolution worsens from the center to the outer planes as the probe energy decreases. For a number of planes much important, in addition to the energy loss the effect of the grating lobes gets important and it becomes very difficult to obtain realistic images.

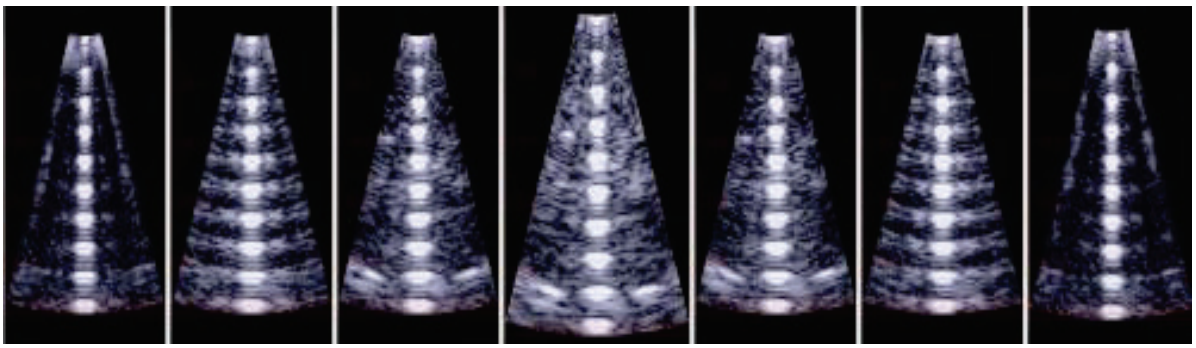

Figure 4.4 : pyramidal scanning of seven planes in the elevation direction, the outer planes are symmetrical around the center one with the same angle step. The image resolution worsens from the center to the outer because of the energy loss.

4.3.2.b Rotational volume scanning

This second mode of 3D image generation is the rotational volume imaging. In this scanning strategy, the planes of the volume rotate around the probe center. This configuration permits to see simultaneously perpendicular planes choosing an angle step of 90 degrees between the two planes. Figure 4.5a-b show the cysts and Figure 4.5c-d the fibers in the lateral and the elevation directions. This type of imaging is suitable for surgical tool tracking as all the planes might pass through the tool and the c-scan plane visualization is optimal. For general 3D imaging, this technique provides a more realistic reconstruction of the volume. These results confirm the capability of 3D using small 2D array within a limited space.

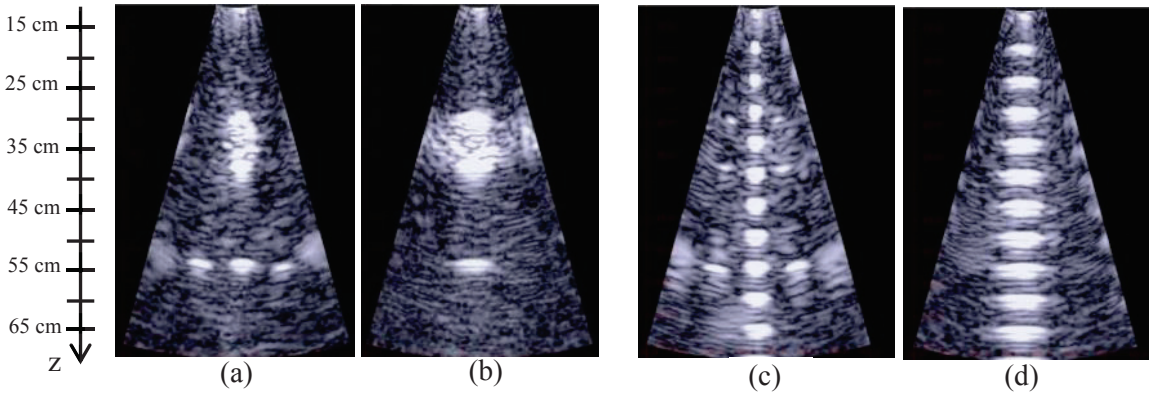

Figure 4.5 : simultaneous visualization of perpendicular planes of the cysts (a)-(b) and nylon fibers (c)-(d) in the lateral and the elevation directions, respectively. The size of the cysts and the wires are different in the directions.

4.3.2.c Grating lobes effect

If the sector scanned is larger than 40 degrees or if the fibers are not on the probe's axis, the mirror image phenomenon is observed confirming the results of the PSF simulations in Figure 4.2d. The images show the limitations of the classical element disposition technique and the necessity of respecting the spatial sampling condition at the expense of the probe capabilities reduction. The group of real fibers is displayed by the main lobe and the copy images come from the grating lobes in both directions (Figure 4.6a-b). These results match better to the theoretical PSF of this probe given by the Figure 4.2.

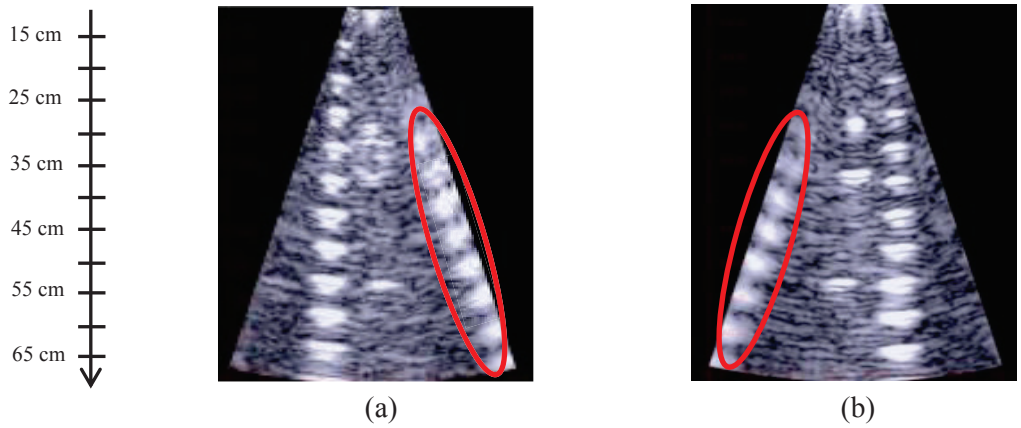

Figure 4.6 : illustration of the grating lobes apparition in (a) the lateral and (b) the elevation directions when the wires are out of the probe axis. The mirror images (surrounded by ellipsoids) are important and constitute a considerable noise source on the array images.

4.4. 8x24 2D array

The 8x24 array, designed according to the theoretical studies, is used to validate the proposed optimization technique. The characterization of the probe is made by exciting it by a three-cycle pulse (Figure 4.7a), the FFT permits to obtain the spectrum of the probe (Figure 4.7b). Figure 4.7c gives the values of the central frequency at different power level and the impulse duration.

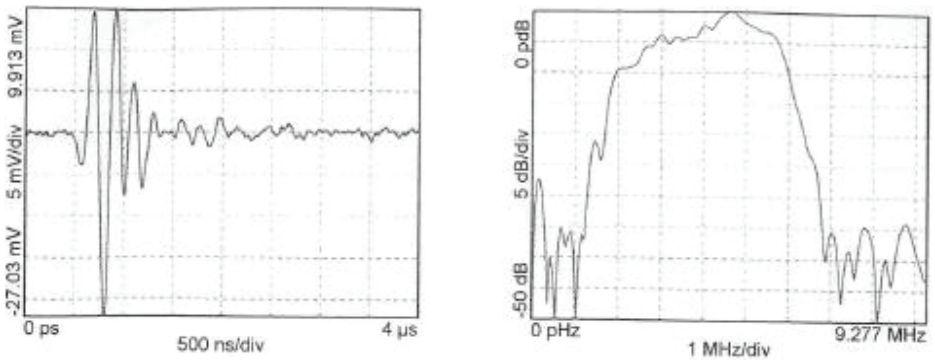

(a) (b)

	-3 dB	-6 dB	-10 dB	-20 dB
Center Frequency	4.09 MHz	3.85 MHz	3.71 MHz	4.20 MHz
Pulse duration	241.8 ns	361.4 ns	476.92 ns	1.21 µs
Bw/Fc	36.9 %	65.1 %	88.2 %	120.4 %

(c)

Figure 4.7: the probe characteristics given by the manufacturer Vermon (a) the impulse response, (b) its Fourier transform enable to determine center frequency as well as bandwidth and (c) the important points of the spectrum.

The central frequency at -6 dB is about 3.9 MHz, this value is used in both the simulations and measurements and the bandwidth goes from 3 to 4 MHz. The geometrical parameters of the probe are listed in Table 4.1. Five elements (element n° 26, 27, 28, 166 and 167) are out of order and the other 187 worked correctly. The sensitivity of individual element varies in a ratio from 0 to 4 dB. The phantoms of Figure 2.11 are used for the PSF and beam profiles simulations in a scanning sector between -90° to 90°.

4.4.1. Probe beam profile

The theoretical beam profile of the 8x24 array presents fewer and better separated (from the main lobe) grating lobes than the 8x8 array but its main lobe is larger due to its small size (Figure 4.8). The PSF is simulated using the phantoms presented by Figure 2.11. In unsteering case, the grating lobes effect is less important in the lateral direction (Figure 4.8b) than that in the elevation direction (Figure 4.8c) due to the probe dimension. In the steering case the same observation is noticed (Figure 4.8d-e). The beam profiles show a significant difference between the energy of grating lobes in the lateral (Figure 4.8f) and the elevation directions (Figure 4.8g): 10 dB against 20 dB, respectively.

These beam properties of the 8x24 2D arrays emphasize the fact that if the sector is narrow, the effect of the grating lobes is less visible even though some echoes may come back to the array. These echoes reduce the image quality in term of signal-to-noise ratio. The maximum acceptable scan sector with the probe is about 60 degrees (from -30 to 30°) according to the PSF simulations.

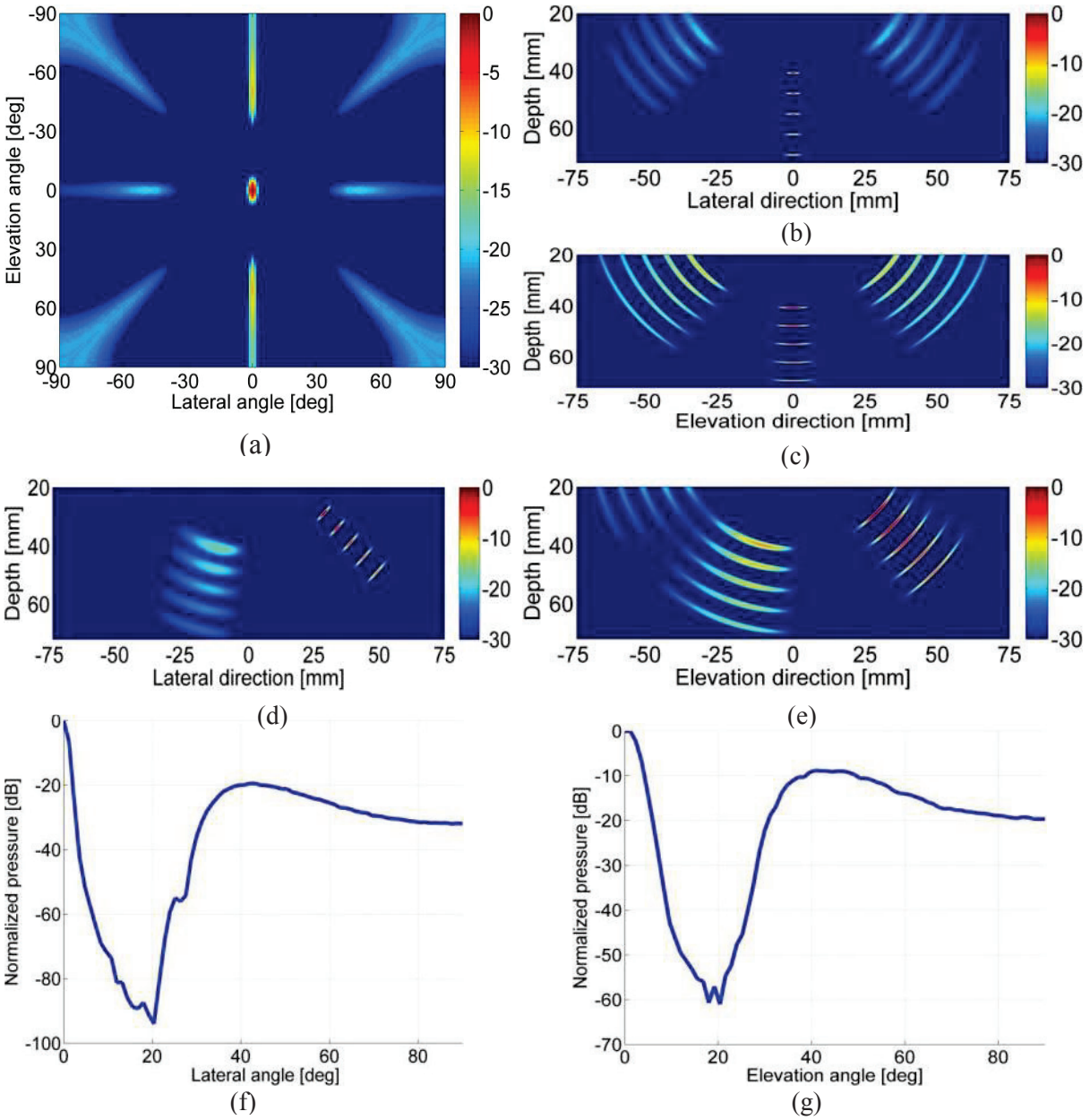

Figure 4.8 : the beam pattern of the dense 8x24 2D array of 192 elements with (a) the c-scan beam at 50 mm, the PSF (b)-(c) unsteering and (d)-(e) steering cases, (f)-(g) the beam profiles in lateral and elevation directions, respectively. The PSF shows the mirror images due to the grating lobes and the beam profiles give their energy compared to the main lobe.

4.4.2. Optimized sparse arrays

The application of the optimization to the 8x24 2D array is divided in two strategies:

- Using the whole 8x24 2D array of 192 elements randomly filled
- Choosing 64 elements on the whole array respecting the connection constraints of the Ula-Op
- Using 8x8 sub-arrays of 64 elements to be in concordance with the scanner channel number.

The algorithm parameters are set as follows: sidelobes level fixed to -20 dB because of the probe small size, the number of iterations is fixed to 3400 and the main lobe width equal to that of the corresponding dense array.

4.4.2.a Sparse 8x24 2D array

The optimization process is the same as the previous chapter. This configuration is just for theoretical validation as the scanner cannot simultaneously control 192 elements. As optimization constraints, the sidelobes must be lower than – 20 dB.

Evolution of element number and energy function

After 1000 iterations, the active element number reaches a steady value of 134 (Figure 4.9a). A thousand iterations are largely sufficient as the element number variation remains less than one element till 3400 iterations. About the cost function, its value increases from the dense array to some local maxima before becoming steady at its final value. The cost function range is not much important as the number of the element is not important like in the 64x16 2D arrays. The variation of the cost function value from an optimization process to another is about one unit (Figure 4.9b).

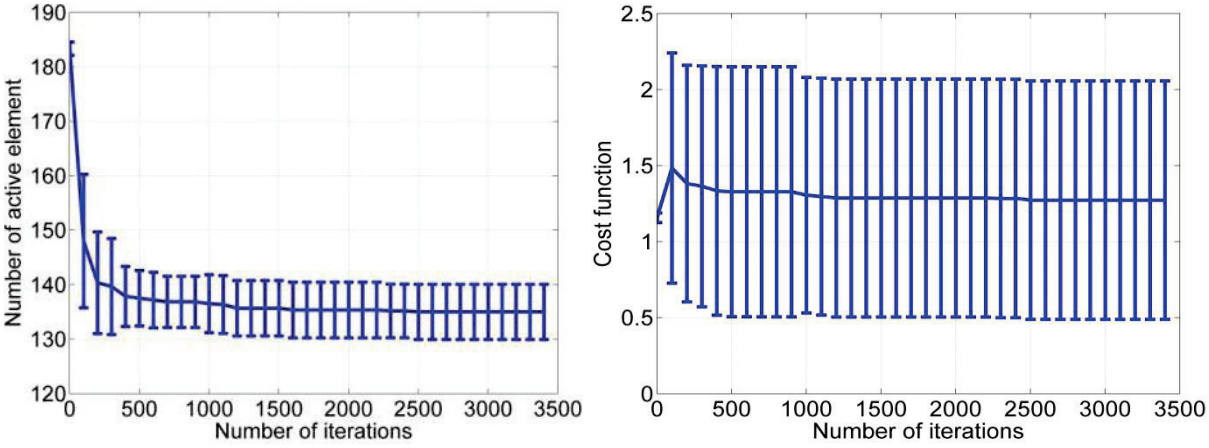

Figure 4.9: the evolution of the active element number (a) and the cost function value (b) as function of the iterations for the sparse 24x8 array. After an iteration number of 1000, the active element number reaches its final mean value (134) .

Comparison of the PSF

The PSF comparison is realized between the dense (192 elements) and the optimized sparse array (134 elements) Figure 4.10a represents the optimized sparse array corresponding to 8x24 dense array. The PSF simulations are performed using the phantom of Figure 2.11 and a Hanning apodization is applied to the dense array. The PSF of the sparse array has a better spatial resolution in both the lateral (Figure 4.10b-c) and elevation direction (Figure 4.10d-e) than the dense array (Figure 4.8b to e). The beam profiles confirm this resolution improvement with a main lobe width of 2 and 6.1 degree for the dense array against 0.7 and 4.6 degrees in the optimized sparse array in the lateral and elevation direction, respectively. The energy of the optimized sparse array is 7 dB more important than that of the dense array and the grating lobes decrease of about 2 and 5 dB in both directions (Figure 4.10g-f). The advantages of optimization can be summarized in three terms: few active elements, thinner main lobe width and better energy level.

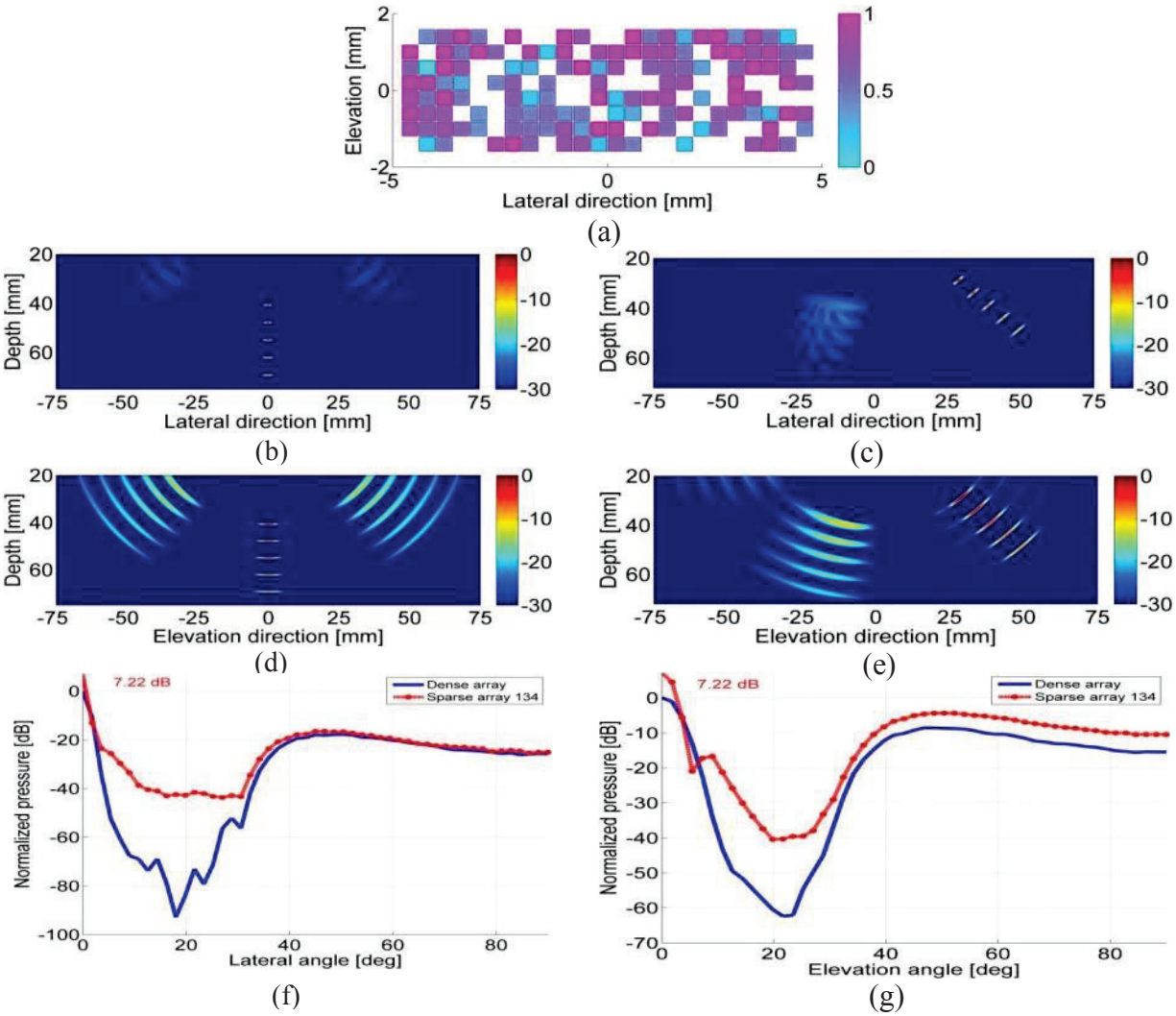

Figure 4.10: the optimized 8x24 array sparse configurations with (a) 134 elements spatial positions and apodization (b)-(c) correspond to the PSF in the lateral direction and (d)-(e) the PSF in the elevation direction in unsteering and steering cases respectively, (f)-(g) the beam profiles comparison to the dense array to estimate the energy loss. The optimized sparse array has more energy, about 7 dB than the dense array.

4.4.2.b Sparse 8x24 2D array with Ula-OP constraints

The element connection possibilities are predefined in the Ula-OP scanner. Figure 4.11 shows the impossibility of the control of arrays containing more than 64 elements. Such arrays are divided in three blocks of 64 elements and the elements number n, $n + 64$ and $n + 128$ ($n \in [1,64]$) are controlled by the same multiplexor, thus they cannot be connected at the same time.

To realize sparse arrays in this condition, 64 elements are randomly chosen between the different possibilities and optimized. The optimization aims to improve the sidelobe level (lower than – 20 dB) and the main lobe width by providing the suitable apodization coefficients to the elements. The interest of the sparse array on the whole probe is the spatial resolutions which remain at least the same as for the dense array of 192 elements.

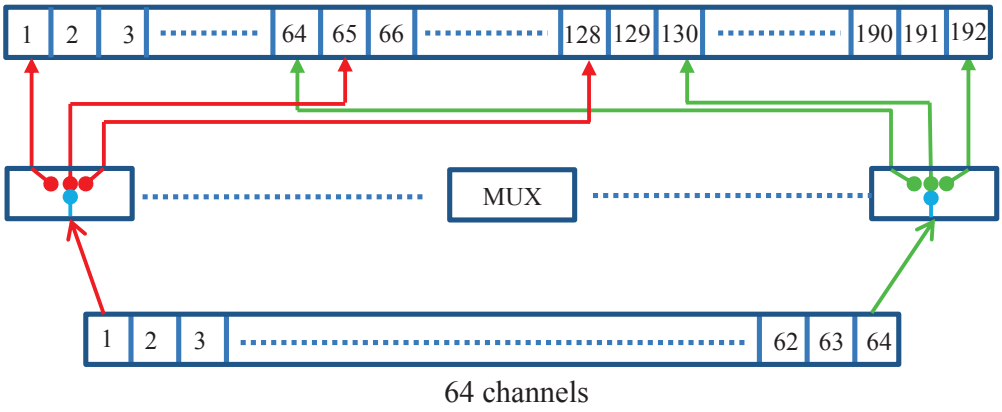

Figure 4.11: the Ula-OP scanner multiplexing system leading to elements conection constraints. The elelemnt *n*, *n*+64 and *n*+128 (with $n \in [1, 64]$) are controlled by the same multiplexor, so they can be connected at the same time.

PSF simulation

The PSF of the optimized sparse array is compared to that of the dense array of 192 elements (Figure 4.8) using the same PSF phantoms (Figure 2.11).

In the lateral direction, the mirror images of the scatterers (Figure 4.12b-c) are less important compared to those of the dense array in both unsteered and steered cases (Figure 4.8b-d) because of the coefficient harmonization by the optimization and the relative low energy of the sparse array. In the elevation direction, the same remarks can be made with a noticeable reduction of the effect of the grating lobes (Figure 4.12d-e). In both directions the spatial resolution is improved in the sparse array case as confirmed by the beam profiles of Figure 4.12f and g.

In the lateral direction, the main lobe width at – 6 dB is 0.8 degree in the sparse array against 2.1 degrees in the dense array and 4.2 degrees against 6.1 degrees in the elevation direction (Figure 4.12f-g). This resolution improvement is translated in thinner scatterer images in the PSF (Figure 4.12) compared to the dense array case (Figure 4.8). The energy loss caused by the sparse array is about 8.9 dB. The ratio between the grating lobes and the main lobe is 5 dB better in the sparse array (Figure 4.12a).

This 64-elements sparse array, taking into account the connection constraints, is the best configuration which can be currently obtained with the experimental array but unfortunately its dense array version (of 192 elements) cannot be tested in measurements for comparison.

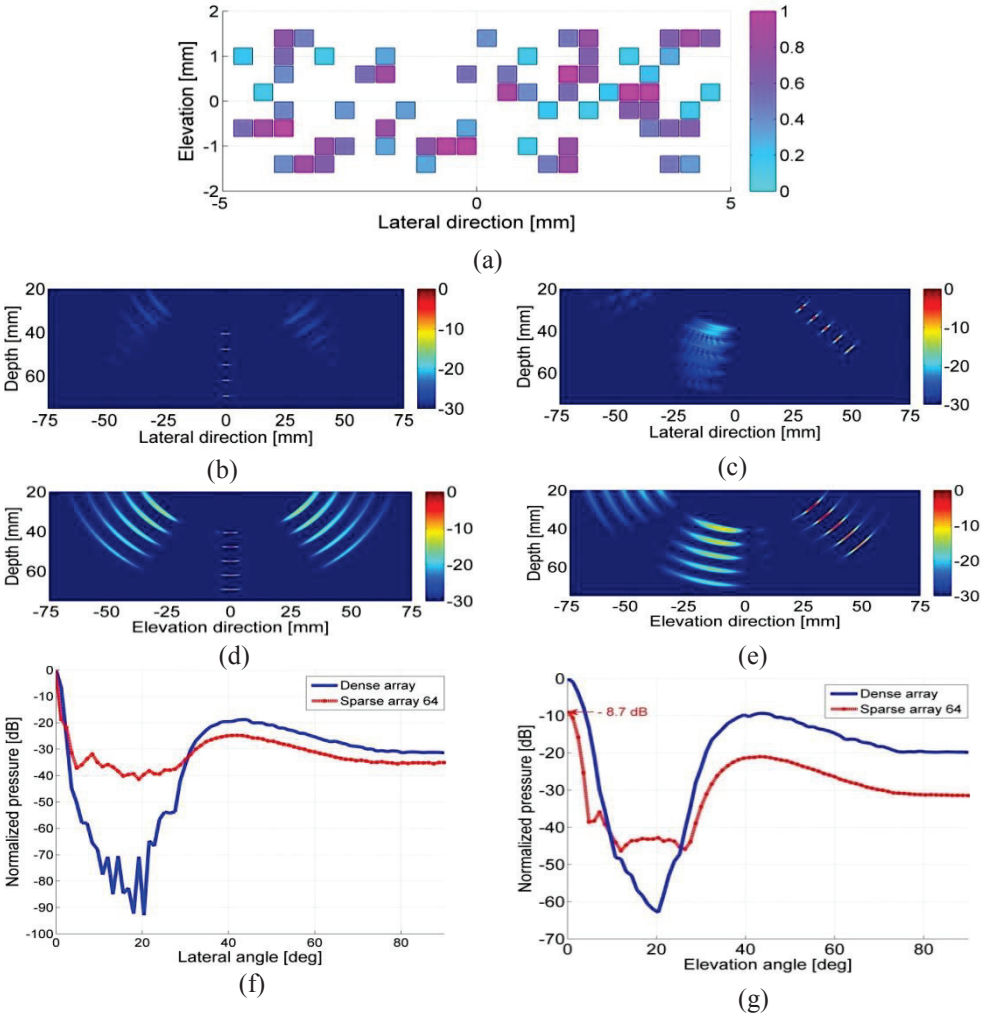

Figure 4.12: (a) the optimized sparse array of 64 active elements made on the whole probe of 192 elements taking into account the multiplexing constraints of the scanner,(b)-(c) are the PSF in the lateral direction and (d)-(e) in theelevation direction in unsteering and steering cases respectively, (f) shows the ratio between the main lobe and the grating lobes energy ratio in each case whereas (g) shows the energy level of the sparse array compared to the dense array. The energy loss is about 9 dB in the sparse array.

Phantom imaging

The experimental and simulation phantom is described in Section 3.6.2.a by the Figure 3.29. The first wire position is 6 mm, the second 19 mm and the third is at 38 mm depth. The experiments are performed with just the 64 optimized array and any comparison can be made with the dense array (of because of the connection impossibility). The transmit focus is fixed at 30 mm and the three reception foci coincide with the wires positions. The scanning sector is 60 degree width (-/+ 30°).

The images show clearly the three scatterers (wires) included in the phantom, in both directions. The spatial resolution is much better in the lateral direction (Figure 4.13a-c) than in the elevation (Figure 4.13b-d) because of the probe rectangular geometry. This spatial resolution result is predicted by the PSF in Figure 4.12. The simulation and experiment results are similar and they present beam characteristics in the same order. The energy ratio normalized by the first scatterer and the – 6 dB width of the three wires (Figure 4.13e-f) are summarized in Table 4.2.

2D array	Scatterers position (mm)	Measurements		Simulations	
		Main lobe at – 6 dB (mm)	Relative energy (dB)	Main lobe at 6 dB (mm)	Relative energy (dB)
64 elements	6	0.6/0.9	0	0.4/0.9	0
	19	0.9/2.2	1.7	0.8/2.3	1.1
	38	1.3/4.1	-2.8	1.4/4.2	-6

Table 4.2: the beam characteristics in the measurements and simulations in both the lateral and elevation directions. The – 6 dB main lobe width and the energy normailzed by that of the first scatterer are listed. The results in simulations and expriments match as well. The first scatterer has more energy than the third and less energy compared to the second in each case.

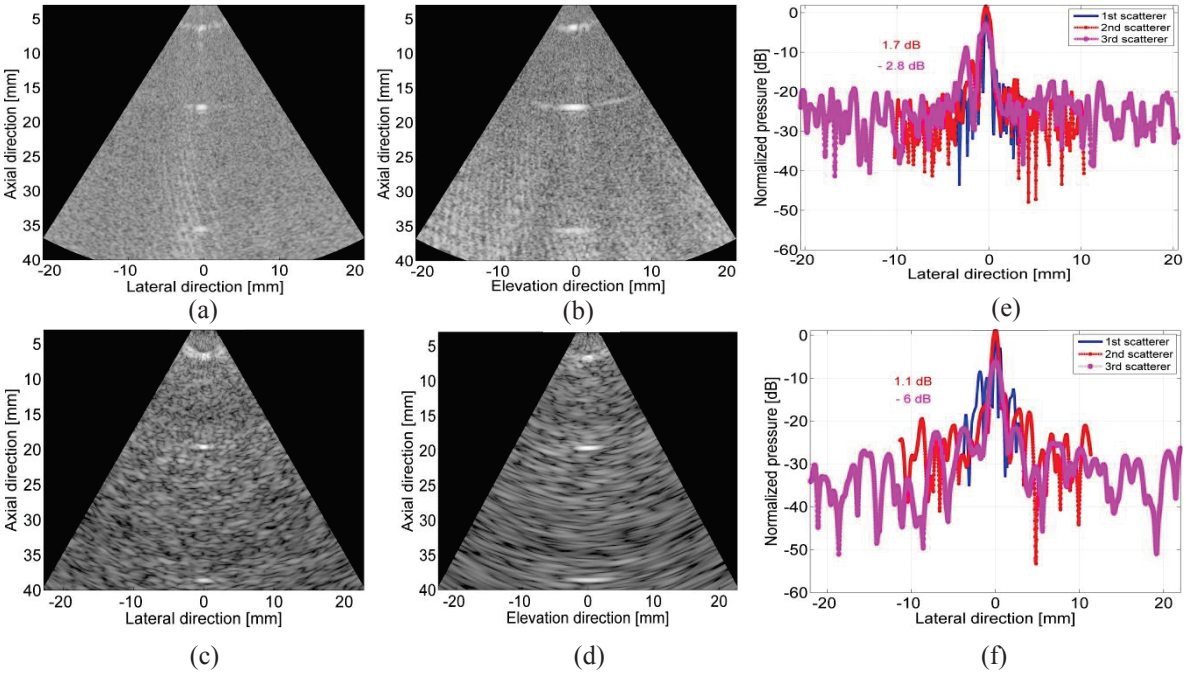

Figure 4.13: (a)-(b) experimental images with the UlaOP scanner and (c)-(d) simulated images with Field II using the optimized 64-elements sparse array taking in account the connection constraints of the UlaOp scanner in the lateral and elevation directions, respectively. The beam profiles of the three scatterers (e) in experiment and (f) in simulations. The beam profiles show the energy ratio at different scatterer positions.

4.4.2.c Sparse 8x8 sub-arrays

The 8x8 sub-array permits the experimental validation of the proposed optimization method. The sub-array considered goes from the 65th to the 128th element.

Evolution of element number and energy function

The evolution of the element number obtained after the algorithm running is presented. In Figure 4.14a the number of the active elements decreases sharply during the first eight hundred iterations going from 63 to 50, about a reduction of 22% from the initial 64 elements. The results presented correspond to the mean value and the standard deviation of the algorithm in eight optimization processes. The minimum of the mean value reached is 49 elements and the variation is about +/- 3 elements. In the experimental tests, two of the optimized arrays (47 and 53 elements) are used to evaluate the algorithm efficiency.

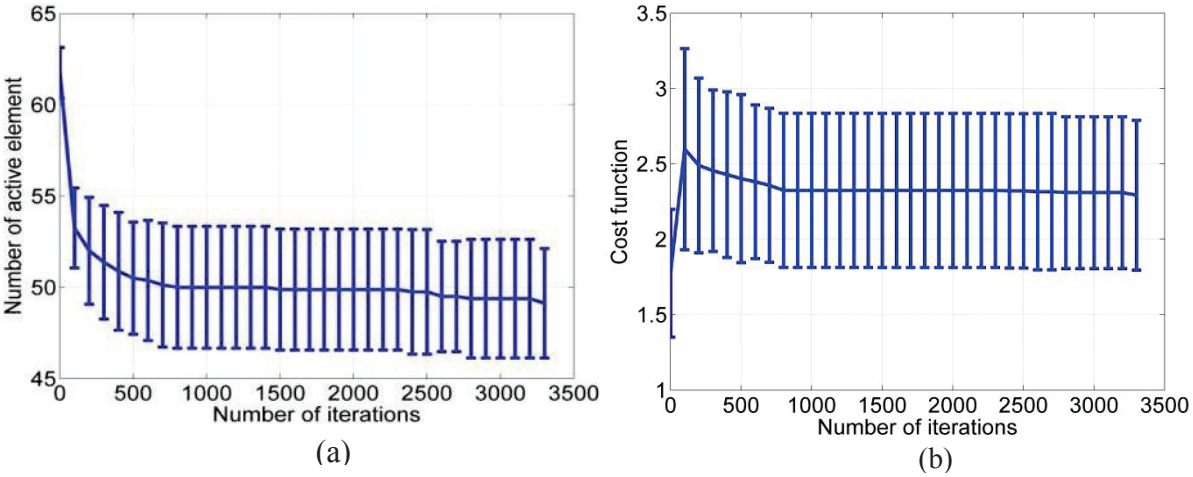

Figure 4.14: the evolution of (a) the active element number and (b) the cost function value as function of the iterations for an 8x8 2D array from the center of the 24x8 array. An iteration number of 1000 is sufficient for this small array.

Comparison of the PSF

The comparison is about the PSF of the 8x8 dense array presented in Figure 4.15a and its corresponding two optimized sparse arrays of 53 and 47 active elements. The 47-elements optimized sparse array is displayed on Figure 4.15b.

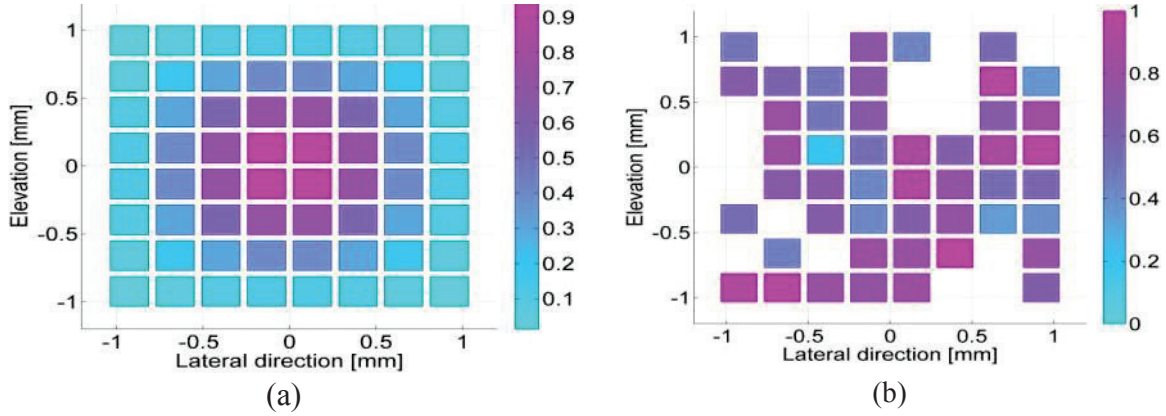

Figure 4.15: (a) the 8x8 dense array and (b) its corresponding optimized sparse array with 47 active elements. The colorbar indicates the apodization coefficients of the elements.

Figure 4.16a-b represent the PSF of three (dense and optimized) arrays when no steering is involved (the PSF in the elevation is identical as the probe are squared). In this case, the grating lobes are important but enough separated from the main lobe to permit making some imaging in a sector of 60 degrees (from -30° to 30°).

Conversely to the first 8x8 array (Section 4.3.1.), the probe was designed to respect the spatial sampling condition. This criterion is at the expense of the probe image resolution which gets worse compared to that presented in Figure 4.2. In the steering case, the grating lobes are more important (Figure 4.16c-d) as they get close to the probe axis. The beam profile in Figure 4.16e confirms that the optimized arrays keep at least the same beam characteristics as the dense array. The – 6 dB main lobe width of the dense array is 6 degrees when the optimized 53-elements and 47-elements sparse arrays have respectively 4.34 degrees and 3.92 degrees, about 30% thinner. In addition, the dense array grating lobes are 5 dB more important than those of the optimized sparse arrays. The sidelobes are higher in the

sparse arrays about 20 dB (fixed by the algorithm) while they are not existent in the dense array. In terms of the probe sensitivity, Figure 4.16f shows that the dense array presents less energy than the optimized 53 and 47-elements sparse arrays. The energy is 10 dB and 7 dB more important in the sparse arrays. This result is a particular case due to the small size of the array used. On Figure 2.11b the apodization coefficients provided by the optimization are between 0.2 and 1 whereas the Hanning apodization applied to the dense array contain a lot of small coefficients. In addition, given the few number of deactivated elements (between 11 and 17), the energy of the sparse arrays remains greater than that of the dense array. In practice, the algorithm is useful for big arrays allowing the limitation the beam deterioration due to the sparse array technique.

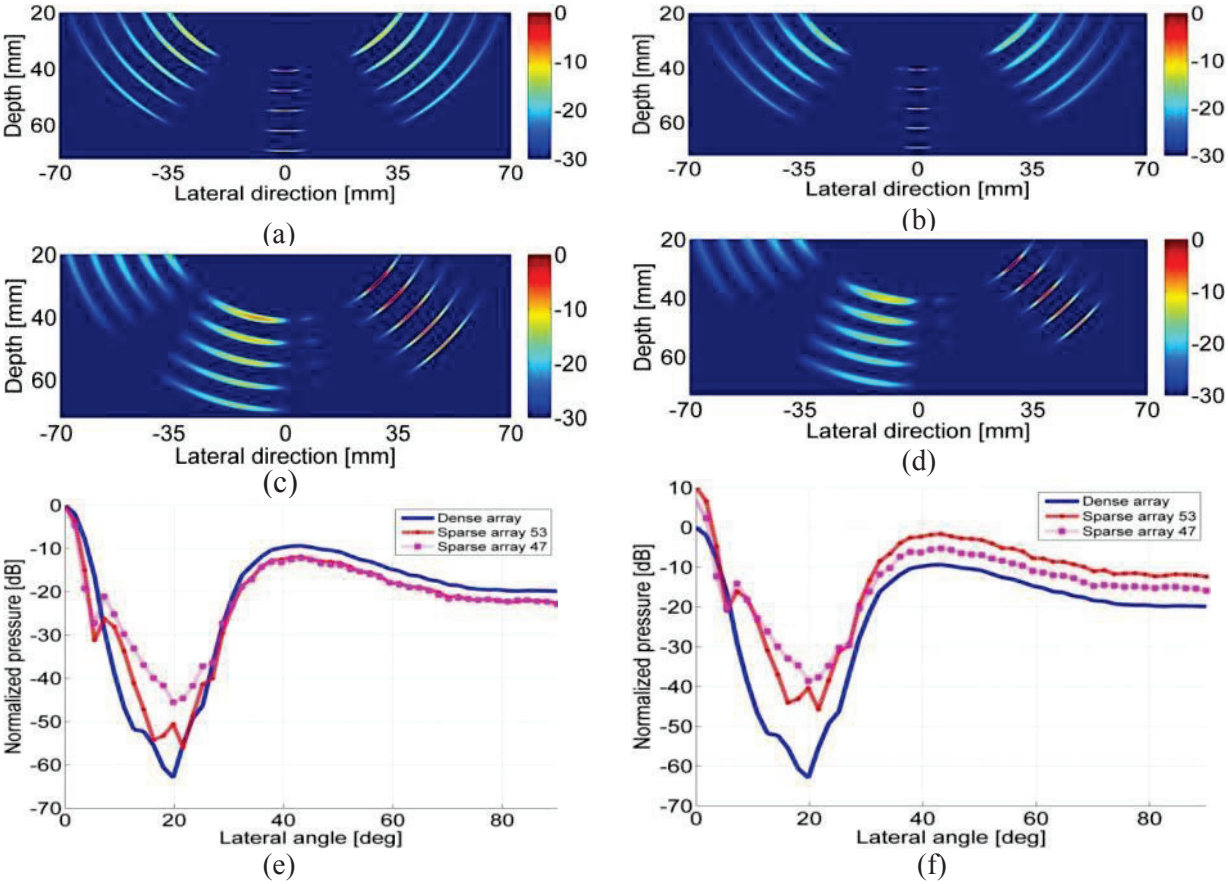

Figure 4.16: PSF of the dense array (a)-(c) and the optimized sparse array (53 and 47 elements) (b)-(d) in the lateral direction in steering and unsteering case respectively (the same PSF in the elevation by symmetry). The comparison of the beam profiles of the dense and the two sparse arrays, (e) shows the ratio between the main lobe and the grating lobes energy ratio in each case whereas (f) shows the energy level of the two sparse arrays compared to the dense 8x8 array. The sparse arrays have respectively 10 dB and 7 dB more energy than the dense array.

4.4.3. Phantom imaging

The experimental phantom is described in Section 3.6.2.a by the Figure 3.29. The imaging is performed by the central 8x8 sub-array and its corresponding optimized sparse arrays (53 and 47 active elements).

4.4.3.a Cyst phantom imaging

The small 8x8 sub-array and its corresponding optimized sparse arrays are further compared. The simulations and the measurements are performed in a sector of 60 degrees (from -30 to 30 degrees) and only the zone surrounded on the phantom (Figure 3.29b) is considered. The comparison criteria are the image spatial resolution and the signal-to-noise ratio (energy). Figure 4.17a-b, and c represents the images of the wires in the lateral directions with respectively the dense, the 53-elements and the 47-elements optimized sparse arrays. The first wire position is 6 mm, the second 19 mm and the third is at 38 mm depth. The resolution in the sectorial scanning gets worse as the beam goes deeper. This spatial resolution deterioration comes from two main factors: the array's relative small size (3.17 x 3.17 mm^2) and the intrinsic resolution reduction of the scanning type. For that reason, the second wire appears wider than the first one and the third wider than the second too.

In all three arrays, the wires are distinguishable. The sidelobes appear on the sparse array images as highlighted in Figure 4.17b-c-e and f at the second wire position.

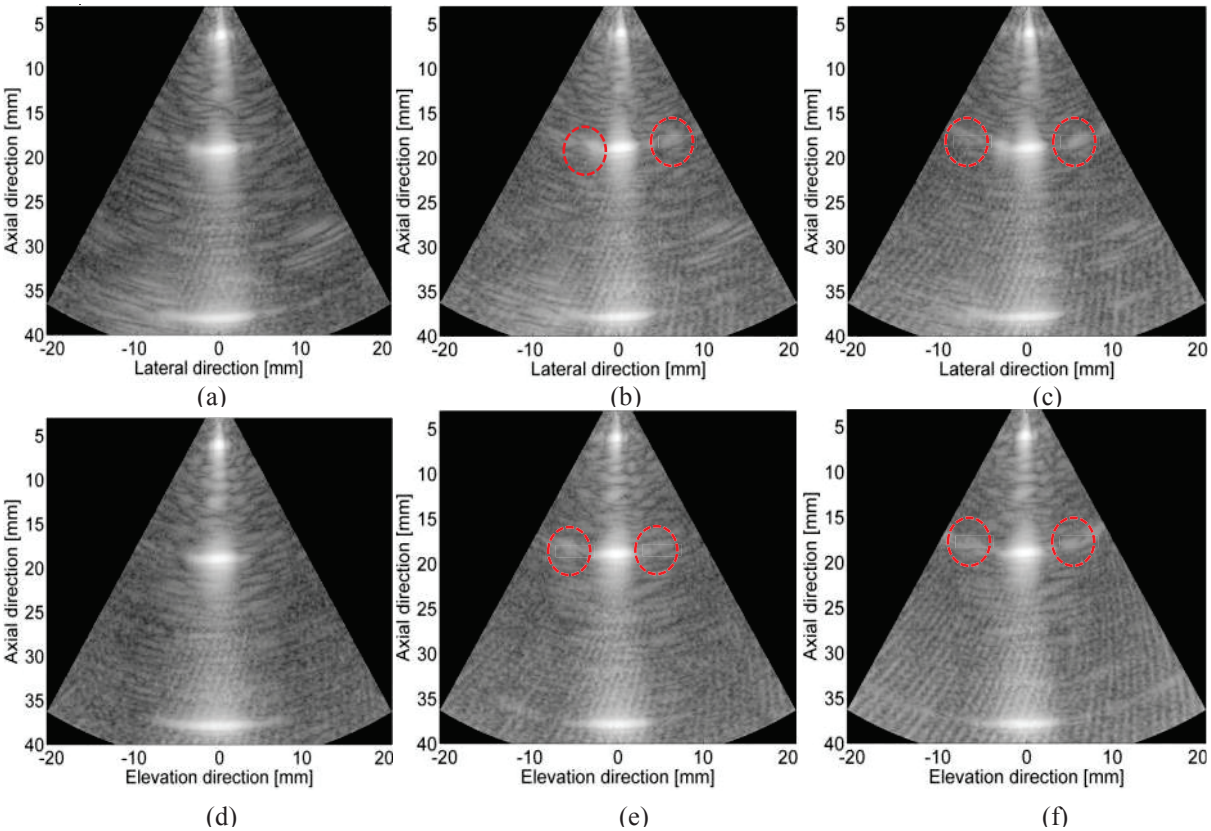

Figure 4.17: the experimental images of three wires in the lateral direction with (a) the dense array (b) the 53-elements optimized spasre array and (c) the 47-elements optimized sparse arrays, (d), (e) and (f) are the same images in the elevation direction. The lateral resolution gets worse as the wire is deeper. The sidelobes apparition in the sparse arrays give rise to mirror images near the real wire image (surrounded by the circles) but their value is considerably reduced by the optimization.

In simulations (Figure 4.18), the results confirm the ability of the 8x8 sub-array to observe the inclusions. The size and the positions of the wires correspond to those obtained by measurements. The near-field wires are correctly detected with a good resolution and those situated at 38 mm from the probe appear too large for the same reason as in the experiments. The third wire is difficult to see because of the energy loss with all the three arrays. The sidelobes effect noticed in experiments is not visible in simulation results because their energy

is not enough to make a contrast difference with the phantom background. The resolution is the same in both lateral and elevation for each array.

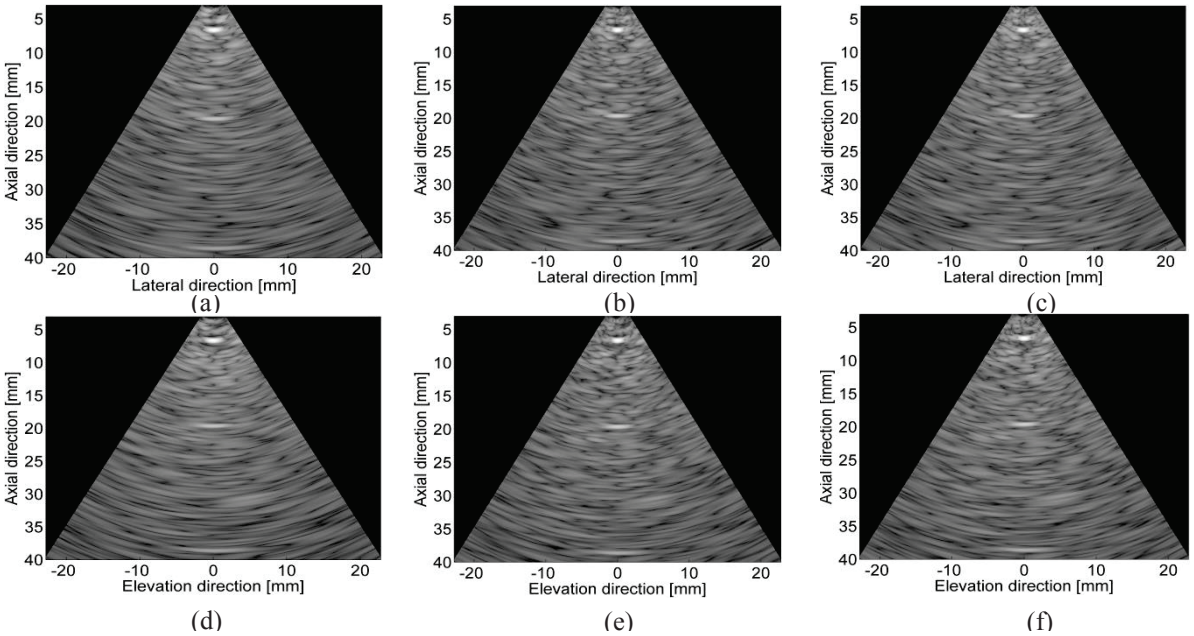

Figure 4.18: the simulated images of three wires in the lateral direction with (a) the dense array (b) the 53-elements optimized spasre array and (c) the 47-elements optimized sparse arrays, (d), (e) and (f) are the same images in the elevation direction. The lateral resolution gets worse as the wire is deep. The sidelobes are visible in simulation because their energy is not enough to make a contrast difference with the phantom background.

4.4.3.a Phantom beam profiles

The beam profiles give precise information about the spatial resolution of each array at the wires positions. The wire width and the energy ratio between the dense and the sparse arrays are presented. Usually, the sparse array causes energy loss compared to the dense array because of the active element number reduction but the small arrays constitute a special case. In the first wire position, in the near field, the dense array energy is 1.16 and 1.24 dB greater than that of the 53 and the 47-optimized sparse arrays in the lateral direction (Figure 4.19a). In the elevation direction, this energy ratio is 1.12 and 1.87 dB (Figure 4.19b). These results are not in agreement with the theoretical optimization results probably because the optimization is made in the far field. In the medium field at 20 mm, the sparse arrays have more energy than the dense array (Figure 4.19c-d). The same tendency is noticed at 38 mm in both directions (Figure 4.19e-f). This energy ratio between the dense and the sparse arrays show the improvement brought by the optimization in addition to the element number reduction.

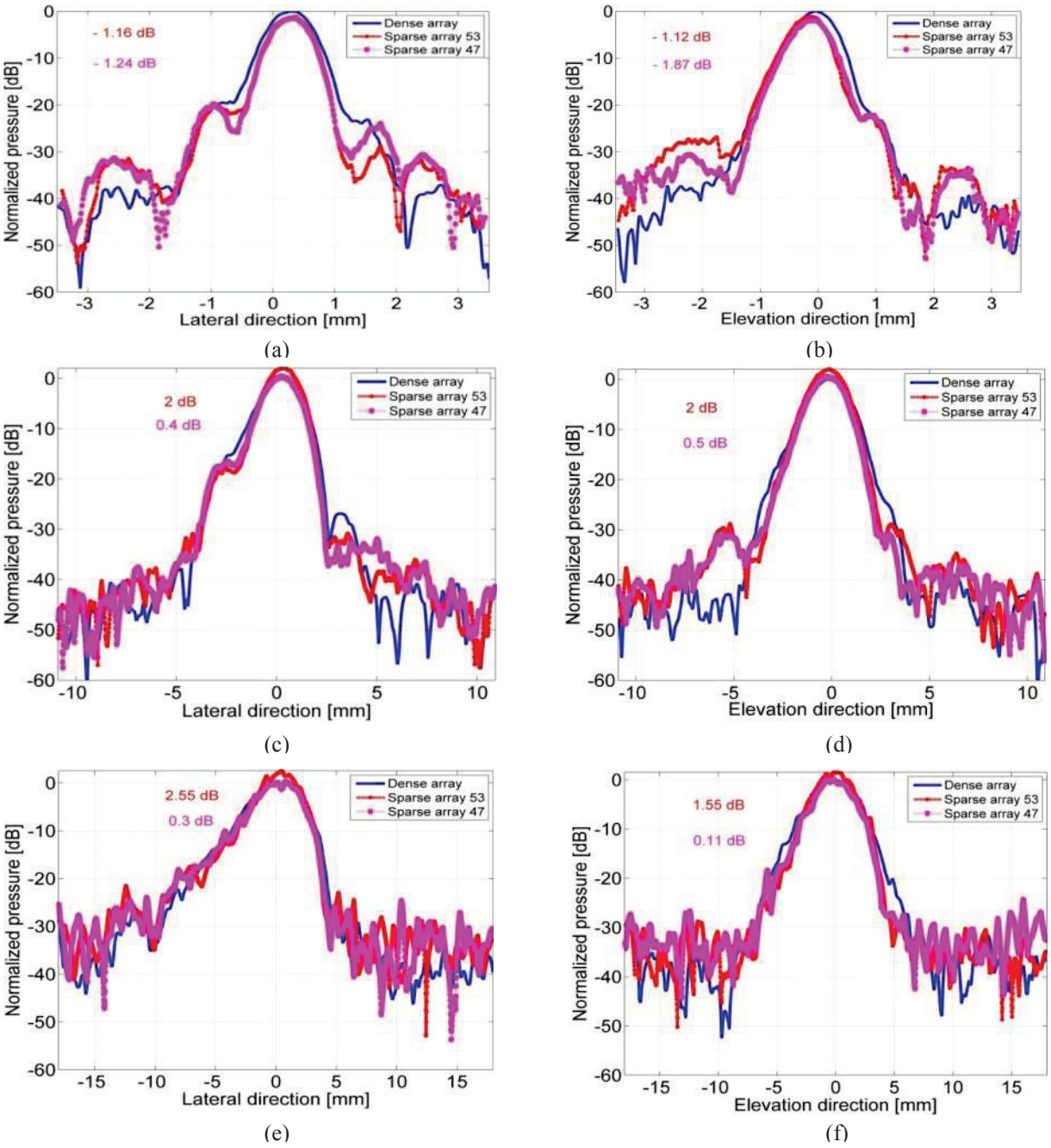

Figure 4.19: the beam profiles of 8x8 dense array and the 53-elements and the 47-elements optimized sparse arrays at the first wire position (6 mm) (a)-(b), the second wire position (19 mm) (c)-(d) and the third wire position(38 mm) (e)-(f) in lateral and elevation directions,respectively. These beam profiles are normalized by that of the dense array to evaluable the energy of the sparse arrays. Int the near field, the dense array energy is about 1.1 to 1.8 greater than that the spasre arrays while in the far field, its energy is less than that of 53-elements spasre array of 2 dB and 0.3 dB compared to the 47-elements spasre array.

The measurement of the wire width at – 6 dB from the first to the third wire with the dense and the optimized arrays is summarized in Table 4.3 in both lateral and elevation directions. The images in the elevation direction are represented by Figure 4.17e-f and g and they have the same characteristics as those in the lateral direction except the – 6 dB width of the wires (Table 4.3). These values give a general survey of the resolution improvement provided by the optimization.

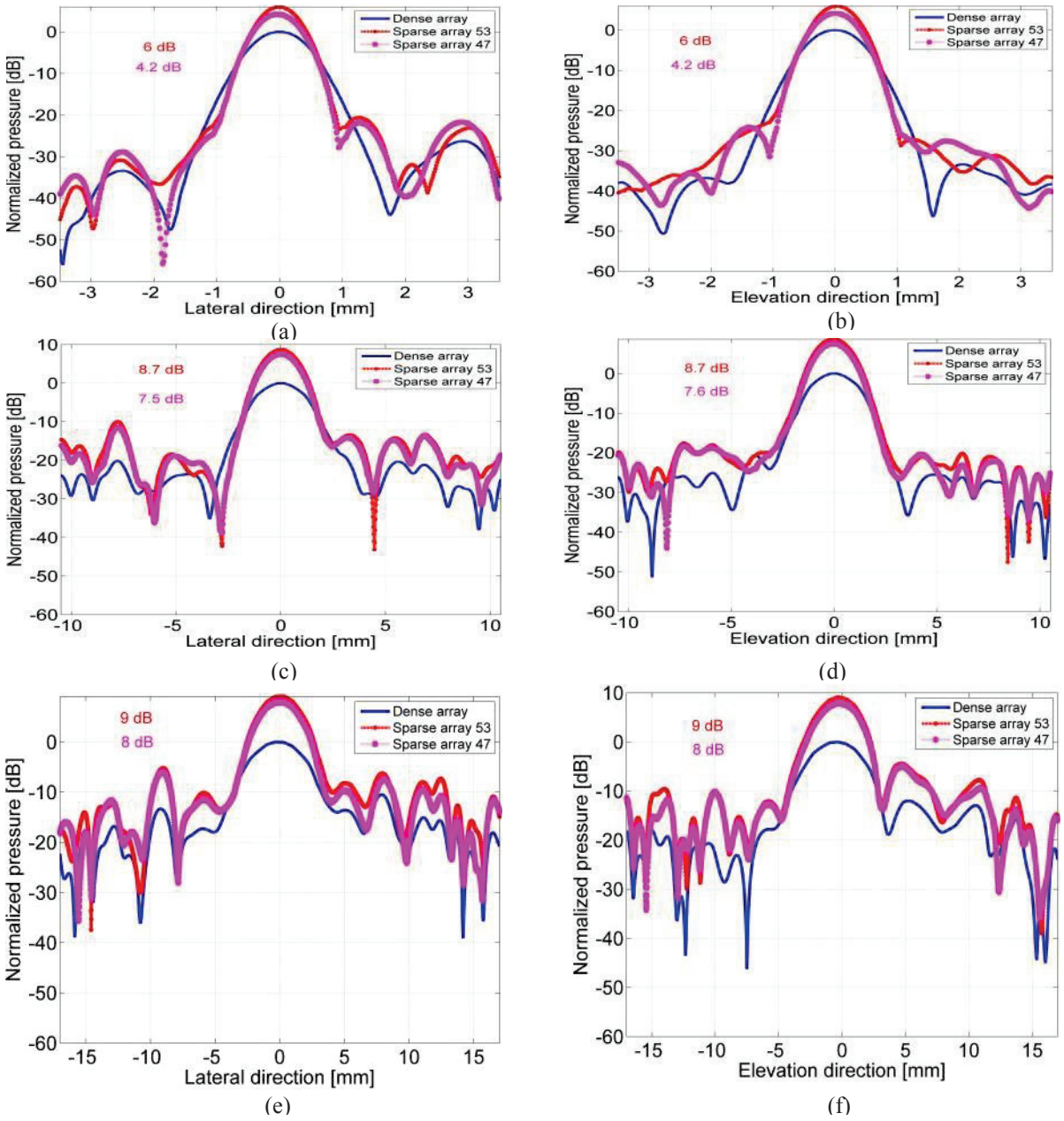

Figure 4.20:the simulated beam profiles of 8x8 dense array and the 53-elements and the 47-elements optimized sparse arrays at the first wire position (6 mm) (a)-(b), the second wire position (19 mm) (c)-(d) and the third wire position(38 mm) (e)-(f) in lateral and elevation directions,respectively. These beam profiles are normalized by that of the dense array to evaluable the energy of the sparse arrays. Int the near field, the dense array energy is about 1.1 to 1.8 greater than that the spasre arrays while in the far field, its energy is less than that of 53-elements spasre array of 2 dB and 0.3 dB compared to the 47-elements

In simulation, the beam profiles (Figure 4.20) confirm the observations made on the PSF (Figure 4.16e-f). In both directions, the – 6 dB main lobe width of the dense array is 1.18 mm, 3 mm and 5.44 mm for three wires from the shallowest to the deepest. In the 53-elements sparse array their values are 0.89 mm, 2.4 mm 4.38 mm and 0.96 mm, 2.36 mm and 4.30 mm for the 47-elements sparse array (Table 4.3). These values are in accordance with the measurements results. The energy ratio between the dense and the sparse arrays is about 6 dB and 4 dB in the near field against 9 dB and 8 dB in medium and far field. These simulation results are different from the measurements but in both cases the optimized sparse arrays provide more energy in the medium and far field. The difference between simulation and

experiment results can come from physical phenomena such as the medium (attenuation, diffraction) and the probe property (element sensitivity). The results validate the capability of the optimization to maintain good imaging characteristics.

4.4.3.b Summary of comparison

The comparison between the simulation and the experimental results are summarized in the Table 4.3. The main lobe width determining the spatial (lateral and elevation) resolutions and the energies (normalized by that of the dense array at each scatterer position) are presented. The lateral and elevation directions have almost the same characteristics in each case. The table highlights the resolution and the energy improvement provided by the optimization applied the sparse arrays.

2D array	Scatterers position (mm)	Measurements		Simulations	
		Main lobe at – 6 dB (mm)	Relative energy (dB)	Main lobe at – 6 dB (mm)	Relative energy (dB)
8x8=64	6	0.91	0	1.18	0
	19	2.57	0	3	0
	38	5.44	0	5.44	0
53	6	0.83	-1.1	0.89	6
	19	2.17	2	2.4	8.7
	38	3.93	2	4.38	9
47	6	0.8	-1.8	0.96	4.2
	19	2.25	0.5	2.36	7.5
	38	4.62	0.3	4.30	8

Table 4.3: summary of comparsion between the measurements and the simulation results using the dense 8x8 array, the 53-elements and 47-elements optimized sparse arrays. The table puts into evidence the main lobe thinning and the increase of the energy in the medium and far fields provided by the sparse arrays.

4.5. Conclusion

This chapter presents the prototype probes used in the experimental measurements. The developed optimization algorithm is tested in realistic case on the 8x8 sub-array from the 8x24 2D arrays manufactured in this work. The comparison between the simulations and the experimental results is made to confirm the validity of the optimization algorithm. The comparison criteria are the spatial resolutions, the energy loss and the overall image quality provided by the optimized sparse arrays compared to the dense array. All the results confirm the imaging capability of the optimized arrays despite the active elements number reduction. These results open the way to the 3D imaging from the 2D arrays using optimized sparse array techniques without any additional complexity to the current ultrasound beamformers (scanners).

To efficiently validate the methods developed, large 2D arrays and scanners with more channels are necessary to significantly feel the power of the optimization. Such equipment provides better imaging features than the small arrays used in these experiments.

Conclusion

In this work, improved extensions of the classical methods in the 2D matrix arrays design are proposed and new more efficient techniques are developed with clear demonstrations of their superiority.

Firstly an extension of the simulated annealing optimization algorithm is proposed to have a more rigorous mathematical formulation as well as an efficient reduction of the active elements number. This improved algorithm permits to provide more reduced arrays keeping at least the same beam characteristics as in the reference methods. Several optimizations are performed to confirm the algorithm's robustness and its precision. The final active elements number in the arrays is considerably reduced to suit to given beam features.

Secondly, complete innovative techniques are presented. In these techniques the regular grid classically used in the 2D array design is suppressed. This grid is responsible for many constraints in the realization of efficient matrix arrays. It superimposes the piezoelectric elements small size by respecting the spatial sampling conditions and thereby favors the apparition of undesired phenomena in the arrays beam pattern known as the grating lobes. The small size of the element deteriorates the sensitivity of the whole array and increases its necessary element number. The new techniques are based on a completely random positioning of the array element. This approach has the potential to overcome the above mentioned limitations and opens the way to many interesting effects on the 2D array. The elements can be several times wider than in the classical methods leading to a natural reduction of their number for a given array footprint. This reduction makes possible the control of the 2D arrays by scanners initially adapted to the 1D array. Moreover, the wider are the elements, the more important is their energy and the thinner is the beam width. Direct consequences of this property are the array sensitivity increase and its spatial resolution improvement. In applications needing a large directivity (large main lobe), a conjugation of both wide and small elements permits to keep both good sensitivity without modifying the main lobe in relation to an array containing only small elements. The new techniques developed are optimized using the improved optimization algorithm proposed in this work.

Thirdly a mean 2D array composed of 8x24=192 elements is manufactured to validate the optimization methods developed theoretically and tested by simulations. This array contains regular aligned elements and is used to evaluate the standard sparse arrays imaging capabilities. The experimental results are compared to those of the simulations to confirm the validity of the methods in realistic studies. These measurements are realized on an industrial tissue mimicking phantoms but tests on human tissues will be performed in the near future.

Perspectives

This thesis proposes a number of solutions for the element number reduction using matrix arrays. However there are still open problem. The perspectives given by this thesis can be summarized as follows:

Take into account in the optimization process more complex parameters as different shaped elements (rectangle, triangle) and adapt their size as the function of available surface in their position.

A comparison study of the simulated annealing with another optimization algorithm present in literature will be interesting, mainly the genetic algorithms which seems to provide interesting solutions in some complex optimization problems.

The 3D volume reconstruction is an essential field to develop. The combination of the (non-grid) sparse array and the compressive sensing are interesting fields to explore for the real time 3D imaging as both are sparse methods to minimize the necessary data amount in the reconstruction.

The realization of a prototype array designed on the basis of the proposed non-grid array technique to validate by experiment the potentialities given by this new element positioning strategy. This prototype may have a footprint large enough to contain wide elements to confirm the suppression of the beam undesired lobes.

Development of a simulation tool for general 2D array imaging and particularly suitable to the non-grid arrays to realize volume simulations in an acceptable running time. Currently, a simple volume of tens of planes can take more than a day under Field II.

Experimental tests in medical field (hospital) are required to more validate the preliminary phantom imaging.

Personal bibliography

International journal

[DIAR-13] B. Diarra, M. Robini, P. Tortoli, C. Cachard and H. Liebgott, "Design of optimal 2-D non-grid sparse arrays for medical ultrasound ", *IEEE Transactions on Biomedical Engineering*, pp. 3093-3102, 2013.

International conferences

[DIAR-13] B. Diarra, M. Robini, H. Liebgott, C. Cachard, and P. Tortoli, "Variable-size elements in 2D sparse arrays for 3D medical ultrasound", *IEEE International Ultrasonics Symposium*, Prague, Czech Republic, accepted, 2013.

[DIAR-12c] B. Diarra, H. Liebgott, C. Cachard, and P. Tortoli, "Non-grid based elements positioning for optimal 2D array beams", *IEEE International Ultrasonics Symposium*, Dresden, Germany, pp. 1-4, 2012.

[DIAR-12b] B. Diarra, H. Liebgott, M. Robini, P. Tortoli, and C. Cachard, "Optimized 2-D array design for ultrasound imaging", *EUSIPCO*, Bucharest, Romania, pp. 2718-2722, 2012.

[DIAR-11] B. Diarra, H. Liebgott, P. Tortoli, and C. Cachard, "2D matrix array optimization by simulated annealing for 3D hepatic imaging", *IEEE International Ultrasonics Symposium*, Orlando, Florida, USA, pp. 1595-1598, 2011 .

National conference

[DIAR-12a] B. Diarra, H. Liebgott, P. Tortoli, and C. Cachard, "Sparse array techniques for 2D array ultrasound imaging", *Acoustics*, Nantes, France, pp. 1591-1596, 2012.

Bibliography

Aboofazeli M., Abolmaesumi P., Mousavi P. and Fichtinger G. (2009) "A new scheme for curved needle segmentation in three-dimensional ultrasound images." *IEEE International Symposium on Biomedical Imaging*, Boston, Massachusetts, USA, 1067–1070.

Angelsen B. A. J., Torp H., Holm S., Kristoffersen K. and Whittingham T. A. (1995) "Which transducer array is best?" *European Journal of Ultrasound*, 2(2), 151–164.

Austeng A. and Holm S. (2000) "Sparse arrays for real-time 3D imaging, simulated and experimental results." *IEEE International Ultrasonics Symposium*, San Juan , Puerto Rico, 1187–1190.

Austeng A. and Holm S. (2002) "Sparse 2-D arrays for 3-D phased array imaging - design methods." *IEEE Transactions on Ultrasonics, Ferroelectrics and Frequency Control*, 49, 1073–1086.

Austeng Andreas and Holm S. (2002) "Sparse 2-d arrays for 3-D phased array imaging--experimental validation." *IEEE Transactions on Ultrasonics, Ferroelectrics, and Frequency Control*, 49, 1087–1093.

Bamber J. C. and Dickinson R. J. (1980) "Ultrasonic B-scanning: a computer simulation." *Physics in medicine and biology*, 25(3), 463–479.

Barthe P. G. and Slayton M. H. (1996) "Characterization of 1.5-D ultrasound transducer arrays." *IEEE International Ultrasonics Symposium*, San Antonio, TX , USA, 1489–1493 vol.2.

Basset O. and Cachard C. (2007) "Ultrasound image post-processing – Application to segmentation." *Physics for Medical Imaging Applications*, NATO Science Series, Springer Netherlands, 227–239.

Bavaro V., Caliano G. and Pappalardo M. (2008) "Element shape design of 2-D CMUT arrays for reducing grating lobes." *IEEE Transactions on Ultrasonics, Ferroelectrics and Frequency Control*, 55(2), 308–318.

Bax J., Cool D., Gardi L., Knight K., Smith D., Montreuil J., Sherebrin S., Romagnoli C. and Fenster A. (2008) "Mechanically assisted 3D ultrasound guided prostate biopsy system." *Medical physics*, 35(12), 5397–5410.

Behar V. and Nikolov M. (2007) "Sparse Array Optimization by Using the Simulated Annealing Algorithm." *Numerical Methods and Applications*, Springer Berlin Heidelberg, Berlin, Heidelberg, 223–230.

Belohlavek M., Foley D. A., Gerber T. C., Kinter T. M., Greenleaf J. F. and Seward J. B. (1993) "Three- and Four-Dimensional Cardiovascular Ultrasound Imaging: A New Era for Echocardiography." *Mayo Clinic Proceedings*, 68(3), 221–240.

Boni E., Bassi L., Dallai A., Guidi F., Ramalli A., Ricci S., Housden J. and Tortoli P. (2012) "A reconfigurable and programmable FPGA-based system for nonstandard ultrasound methods." *IEEE Transactions on Ultrasonics, Ferroelectrics and Frequency Control*, 59(7), 1378–1385.

Brandwood D. (2012) *Fourier Transforms in Radar and Signal Processing, Second Edition*. Artech House.

Brant W. E. (2001) *The Core Curriculum: Ultrasound*. Lippincott Williams & Wilkins.

Brunke S. S. and Lockwood G. R. (1997) "Broad-bandwidth radiation patterns of sparse two-dimensional vernier arrays." *IEEE Transactions on Ultrasonics, Ferroelectrics and Frequency Control*, 44(5), 1101–1109.

Bureau J.-M., Steichen W. and Lebail G. (1998) “A two-dimensional transducer array for real-time 3D medical ultrasound imaging.” *IEEE International Ultrasonics Symposium*, IEEE, Sendai , Japan, 1065–1068.

Canals R., Lamarque G. and Chatain P. (1999) “Volumetric ultrasound system for left ventricle motion imaging.” *IEEE Transactions on Ultrasonics, Ferroelectrics, and Frequency Control*, 46(6), 1527–1538.

Candès E. J., Wakin M. B. and Boyd S. P. (2008) “Enhancing Sparsity by Reweighted ℓ 1 Minimization.” *Journal of Fourier Analysis and Applications*, 14, 877–905.

Caorsi S., Lommi A., Massa A., Piffer S. and Trucco A. (2002) “Planar antenna array design with a multi-purpose GA-based procedure.” *Microwave and Optical Technology Letters*, 35(6), 428–430.

Cardone G., Cincotti G., Gori P. and Pappalardo M. (2001) “Optimization of wide-band linear arrays.” *IEEE Transactions on Ultrasonics, Ferroelectrics, and Frequency Control*, 48(4), 943–952.

Catoni O. (1992) “Rough Large Deviation Estimates for Simulated Annealing: Application to Exponential Schedules.” *The Annals of Probability*, 20, 1109–1146.

Chen P., Shen B., Zhou L. and Chen Y. (2010) “Optimized simulated annealing algorithm for thinning and weighting large planar arrays.” *Journal of Zhejiang University SCIENCE C*, 11, 261–269.

Chi Hyung Seo and Yen J. T. (2009) “A 256 x 256 2-D array transducer with row-column addressing for 3-D rectilinear imaging.” *IEEE Transactions on Ultrasonics, Ferroelectrics and Frequency Control*, 56, 837–847.

Chitre M. A. and Potter J. R. (1998) “Optimization and Beamforming of a Two Dimensional Sparse Array.” *High Performance Computing*, 98.

Curiel L., Chavrier F., Souchon R., Birer A. and Chapelon J. Y. (2002) “1.5-D high intensity focused ultrasound array for non-invasive prostate cancer surgery.” *Ultrasonics, Ferroelectrics and Frequency Control, IEEE Transactions on*, 49(2), 231–242.

Daft C. M. W., Wildes D. G., Thomas L. J., Smith L. S., Lewandowski R. S., Leue W. M., Rigby K. W., Chalek C. L. and Hatfield W. T. (1994) “A 1.5D transducer for medical ultrasound.” *IEEE International Ultrasonics Symposium*, Cannes , France, 1491–1495.

Daher N. M. and Yen J. T. (2006) “2-D array for 3-D Ultrasound Imaging Using Synthetic Aperture Techniques.” *IEEE transactions on ultrasonics, ferroelectrics, and frequency control*, 53, 912–924.

Daubechies I., DeVore R., Fornasier M. and Güntürk C. S. (2010) “Iteratively reweighted least squares minimization for sparse recovery.” *Communications on Pure and Applied Mathematics*, 63, 1–38.

Dhanantwari A. C., Stergiopoulos S., Song L., Parodi C., Bertora F., Pellegretti P. and Questa A. (2004) “An efficient 3D beamformer implementation for real-time 4D ultrasound systems deploying planar array probes.” *IEEE International Ultrasonics Symposium*, Montréal, Canada, 1421– 1424.

Diarra B., Liebgott H., Cachard C. and Tortoli P. (2012) “Non-grid based elements positioning for optimal 2D array beams.” *IEEE International Ultrasonics Symposium*.

Diarra B., Liebgott H., Robini M., Tortoli P. and Cachard C. (2012) “Optimized 2D array design for Ultrasound imaging.” *European Signal Processing Conference*, 2718–2722.

Diarra B., Liebgott H., Tortoli P. and Cachard C. (2011) "2D matrix array optimization by simulated annealing for 3D hepatic imaging." *IEEE International Ultrasonics Symposium*, 1595 –1598.

Diarra Bakary, Liebgott H., Tortoli P. and Cachard C. (2012) "Sparse array techniques for 2D array ultrasound imaging." *Acoustics*, S. F. d' Acoustique, ed., Nantes, France, 1591–1596.

Diarra Bakary, Robini M., Liebgott H., Cachard C. and Tortoli P. (2013) "Variable-size elements in 2D sparse arrays for 3D medical ultrasound." *IEEE International Ultrasonics Symposium*, Prague, Czech Republic.

Diarra B., Robini M., Tortoli P., Cachard C. and Liebgott H. (2013) "Design of optimal 2-D non-grid sparse arrays for medical ultrasound." *IEEE Transactions on Biomedical Engineering*, (99).

Ding M. and Fenster A. (2003) "A real-time biopsy needle segmentation technique using Hough transform." *Medical Physics*, 30(8), 2222–2233.

Eames M. D. C. and Hossack J. A. (2008) "Fabrication and Evaluation of Fully-Sampled, Two-Dimensional Transducer Array for 'Sonic Window' Imaging System." *Ultrasonics*, 48(5), 376–383.

Eames M., Zhou S. and Hossack J. (2005) "High element count [3600], fully sampled, two dimensional transducer array." *IEEE International Ultrasonics Symposium*, 2243–2246.

Fernandez A. T., Gammelmark K. L., Dahl J. J., Keen C. G., Gauss R. C. and Trahey G. E. (2003) "Synthetic elevation beamforming and image acquisition capabilities using an 8 × 128 1.75D array." *IEEE Transactions on Ultrasonics, Ferroelectrics and Frequency Control*, 50, 40 – 57.

Fleury G. (2013) "Personal communication."

Fuller M. I., Blalock T. N., Hossack J. A. and Walker W. F. (2003) "A portable, low-cost, highly integrated, 3D medical ultrasound system." *IEEE International Ultrasonics Symposium*, 38–41 Vol.1.

Fuller M. I., Ranganathan K., Zhou S., Blalock T. N., Hossack J. A. and Walker W. F. (2008) "Experimental system prototype of a portable, low-cost, C-scan ultrasound imaging device." *IEEE Transactions on Biomedical Engineering*, 55(2 Pt 1), 519–530.

Gee A., Prager R., Treece G. and Berman L. (2002) "Narrow-band volume rendering for freehand 3D ultrasound." *Computers & Graphics*, 26(3), 463–476.

Gee A., Prager R., Treece G. and Berman L. (2003) "Engineering a freehand 3D ultrasound system." *Pattern Recognition Letters*, 24(4–5), 757–777.

Girard E., Zhou S., Walker W., Blalock T. and Hossack J. (2003) "High element count two dimensional transducer array." *IEEE International Ultrasonics Symposium*, 964–967.

Gori P., Cincotti G. and Pappalardo M. (2000) "Dense and sparse 2-D array radiation patterns in lossy media." *IEEE Transactions on Ultrasonics, Ferroelectrics and Frequency Control*, 47(4), 940–948.

Gubernatis J. E. (2005) "Marshall Rosenbluth and the Metropolis algorithm." *Physics of Plasmas*, 12(5), 057303.

Hajek B. (1988) "Cooling schedules for optimal annealing." *Mathematics of operations research*, 13, 311–329.

Happel C. M., Thommes J., Thrane L., Männer J., Ortmaier T., Heimann B. and Yelbuz T. M. (2011) "Rotationally acquired four-dimensional optical coherence tomography of embryonic chick hearts using retrospective gating on the common central A-scan." *Journal of Biomedical Optics*, 16(9).

Haupt R. (1994) “Thinned arrays using genetic algorithms.” *IEEE Transactions on Antennas and Propagation*, 42, 993 – 999.

Herth F. J. F. and Becker H. D. (2003) “Transthoracic Ultrasound.” *Respiration*, 70(1), 87–94.

Holm S. (2000) “Sparse and irregular sampling in array processing.” *IEEE International Conference on Acoustics, Speech, and Signal Processing*, 3850 –3853.

Holm S., Austeng A. and Iranpour K. (2001) “Sparse sampling in array processing.” *Sampling Theory and Practice*, ch 19.

Holm S., Elgetun B. and Dahl G. (1997) “Properties of the beampattern of weight- and layout-optimized sparse arrays.” *IEEE Transactions on Ultrasonics, Ferroelectrics and Frequency Control*, 44(5), 983 – 991.

Hopperstad J.-F. and Holm S. (1999) “Optimization of sparse arrays by an improved simulated annealing algorithm.” *International Workshop on Sampling Theory and Applications*, 91–95.

Housden R. J., Treece G. M., Gee A. H. and Prager R. W. (2008) “Calibration of an orientation sensor for freehand 3D ultrasound and its use in a hybrid acquisition system.” *BioMedical Engineering OnLine*, 7(1), 5.

Jensen J. A. (1996) “FIELD: A Program for Simulating Ultrasound Systems.” *10th Nordic-Baltic Conference on Biomedical Imaging*, 34, 351–353.

Jensen J. A., Holm O., Jensen L. J., Bendsen H., Pedersen H. M., Salomonsen K., Hansen J. and Nikolov S. (1999) “Experimental ultrasound system for real-time synthetic imaging.” *IEEE International Ultrasonics Symposium*, Caesars Tahoe, NV , USA, 1595–1599.

Jensen J. A. and Svendsen N. B. (1992) “Calculation of pressure fields from arbitrarily shaped, apodized, and excited ultrasound transducers.” *IEEE Transactions on Ultrasonics, Ferroelectrics and Frequency Control*, 39, 262–267.

Jian-Yu Lu and Greenleaf J. F. (1994) “A study of two-dimensional array transducers for limited diffraction beams.” *IEEE Transactions on Ultrasonics, Ferroelectrics and Frequency Control*, 41(5), 724–739.

Johnson J. A., Karaman M. and Khuri-Yakub B. T. (2002) “Phased subarray processing for underwater 3D acoustic imaging.” *OCEANS ’02 MTS/IEEE*, 2145–2151.

Karaman M., Wygant I. O., Oralkan O. and Khuri-Yakub B. T. (2009) “Minimally redundant 2-D array designs for 3-D medical ultrasound imaging.” *IEEE Transactions on Medical Imaging*, 28(7), 1051–1061.

Kesong C., Yun X., Z H. and Han C. (2007) “Synthesis of Sparse Planar Arrays Using Modified Real Genetic Algorithm.” *IEEE Transactions on Antennas and Propagation*, 55(4), 1067 – 1073.

Kirkpatrick S., Gelatt C. D. and Vecchi M. P. (1983) “Optimization by Simulated Annealing.” *Science*, 220(4598), 671 –680.

Kneif S., Hirche C., Mohr Z. and Hunerbein M. (2009) “Three-Dimensional Ultrasound in Soft Tissue Tumor Imaging.” *Current Medical Imaging Reviews*, 5, 210–215.

Kojima T. (1986) “Matrix Array Transducer and Flexible Matrix Array Transducer.” *IEEE International Ultrasonics Symposium*, 649 – 654.

Krenning B. J., Voormolen M. M. and Roelandt J. R. (2003) “Assessment of left ventricular function by three-dimensional echocardiography.” *Cardiovascular Ultrasound*, 1(1), 12.

Laarhoven P. J. van and Aarts E. H. (1987) *Simulated Annealing: Theory and Applications*. Springer.

Lacaze E., Michau S., Dufait R. and Flesch A. (1998) *A l'intérieur d'une barrette échographique*. Elsevier, Paris.

Larina I. V., Larin K. V., Dickinson M. E. and Liebling M. (2012) "Sequential Turning Acquisition and Reconstruction (STAR) method for four-dimensional imaging of cyclically moving structures." *Biomedical Optics Express*, 3(3), 650.

Lee N. N., O'Rourke R. W., Cheng J. and Hansen P. D. (2004) "Transthoracic hepatic radiofrequency ablation." *Surgical Endoscopy*, 18(11), 1672–1674.

Liao W.-Y., Chen M.-Z., Chang Y.-L., Wu H.-D., Yu C.-J., Kuo P.-H. and Yang P.-C. (2000) "US-guided Transthoracic Cutting Biopsy for Peripheral Thoracic Lesions Less than 3 cm in Diameter1." *Radiology*, 217(3), 685 –691.

Liebgott H. (2010) "Fourier domain beamforming for transverse-oscillations." *IEEE International Ultrasonics Symposium*, 1755–1758.

Liebgott H., Basarab A., Loizeau D., Wilhjelm J. E., Jensen J. A. and Delachartre P. (2006) "P3H-2 Improved Beamforming for Lateral Oscillations in Elastography Using Synthetic Aperture Imaging." *IEEE International Ultrasonics Symposium*, 2168–2171.

Light E. D., Angle J. F. and Smith S. W. (2008) "Real-Time 3-D Ultrasound Guidance of Interventional Devices." *IEEE Transactions on Ultrasonics, Ferroelectrics and Frequency Control*, 55(9), 2066–2078.

Light E. D., Davidsen R. E., Hruschka T. A. and Smith S. W. (1997) "Advances in two dimensional arrays for real time volumetric imaging." *IEEE International Ultrasonics Symposium*, Toronto, Ontario , Canada, 1619–1623.

Linguraru M. G. (2006) "Texture-based instrument segmentation in 3D ultrasound images." *Proceedings of SPIE*, San Diego, CA, USA, 61443J–61443J–9.

Lockwood G. R. and Foster F. S. (1996) "Optimizing the radiation pattern of sparse periodic two-dimensional arrays." *IEEE Transactions on Ultrasonics Ferroelectrics and Frequency Control*, 43(1), 15–19.

Lommi A., Massa A., Storti E. and Trucco A. (2002) "Sidelobe reduction in sparse linear arrays by genetic algorithms." *Microwave and Optical Technology Letters*, 32(3), 194–196.

Lurton X. (2002) *An Introduction to Underwater Acoustics: Principles and Applications*. Springer.

Maranda B. (1989) "Efficient digital beamforming in the frequency domain." *The Journal of the Acoustical Society of America*, 86(5), 1813–1819.

Matrone G., Quaglia F. and Magenes G. (2010) "Modeling and simulation of ultrasound fields generated by 2D phased array transducers for medical applications." *IEEE Engineering in Medicine and Biology Society*, 6003 –6006.

Matrone G., Quaglia F. and Magenes G. (2011) "Simulating ultrasound fields for 2D phased-array probes design optimization."*International Conference of the IEEE Engineering in Medicine and Biology Society*, 8507–8510.

Mendelsohn Y. and Wiener-Avnear E. (2002) "Simulations of circular 2D phase-array ultrasonic imaging transducers." *IEEE Transactions on Ultrasonics, Ferroelectrics and Frequency Control*, 39, 657–666.

Meunier J. and Bertrand M. (1995) "Ultrasonic texture motion analysis: theory and simulation." *IEEE transactions on medical imaging*, 14(2), 293–300.

Morton C. E. and Lockwood G. R. (2003) "Theoretical assessment of a crossed electrode 2-D array for 3-D imaging." *IEEE International Ultrasonics Symposium*, Honolulu, Hawaii, 968– 971.

Mucci R., Bolt B. and Newman (1984) “A comparison of efficient beamforming algorithms.” *IEEE Transactions on Acoustics, Speech and Signal Processing*, 32(3), 548 – 558.

Murino V. and Trucco A. (1994) “Dynamic focusing by FFT beamforming for underwater 3D imaging.” *Acoustics Letters*, 17(9), 169–172.

Murino V., Trucco A. and Regazzoni C. S. (1996) “Synthesis of unequally spaced arrays by simulated annealing.” *IEEE Transactions on Signal Processing*, 44(1), 119–122.

Nielsen R. O. (1991) *Sonar Signal Processing*. Artech House.

Nikolov S. I. and Jensen J. A. (2003) “Investigation of the feasibility of 3D synthetic aperture imaging.” *Ultrasonics*, 2, 1903 – 1906.

Nikolov S. I., Pablo Gómez Gonzaléz J. and Arendt Jensen J. (2003) “Real time 3D visualization of ultrasonic data using a standard PC.” *IEEE Ultrasonics*, 41(6), 421–426.

Okazawa S. H., Ebrahimi R., Chuang J., Rohling R. N. and Salcudean S. E. (2006) “Methods for segmenting curved needles in ultrasound images.” *Medical Image Analysis*, 10(3), 330–342.

Pospisil E. R., Rohling R., Azar R. Z. and Salcudean S. E. (2010) “4-D x 3-D ultrasound: real-time scan conversion, filtering, and display of displacement vectors with a motorized curvilinear transducer.” *IEEE Transactions on Ultrasonics, Ferroelectrics and Frequency Control*, 57(10), 2271–2283.

Puyun Guo, Shikui Yan and Quing Zhu (2001) “Elevation beamforming performance of a 1.75 D array.” *IEEE International Ultrasonics Symposium*, Atlanta, GA, USA, 1113–1116.

Rachedine M. and Zerhouni M. B. (1993) “Ultrasonic calibration material and method.”

Ramm O. T. and Smith S. W. (1990) “Real time volumetric ultrasound imaging system.” *Journal of Digital Imaging*, 3(4), 261–266.

Robini M. C. (2013) “Theoretically Grounded Acceleration Techniques for Simulated Annealing.” *Handbook of Optimization*, Intelligent Systems Reference Library, Springer, 311–335.

Robini M. C., Rastello T. and Magnin I. E. (1999) “Simulated annealing, acceleration techniques, and image restoration.” *IEEE Transactions on Image processing*, 8(10), 1374–1387.

Robini M. C. and Reissman P.-J. (2013) “From simulated annealing to stochastic continuation: a new trend in combinatorial optimization.” *Journal of Global Optimization*, 56(1), 185–215.

Sartori S., Tombesi P., Trevisani L., Nielsen I., Tassinari D. and Abbasciano V. (2007) “Accuracy of Transthoracic Sonography in Detection of Pneumothorax After Sonographically Guided Lung Biopsy: Prospective Comparison with Chest Radiography.” *Am. J. Roentgenol.*, 188(1), 37–41.

Savord B. and Solomon R. (2003) “Fully sampled matrix transducer for real time 3D ultrasonic imaging.” *IEEE International Ultrasonics Symposium*, Honolulu, Hawaii, 945–953.

Seggie D. A., Leeman S. and Burge R. E. (1983) “Realistic Simulation of B-Scan Images.” *IEEE International Ultrasonics Symposium*, 714–717.

Shattuck D. P., Weinshenker M. D., Smith S. W. and von Ramm O. T. (1984) “Explososcan: A parallel processing technique for high speed ultrasound imaging with linear phased arrays.” *The Journal of the Acoustical Society of America*, 75(4), 1273–1282.

Shung K. K. (2002) “The principle of multidimensional arrays.” *European Journal of Echocardiography*, 3(2), 149–153.

Smith S. W., Pavy H. G. and von Ramm O. T. (1991a) “High-speed ultrasound volumetric imaging system. II. Parallel processing and image display.” *IEEE Ultrasonics*, 38(2), 109 – 115.

Smith S. W., Pavy H. G. and von Ramm O. T. (1991b) “High-speed ultrasound volumetric imaging system. I. Transducer design and beam steering.” *IEEE Ultrasonics*, 38(2), 100 – 108.

Smith S. W. (2001) “Methods and systems for selective processing of transmit ultrasound beams to display views of selected slices of a volume.”

Stepanishen P. R. (1971) “The Time-Dependent Force and Radiation Impedance on a Piston in a Rigid Infinite Planar Baffle.” *The Journal of the Acoustical Society of America*, 49(3B), 841–849.

Stepanishen Peter R. (1971) “Transient Radiation from Pistons in an Infinite Planar Baffle.” *The Journal of the Acoustical Society of America*, 49(5B), 1629–1638.

Taki H. and Sato T. (2007) “High-resolution real-time three-dimensional acoustic imaging system with a reflector.” *Journal of Medical Ultrasonics*, 34(3), 133–144.

Tekes C., Karaman M. and Degertekin F. (2011) “Optimizing circular ring arrays for forward- looking IVUS imaging.” *IEEE Transactions on Ultrasonics, Ferroelectrics and Frequency Control*, 58(12), 2596–2607.

Thomenius K. E. (1996) “Evolution of ultrasound beamformers.” *IEEE International Ultrasonics Symposium*, San Antonio, TX , USA, 1615–1622 vol.2.

Tortoli P., Bassi L., Boni E., Dallai A., Guidi F. and Ricci S. (2009) “ULA-OP: an advanced open platform for ultrasound research.” *IEEE Transactions on Ultrasonics, Ferroelectrics and Frequency Control*, 56, 2207–2216.

Tournois P., Calisti S., Doisy Y., Bureau J. M. and Bernard F. (1995) “A 128×4 channels 1.5D curved linear array for medical imaging.” *IEEE International Ultrasonics Symposium*, Seattle, WA , USA, 1331–1335.

Trucco A. (1999) “Thinning and weighting of large planar arrays by simulated annealing.” *IEEE Transactions on Ultrasonics, Ferroelectrics and Frequency Control*, 46, 347–355.

Trucco A. (2002) “Weighting and thinning wide-band arrays by simulated annealing.” *IEEE Ultrasonics*, 40(1-8), 485–489.

Trucco A., Palmese M. and Repetto S. (2008) “Devising an Affordable Sonar System for Underwater 3-D Vision.” *IEEE Transactions on Instrumentation and Measurement*, 57, 2348 –2354.

Trucco A. and Repetto F. (1996) “A stochastic approach to optimizing the aperture and the number of elements of an aperiodic array.” *OCEANS ’96. MTS/IEEE*, 1510–1515.

Tupholme G. E. (1969) “Generation of acoustic pulses by baffled plane pistons.” *Mathematika*, 16(02), 209–224.

Turnbull D. H. and Foster F. S. (1991) “Beam steering with pulsed two-dimensional transducer arrays.” *IEEE Transactions on Ultrasonics, Ferroelectrics and Frequency Control,* 38, 320–333.

Tweedie A., Murray V. and Hayward G. (2009) “Aperiodic and deterministic 2D phased array structures for ultrasonic imaging.” *IEEE International Ultrasonics Symposium*, Rome, Italy, 406–409.

Uherčík M., Kybic J., Liebgott H. and Cachard C. (2010) "Model Fitting Using RANSAC for Surgical Tool Localization in 3-D Ultrasound Images." *IEEE Transactions on Biomedical Engineering*, 57, 1907–1916.

Varray F., Cachard C., Tortoli P. and Basset O. (2010) "Nonlinear radio frequency image simulation for harmonic imaging: Creanuis." *IEEE International Ultrasonics Symposium*, 2179–2182.

Weber P. K., Austeng A., Holm S. and Aakvaak N. (1999) "1D- and 2D-Sparse-Array-Optimization." *Instrumentation Science & Technology*, 27(4), 235–246.

Weber P. K., Schmitt R. M., Tylkowski B. D. and Steck J. (1994) "Optimization of random sparse 2-D transducer arrays for 3-D electronic beam steering and focusing." *IEEE International Ultrasonics Symposium*, Cannes, France, 1503–1506.

Wildes D. G., Chiao R. Y., Daft C. M. W., Rigby K. W., Smith L. S. and Thomenius K. E. (1997) "Elevation performance of 1.25D and 1.5D transducer arrays." *IEEE Transactions on Ultrasonics, Ferroelectrics and Frequency Control,* , 44(5), 1027–1037.

Wu Qiu, Mingyue Ding and Ming Yuchi (2008) "Needle Segmentation Using 3D Quick Randomized Hough Transform." *International Conference on Intelligent Networks and Intelligent Systems, 2008*, 449–452.

Wygant I. O. (2006) "Beamforming and hardware design for a multichannel front-end integrated circuit for real-time 3D catheter-based ultrasonic imaging." *Proceedings of SPIE*, San Diego, CA, USA, 61470A–61470A–8.

Wygant I. O., Xuefeng Zhuang, Yeh D. T., Oralkan O., Ergun A. S., Karaman M. and Khuri-Yakub B. T. (2008) "Integration of 2D CMUT arrays with front-end electronics for volumetric ultrasound imaging." *IEEE Transactions on Ultrasonics, Ferroelectrics and Frequency Control*, 55(2), 327–342.

Xie M.-X., Wang X.-F., Cheng T. O., Lu Q., Yuan L. and Liu X. (2005) "Real-Time 3-Dimensional Echocardiography: A Review of the Development of the Technology and Its Clinical Application." *Progress in Cardiovascular Diseases*, 48(3), 209–225.

Yang P., Chen B. and Shi K.-R. (2006) "A novel method to design sparse linear arrays for ultrasonic phased array." *IEEE Ultrasonics*, 44(1), e717–e721.

Yen J. T. and Smith S. W. (2002) "Real-time rectilinear volumetric imaging using a periodic array." *Ultrasound in Medicine and Biology*, 28(7), 923–931.

Zhang F., Bilas A., Dhanantwari A., Plataniotis K. N., Abiprojo R. and Stergiopoulos S. (2002) "Parallelization and performance of 3D ultrasound imaging beamforming algorithms on modem clusters." *International Conference on Supercomputing*.

Zhang L., Jiao Y.-C., Chen B. and Li H. (2012) "Orthogonal Genetic Algorithm for Planar Thinned Array Designs." *International Journal of Antennas and Propagation*, 1–7.